Charakterisierung dipolarer Wechselwirkungen magnetischer Nanopartikel in mesoskopischen Ensembles

---

Characterization of dipolar interactions of magnetic nanoparticles in mesoscopic ensembles

JUSTUS-LIEBIG-UNIVERSITÄT GIESSEN

Dissertation

zur Erlangung des akademischen Grades

Doktor der Naturwissenschaften
- Dr. rer. nat. -

vorgelegt von Nils Neugebauer

This dissertation is written in English

Vom Fachbereich 07 für Mathematik und Informatik, Physik, Geographie
der Justus-Liebig-Universität Gießen als Dissertation angenommen am: 11.08.2023

Datum der Disputation: 15.12.2023

Erstgutachter: Prof. Dr. Peter J. Klar

Zweitgutachter: Prof. Dr. Christian Heiliger

Mitglieder der Prüfungskommission:
Prof. Dr. Peter J. Klar[1,2]
Prof. Dr. Christian Heiliger[2,3]
Prof. Dr. Detlev M. Hofmann[1,2]
Prof. Dr. Martin D. Buhmann[4]

---

[1] Institute of Experimental Physics I, Justus Liebig University, Heinrich-Buff-Ring 16, 35392 Giessen, Germany

[2] Center for Materials Research (ZfM/LaMa), Justus Liebig University, Heinrich-Buff-Ring 16, 35392 Giessen, Germany

[3] Institute for Theoretical Physics, Justus Liebig University, Heinrich-Buff-Ring 16, 35392 Giessen, Germany

[4] Mathematics Institute, Justus-Liebig University, Heinrich-Buff-Ring 44, 35392 Giessen, Germany

Nur wenige wissen, wie viel man wissen muss, um zu wissen, wie wenig man weiß.

Few know how much you need to know to know how little you know.

- Werner Heisenberg -

Contents

Kurzfassung

Die Eigenschaften von Materialien werden nicht nur durch die Charakteristika auf atomarer Ebene bestimmt, sondern ebenfalls durch die Rahmenbedingungen auf makroskopischen Skalen. So kann unter anderem die Form eines Festkörpers eine entscheidende Bedeutung für die Eigenschaften eben dieses haben. Beispielsweise führt dies im Falle eines Magneten dazu, dass auf Grund von dessen *Demagnetisierung* gewisse präferierte Raumachsen für die Orientierung der makroskopischen Magnetisierung beobachtet werden können.

Im Zuge einer stetigen Optimierung verschiedenster Syntheseverfahren ist es mit modernen Methoden möglich geworden, Rahmenbedingungen zur Manipulation der Eigenschaften eines Festkörpers nicht mehr ausschließlich auf makroskopischer Ebene ($> 10^{-6}$ m) bzw. atomarer Ebene ($< 10^{-9}$ m) vorzugeben, sondern diese ebenfalls im Bereich zwischen makroskopischer und atomarer Ebene, der mesoskopischen Skala (etwa 10^{-8} m bis 10^{-6} m), vorzunehmen. Hier ist im Besonderen der Fortschritt chemischer Verfahren hervorzuheben, welche es heute ermöglichen, Strukturen bestehend aus wenigen bis einigen tausend Atomen zu synthetisieren, sogenannte *Nanopartikel* (NP). Unter Verwendung von NP mit wohldefinierter Form und einer sehr schmalen Größenverteilung lassen sich durch Ausnutzung von Selbstorganisationsprozessen hochgeordnete, periodische NP-Gitter bzw. NP-Kristalle herstellen. Da es sich hierbei um einen mesoskopisch strukturierten Kristall handelt, werden diese verallgemeinert als *Mesokristalle* bezeichnet.

Mesokristalle stellen somit eine Klasse von *Metamaterialen* dar. Diese Metamaterialien zeichnen sich dadurch aus, dass kleinere Bausteine eines Festkörpers periodisch angeordnet in eine größere Struktur eingebunden sind. Durch diese periodische Anordnung können Phänomene auftreten, welche im unstrukturierten Volumenmaterial nicht beobachtet werden können. Diese neuartigen Phänomene in hierarchisch aufgebauten Materialen zu charakterisieren ist sowohl aus fundamentaler, wissenschaftlicher Perspektive als auch aus technischer Sicht von großem Interesse. Entspricht etwa die Größe der verwendeten NP im Mesokristall der typischen Wechselwirkungslänge des entsprechenden Volumenmaterials, so sind Abweichungen der zugehörigen Materialparameter zu erwarten, die es zu charakterisieren und zu verstehen gilt. Weiterhin ermöglichen es die Eigenschaften von Metamaterialien, die Ausbreitung von elektromagnetische Wellen zu manipulieren, was weit über den Rahmen konventioneller Materialien hinausgeht. Beispielsweise ändern sich die Transmissions- bzw. Reflektionseigenschaften eines Materials grundlegend, wenn die Wellenlänge einer elektromagnetischen Welle der Periodizität des Mesokristalls entspricht.

Im Rahmen dieser Arbeit wurden die magnetischen Eigenschaften von Strukturen bestehend aus magnetischen Nanopartikeln (MNP) systematisch untersucht. Ein zentraler Aspekt hierbei war es einen grundlegenden Beitrag zum Verständnis der Dipol-Dipol-Wechselwirkung zwischen den MNP in hochgehordneten, wohldefinierten Anordnungen zu leisten. In Publikation 1 wird zunächst die Wechselwirkung benachbarter kreisförmiger MNP-Anordnungen behandelt. Die einzelnen MNP haben einen Durchmesser von 20 nm und weisen eine Polyethylenglycol-Beschichtung auf, wodurch sich ein Interpartikelabstand von etwa 2 nm ergibt. Mit Hilfe von Ferromagnetischen-Resonanz Experimenten (FMR) konnte gezeigt werden, dass bei solchen MNP-Anordnungen mit einer Ausdehnung im Bereich einiger 100 nm zwei resonante magnetische Schwingungsmoden, eine Haupt- und eine Nebenresonanz, auftreten. Eine systematische Verringerung des Abstandes zwischen den kreisförmigen MNP-Anordnungen hat zur Folge, dass die beobachtete Nebenresonanz an Intensität zunimmt. Weiterhin konnte bei einer Verringerung der Abstände eine zunehmende Winkelabhängigkeit der Resonanzfeldstärke in winkelabhängigen FMR-Experimenten nachgewiesen werden. Dies konnte darauf zurückgeführt werden, dass die Nebenresonanz auf den Randbereich der MNP-Anordnung beschränkt ist, wohingegen für die Hauptresonanz auf eine Mode des zentralen Bereichs geschlossen wird.

Aufbauend auf diesen Erkenntnissen wurde in Publikation 2 der Ursprung der beiden Resonanzen näher untersucht. Hierfür wurden 20 nm große MNPs mit einer Ölsäure-Beschichtung in einer hochgeordneten, hexagonalen Anordnung auf einem Substrat abgeschieden und anschließend mittels Elektronenstrahllithographie in ein kreisförmiges MNP-Ensemble von etwa 450 nm Durchmesser strukturiert. Durch ortsaufgelöste Brillouin-Licht-Streuung (BLS) konnten die Interpretationen aus Publikation 1 in Bezug auf die resonanten Bereiche der beiden Signale weiter untermauert werden. Weiterhin konnte im Rahmen frequenzabhängiger Messungen dargelegt werden, inwiefern das Intensitätsverhältnis der beiden Signale durch die Dipol-Dipol-Wechselwirkung innerhalb der Struktur bestimmt wird.

Während in den beiden ersten Arbeiten der Fokus auf die Eigenschaften von MNP-Ensembles im Zusammenhang mit ihrer äußeren Form auf der Mikrometer-Skala beziehungsweise auf die Wechselwirkung zwischen ihnen gelegt wurde, befasst sich Publikation 3 genauer mit den magnetischen Charakteristika von Mesokristallen, welche auf der Nanometer-Skala durch den Abstand der MNP und damit durch die Gitterkonstante des Mesokristalls beeinflusst werden. In diesem Zusammenhang wurde der Durchmesser und der Interpartikelabstand der MNP systematisch variiert. Im Rahmen von FMR-Experimenten an zweidimensionalen (2D) Mesokristallen wurde untersucht, inwiefern die dynamischen Eigenschaften von dem entsprechenden MNP-Gitter beeinflusst werden. Weiterhin konnte im Rahmen dieser Arbeit gezeigt werden, dass die entsprechenden Materialparameter, wie die Magnetisierung und die effektive Anisotropie der MNP, im Vergleich zu dem Volumenmaterial verringert sind. Dies wird auf strukturelle Defekte innerhalb der MNP zurückgeführt, welche zur Bildung von Subdomänen innerhalb der MNP führen und somit die Reduktion dieser Materialparameter erklären.

Abstract

The properties of a material are influenced not only by the circumstances on the atomic scale, but also by the framework conditions on macroscopic scales. Thus, e.g., the shape of a solid can have a decisive influence on the characteristics of the entire solid. In case of a magnet, for example, certain preferred spatial axes for the orientation of its macroscopic magnetization can be observed due to its *demagnetization* associated with its geometry.

In the course of a continuous optimization of various synthesis techniques, modern methods have made it possible to engineer framework conditions for the manipulation of the properties of an entire solid no longer exclusively on the macroscopic level ($> 10^{-6}$ m) or atomic level ($< 10^{-9}$ m), but also in the range between macroscopic and atomic level, the mesoscopic scale (approximately 10^{-8} m to 10^{-6} m). Here, the advances in chemical processes must particularly be emphasized which have made it possible to synthesize structures consisting of a few to some thousand atoms, known as *nanoparticles* (NP). Using NPs with a well-defined shape and a very narrow size distribution, the fabrication of highly ordered, periodic NP lattices or NP crystals may be facilitated by exploiting self-assembling processes. Since this may be regarded as a mesoscopically structured crystal, these are generally denoted as *mesocrystals*.

Mesocrystals thus represent a class of *metamaterials*, which are characterized by the fact that smaller building blocks of a material are periodically arranged into a larger structure. In such metamaterials, phenomena can occur which cannot be observed in unstructured bulk material. Characterizing these novel phenomena of hierarchical materials is of great interest from a fundamental, scientific perspective as well as from an engineering point of view. The use of metamaterials not only yields technical innovations, but also allows one to investigate fundamental properties of matter. If, for example, the size of the NPs used in a mesocrystal corresponds to the typical interaction length of the corresponding bulk material, deviations in the associated material parameters can be expected, which must be characterized and understood. Furthermore, the properties of metamaterials allow one to manipulate electromagnetic waves in a fashion which is far beyond the possibilities of conventional materials. For example, transmission or reflection properties of a material change fundamentally when the wavelength of an electromagnetic wave matches the periodicity of the mesocrystal.

In this work, the magnetic properties of structures consisting of magnetic nanoparticles (MNPs) were systematically investigated. A central aspect here was to make a fundamental contribution to the understanding of the dipole-dipole interaction between

MNPs in highly ordered, well-defined arrangements. Publication 1 first discusses the interaction of adjacent circular MNP assemblies. The individual MNPs are 20 nm in diameter and have a polyethylene glycol coating, resulting in an interparticle spacing of about 2 nm. Using ferromagnetic resonance (FMR) experiments, it was shown that two resonant magnetic excitation modes occur, a main and a satellite resonance, in a size range of the assembly of some hundreds of nanometers. Systematically decreasing the spacing between the circular MNP assemblies results in an increase of the intensity of the observed satellite resonance. Furthermore, a stronger angular dependence of the resonance field strength in angle-dependent FMR experiments has been found when the distances are reduced. This could be attributed to the fact that the satellite resonance is confined to the edge region of the MNP assemblies, whereas modes of the central region are assigned to the main resonance.

Building on these findings, the origin of the two resonances was investigated in more detail in Publication 2. For this purpose, 20 nm sized MNPs with an oleic acid coating were deposited in a highly ordered hexagonal arrangement on a substrate and subsequently then patterned into circular MNP ensembles of about 450 nm diameter by electron beam lithography. Spatially resolved Brillouin light scattering spectroscopy (BLS) was used to further substantiate the interpretations from Publication 1 with respect to the resonant spatial regions of the two signals. Furthermore, performing frequency-dependent measurements, it has been shown to what extent the intensity ratio of the two signals is determined by the dipole-dipole interaction within the structure.

The first two papers focused on the properties of MNP ensembles affected by their outer shape on the micrometer scale and their mutual interaction, respectively. Publication 3 provides a more precise investigation concerning the magnetic characteristics of mesocrystals, which are influenced on the nanometer scale by the spacing and the diameter of the MNPs and thus the lattice constant of the mesocrystal. Within the framework of FMR experiments on two-dimensional (2D) mesocrystals, it was investigated to what extent the dynamic properties are influenced by the corresponding MNP lattice. Furthermore, it was shown that the corresponding material parameters, such as the magnetization and the effective anisotropy of the MNPs, are reduced compared to corresponding bulk material. This is attributed to structural defects within the MNPs, which lead to the formation of subdomains within the MNPs and thus explains the reduction of these material parameters.

Symbols and Abbreviations

Symbol	**SI-Unit**	**Physical Quantity**
$\mathbb{1}_2$	dimensionless	Identity matrix of rank 2
α	dimensionless	Damping constant of the magnetization precession
α_{TFPI}	rad	Angle between the two beam lines in a tandem-(3+3)-Fabry-Pérot interferometer
$\hat{\alpha}, \hat{\beta}$	dimensionless	Dirac's operator for linearizing the Klein-Gordon-equation
A_{FMR}	arbitrary unit	Intensity of a ferromagnetic resonance (FMR) spectrum
A	J/m	Exchange stiffness constant
$\vec{A}$	T·m	Magnetic vector potential
$\vec{a}_{1,2}$	dimensionless	Eigenvectors of the Dirac Hamiltonian of the free electron
a_{meso}	m	Lattice constant of the mesocrystal
B_{aniso}, B_{dd}, B_{exc}, B_{mod}, B_{ω}, B_{res}, B_{shape}, B_{stat}, B_{surf}, B_{tot}	T	Magnetic field strengths for: the magnetocrystalline anisotropy, the dipole-dipole interaction, the exchange interaction, the modulation for the static external field, the microwave field, the field strength at which the resonance occurs, the shape anisotropy, the static external field, the surface anisotropy, and the total magnetic field
C	J	Coulomb integral
c	m/s	Velocity of light in vacuum
d_{crit}	m	Critical diameter below which magnetic solids are in the single domain state
d_{MNP}	m	Diameter of the MNP
d_{shell}	m	Thickness of the non-magnetic MNP shell
d_{spacer}	m	Spacing between the MNPs
$d_{\mathrm{x^2-y^2}}$	dimensionless	Linear combination of the orbital wave function with an azimuthal quantum number $l = 2$ and a magnetic quantum number $m_{\mathrm{l}} = \pm 2$
Δ	$1/\mathrm{m}^2$	Laplace operator
e	C	Elementary charge

ϵ_0	A·s/V·m	Vacuum permittivity
$E^{(0)}$, E_aniso, E_shape	J	Energy of isolated hydrogen atoms, the magnetocrystalline anisotropy, and the shape anisotropy
f	1/s	Frequency
$\lvert\psi\rangle$, $\lvert\phi\rangle$, $\lvert\chi\rangle$	dimensionless	Total, orbital, and spin wavefunction
ϕ_B, ϕ_i	rad	Angle of the magnetic field and impinging photons with respect to the film plane
φ_e	J	Electrostatic potential
φ_M	A	Magnetic surface potential
γ	A·s/kg	Gyromagnetic ratio
$\tilde{\gamma}$	dimensionless	Lorentz factor
g	dimensionless	Landé (/g-) factor
$\hbar$	J·s	Reduced Planck constant
$\mathcal{H}$, $\mathcal{H}^{(0)}$, $\mathcal{H}^{(1)}$, $\mathcal{H}^{(\mathrm{eff})}$	J	Hamiltonians of two hydrogen atoms: the total interaction, for the unperturbed system, and the mutual interaction
$\mathcal{H}_\mathrm{D}^0$, $\mathcal{H}_\mathrm{D}$	J	Dirac Hamiltonians of a free electron and an electron in an electromagnetic field
$\mathcal{H}_\mathrm{P}^0$	J	Pauli Hamiltonian of an electron in an electromagnetic field
$\mathcal{J}_\mathrm{ij}$	J	Exchange energy constant
J, J_z	J·s	Total angular momentum of an isolated ion and its associated z-component
J^exc	J	Exchange integral
K_1	J/m^3	First magnetocrystalline anisotropy constant
$\overrightarrow{k}_\mathrm{i}$, $\overrightarrow{k}_\mathrm{f}$, $\overrightarrow{k}_\mathrm{M}$	1/m	Wave vector of the impinging, reflected, and magnonic wave
λ_phot	m	Wavelength of a photon
λ_so	1/kg·m^2	Spin-orbit coupling constant
$\overrightarrow{l}$	J·s	Angular momentum
μ_0	N/A^2	Vacuum magnetic permeability
μ_B	T	Bohr magneton
m, m_z	A·m^2	Magnetic moment and its z-component
m_s	A·m^2	Magnetic moment of an electron associated with its spin
m_j	dimensionless	Secondary magnetic quantum number
m_e	kg	Mass of the electron
M_sat	A/m	Saturation magnetization
∇	1/m	Nabla operator
$\underline{\underline{\mathrm{N}}}$	dimensionless	Demagnetization tensor
p, p_x, p_y	dimensionless	Orbital wave function with an azimuthal quantum number $l = 1$ and a magnetic quantum number $m_l = 1$
$\overrightarrow{p}$	kg·m/s	Momentum operator

r_{a1}, r_{b2}, R_{ab}, r_{12}, r_{b1}, r_{a2}	m	Distance between the "first" electron and the "first" nucleus, the "second" electron and the "second" nucleus, the two nuclei, the two electrons, the "second" electron and the "first" nucleus, and the "first" electron and the "second" nucleus
$\sigma_{(x,y,z)}$	dimensionless	Pauli spin matrices
σ_{M}	A/m^2	Magnetic surface charge density
S	dimensionless	Overlapp integral
$\vec{s}_{\mathrm{i}}$	J·s	Vector of spin *i*
$\hat{s}$	J·s	Dirac spin operator
t	s	Time
ω	rad/s	Angular frequency
ω_{M}, ω_{f}, ω_{i}	rad/s	Angular frequency of the magnon, the scattered and impinging photons
$V(\vec{r})$	J	Crystal field potential
V	m^3	Volume
v	m/s	Velocity
$\mathcal{Y}_l^m$	dimensionless	Spherical harmonic with $l \geq \lvert m \rvert$, and l & m the azimuthal and magnetic quantum number
Z^*	dimensionless	Screened number of nuclear charges

Abbreviations	**Denotation**
$\langle a \rangle$	Expectation value of the observable a
$\{a,b\}$	Commutator of the two operators a and b
1D, 2D, 3D	One-, two, three-dimensional
BDF	Backward differentiation formula
BLS	Brillouin-Light-Scattering microscopy
BS	Beam splitter
DC	Direct current
DEG	Diethylene glycol
e-beam	Electron beam
EBL	Electron beam lithography
FDM	Finite differences methods
FEM	Finite elements methods
Fe_3O_4	Chemical formula of magnetite
$Fe^{2+/3+}_{oct/tet}$	Octahedrally and tetrahedrally coordinated iron (2+/3+) ions
Fe(acac)	Iron acetylacetonate
Fe(oleate)	Iron oleate complexes
FMR	Ferromagnetic resonance
FPI	Fabry-Pérot interferometer
IVP	Initial value problem
$\lambda/2$-plate	Half-wave plate
L	Lens
MFM	Magnetic force microscopy
MNP	Magnetic nanoparticle
MOKE	Magneto-optic Kerr effect
NP	Nanoparticle
OA	Oleic acid
ODE	Ordinary differential equation
OOMMF	The Object Oriented MicroMagnetic Framework project at ITL/NIST
PBS	Polarizing beam splitter
PEG	Polyethylene glycol
PMMA	Polymethyl methacrylate
PS	Polystyrene
PTFE	Polytetrafluoroethylene
Q-factor	Quality factor
STM	Semitransparent mirror
TEM	Transmission electron microscopy
TFPI	Tandem-(3+3)-Fabry-Pérot interferometer
VNA	Vector network analyzer

Figures and Tables

1

Introduction

In a solid crystal, the constituent atoms or ions are located at the atomic sites in a periodic crystal lattice structure. This arrangement is illustrated schematically at the bottom image of the left column in figure 1.1. The collective properties of the material at the atomic scale are governed by two essential factors: the specific arrangement of the ions on the crystal lattice sites, which determines a distinct structural framework, and the interactions between the ions. Together they yield the collective properties of the material.

Employing conventional fabrication techniques for solid materials, the manipulation of the solid's macroscopic characteristics may be performed by engineering the interactions between the ions at the atomic scale by, e.g., doping or alloying the material with a different chemical element. Hence, its macroscopic properties such as its electrical conductivity may be tuned precisely.

Furthermore, conventional fabrication techniques offer the ability to influence the macroscopic properties of the solid through structuring the material using lithographic techniques, as exemplified in the right column of Figure 1.1. The figure illustrates the manipulation of macroscopic properties through the arrangement of smaller entities derived from dense thin films. At the macroscopic scale, it is possible to tune the properties of a material by controlling the shape of the smaller entities and their arrangement on a specific lattice. In doing so, it becomes possible to manipulate the interactions between the individual entities, thereby influencing the collective properties of the material at the macroscopic scale.

It may be concluded that the degrees of freedom to tune the characteristics of the material using conventional fabrication techniques are limited to the atomic and macroscopic scale only. In contrast, the incorporation of nanoparticles (NPs) may offer additional degrees of freedom to tune and control the macroscopic properties of a material which are introduced at the mesoscopic scale. Consequently, the utilization of NPs provides additional opportunities to adjust and modulate material properties that are beyond the limitations of conventional fabrication techniques. This is highlighted by the gray shaded (middle) column in figure 1.1 which emphasizes the additional degrees of freedom to manipulate the characteristics of a material by employing NPs. As in the case of manipulating material characteristics at the atomic and the macroscopic scale, where the collective properties are governed by the features of the individual constituents and their mutual coupling at the respective scales, similar opportunities are introduced at the mesoscopic scale. Thus, on the one hand, both the properties of the individual NPs

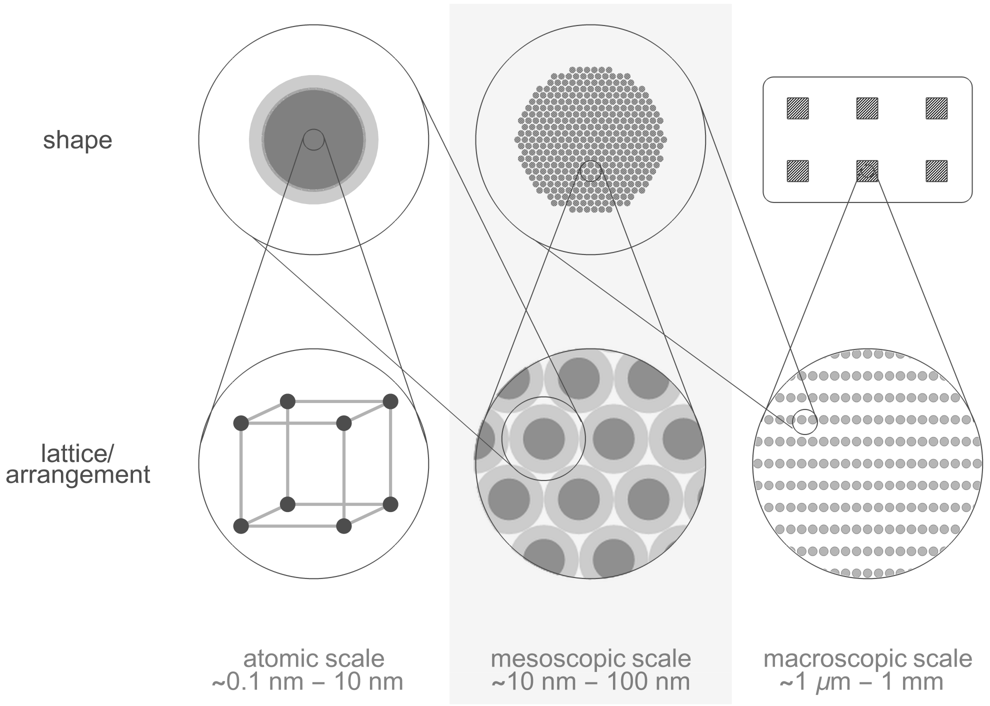

Figure 1.1: Employing nanoparticles of a material and arranging these into highly ordered structures opens up additional degrees of freedom for tuning at the mesoscopic scale (level 2). By manipulating, e.g., the size, shape, and arrangement of the constituents, the collective properties may be tuned leading to phenomena that would not arise by a manipulation at the macroscopic or atomic scale only. This image is reproduced in the style of Ref. [3]

as well as the interactions between them open up a vast playground to precisely tune the collective characteristics of the whole solid, and, on the other hand, the emergence of potential novel phenomena introduced at this scale may be employed for innovative technological applications [1, 2].

The individual properties of NPs are determined by two key factors. At the atomic scale, the NP characteristics are fundamentally governed by the interactions between the constituent ions giving rise to, e.g., magnetic properties which is emphasized in the bottom image of the left column in Fig. 1.1. Complementarily, the shape of the NP plays a significant role as well. Modern synthesis techniques have facilitated the fabrication of various shapes of NPs such as spheres, cubes, plates, or even polyhedral geometries, which is emphasized in figure 1.1 in the top image of the left column [4, 5, 6]. Moreover, their size can be precisely controlled by, e.g., adjusting the reaction temperature during their synthesis [4, 7]. Consequently, at the level of the individual NPs, at least two additional degrees of freedom to manipulate macroscopic material characteristics are introduced by controlling the shape and size of the NPs. However, when the size of nanoparticles decreases, deviations in the material parameters may occur, particularly when the nanoparticle size approaches the characteristic length scale of specific interactions between the ions within the material. It is important to note that the material parameters of the bulk counterpart represent the properties of a sufficiently large volume, such that the solid can be considered as infinitely large and the symmetry break at the surface has a subsidiary impact on the properties of the solid. Therefore, when comparing the material parameters of NPs with its bulk counterparts, it is important to consider and characterize potential deviations of the corresponding parameters in detail. Thus, the employment of nanoparticles not only introduces additional degrees of freedom to tune the overall characteristics of a material but also opens up the possibility to systematically investigate the relative strengths of the interactions at the different length scales by varying the NP size [132]. As the sizes of NPs ranges from some nanometers to some tens of nanometers in diameter, they are ideal model systems to investigate the transition from the quantum mechanically dominated regime to classical interaction regimes [8]. Hence, magnetic nanoparticle (MNP) arrangements serve as ideal model systems for systematically studying how the dominant magnetic interactions vary with the characteristic period of the MNP arrangement.

To illustrate this with a simple example, consider the magnetostatic coupling phenomena that predominantly govern the magnetic properties of a macroscopic magnetic structure (see fig. 1.1 - level 3) [8, 9]. In a macroscopic magnetic solid, the formation of magnetic domains with different orientations is driven by the need to minimize the magnetostatic energy. As the size of a magnetic entity decreases, the strength of magnetostatic coupling scales accordingly [10]. However, this magnetostatic coupling competes with the exchange interactions within the solid, as the formation of magnetic domains causes an energetic cost due to the increased exchange energy associated with the tilting of the magnetic moments of the ions at the domain boundaries. Due to this competition, there exists a transition region where the exchange interactions may prevail, resulting in a single-domain state of the magnetic solid. Thus, by decreasing the volume of the magnetic solid, the characteristics of the magnetic material are increasingly governed by the quantum mechanical exchange interactions. The transition between the two regimes depends on the ratio of the strength of the exchange energy between the constituent ions and the magnetostatic energy of the magnetic entity. It is expected to occur for MNPs with a diameters ranging between $d_{\text{MNP}} \approx 100$ nm to ≈ 10 nm [8, 9]. Therefore, at the mesoscopic scale (see fig. 1.1 - level 2), the characteristics of an individual MNP is crucially affected by both the classical magnetostatic and quantum mechanical exchange interactions [11].

In addition, not only the individual properties of the NPs are of particular interest, but also the collective characteristics of the whole arrangement arising from mutual interactions between the NPs [12, 13]. By exploiting self-assembling processes during the deposition of NPs onto a desired substrate, it becomes possible to fabricate ordered assemblies of NPs that exhibit various symmetries in their arrangement such as hexagonal or honeycomb lattices. Employing two or more species of NPs with suitable sizes and concentration ratios and using appropriate deposition techniques to fabricate ordered NP lattices [14], more intricate lattice structures can be fabricated. This approach enables the formation of sophisticated lattices with, e.g., cubic and orthorhombic symmetries [5, 6], which further expands the possibilities for material design and engineering introduced at the mesoscopic scale. Such highly ordered, periodic NP lattices showing translational symmetry or even superlattices are known as *mesocrystals*, as they can be considered as mesoscopically structured crystals. This is schematically shown at the bottom image of the gray shaded (middle) column in figure 1.1 for a manipulation of material characteristics at the level of the arrangement of NPs into mesocrystals. In addition, using lithographic techniques it is possible to synthesize structured, mesoscopically arranged materials [15, 16]. By precisely controlling the shape and size of the structured NP ensemble, further degrees of freedom to tune the properties of the material are introduced as indicated in the top image of the gray shaded (middle) column in figure 1.1 by the circularly structured, hexagonally arranged NP ensemble.

Hence, the material properties are determined on various hierarchical length scales and, thus, such hierarchical structures offer a great variety of novel opportunities to manipulate the macroscopic characteristics of the material. Consequently, the integration of the mesoscopic scale in material design and engineering, through the utilization of nanoparticles (NPs), presents an approach that surpasses the limitations of conventional dense thin film techniques. This advancement offers novel strategies to precisely control and manipulate material properties, paving the way for innovative technological applications and devices. Due to the periodic arrangement of the NPs novel phenomena may occur in which can be exploited for applications with desired functionalities, which are not available in their naturally found monolithic counterpart [1]. Materials that show corresponding emergent periodicity-dependent characteristics are commonly referred to as *metamaterials*. This new class of materials has attracted considerable attention in the field of materials science [12, 18].

The precise control of the interactions at the mesoscopic scale is a subject of significant interest, as the collective characteristics and the emerging properties of metamaterials are crucially governed by the coupling phenomena between the NPs. Consider, for example, a specific type of a mesocrystal composed of MNPs denoted as a *magnonic crystal* [17]. The MNPs constituting the magnonic crystal may couple via the dipole-dipole interaction which shows a $1/r^{2}$-dependence (where r is the distance between the magnetic dipoles). Due to the $1/r^{2}$-dependence, the dipolar coupling has a long-range character and, thus, it is not restricted to the interaction between the ions within an individual MNP but also affects the local environment of the MNP. In magnonic crystals composed of MNPs, the dipole-dipole interaction between the MNPs is the most prominent coupling phenomenon which yields the collective behavior of the material at the mesoscopic scale [19, 20, 21, 22, 23, 24]. It has been shown that dipolar coupling between the MNPs at the mesoscopic scale yields dispersion relations that show considerable anisotropies reflecting the symmetry of the MNP arrangement [17, 19, 23, 25, 26, 27, 28, 29, 31]. Until today, mostly theoretical investigations exist which examine the characteristics of such magnetic mesocrystals [26, 32]. These studies address, e.g., the occurrence of magnonic band gaps or the impact of the MNP diameter on the spectral features [26, 28, 33]. In order to verify these findings experimentally, the properties of the individual MNPs such as their magnetization, exchange stiffness, and anisotropy have to be understood in detail, especially as these material parameters are the key parameters determining the overall collective characteristics [26]. However, in addition to dipolar coupling between MNPs, exchange coupling between MNPs may also occur when the separation between the particles is sufficiently small to allow for either (i) electrons tunneling through a barrier from one to the other MNP [12, 34, 35] or (ii) for direct contact between the

MNPs [13, 35, 36, 37, 38, 39].

Based on the above considerations regarding the interactions between MNPs, it is intuitive that the underlying mesocrystal lattice has a crucial impact on the collective properties of the macroscopic periodic arrangement as a whole. On the one hand, the mesocrystal lattice determines the packing density and, thus, the coupling strength between the MNPs. On the other hand, the mesocrystal lattice determines the directions of high symmetry which give rise to anisotropies of the material. Since the synthesis and deposition of highly monodisperse NPs has reached outstanding precision during the past decades the fabrication of samples with various mesocrystal lattices has become possible [5, 6, 12, 41, 42]. This allows for a precise investigation of macroscopic material properties associated with the collective properties at the mesoscopic scale [25, 43]. Understanding the characteristics of individual MNPs and their collective characteristics arising from their mutual coupling is thus not only important for the development of novel technological applications, so-called "metadevices" [18], but also of great interest from a scientific point of view by characterizing the different dominant interaction regimes.

In the recent years, significant advancements have been achieved in the synthesis and deposition of MNPs, their experimental characterization, as well as their theoretical modeling simulating of appropriate model systems. This progress has contributed to a deeper understanding of the nature of MNPs and the coupling phenomena within and between them. Before turning to the findings of this thesis, it is beneficial to provide a contextual overview of the research conducted in this field, as it sets the foundation for the present investigation. In this regard, the progress made in the recent years is schematically summarized in table 1.1, where the contribution of this dissertation to the research in this field is highlighted by the gray shaded areas.

Concerning the characterization of dipolar coupling phenomena at the mesoscopic scale, first attempts have been made by investigating (dense) structured thin films using conventional fabrication techniques [22, 44, 45, 46, 47, 48, 49, 50]. These investigations have demonstrated the influence of dipolar coupling phenomena between the individual (dense) magnetic entities on the collective properties of the entire magnetic samples in terms of the spacing between the entities and their size. Due to the limitations imposed by the resolution of the employed lithographic technique ($\approx$ 100 nm for electron beam lithography), alternative fabrication techniques need to be employed in order to achieve even smaller sizes and distances of the magnetic entities. As already discussed above, chemical synthesis approaches have enabled the fabrication of NPs of sizes smaller than 100 nm [4, 6]. In previous studies, dipolar coupling phenomena have been extensively investigated and characterized in both dispersions and dried powders of MNPs of sizes of some tens of nanometers [51, 52, 53]. In these publications the mean spacing between the MNPs has been varied by adjusting the particle concentration in the dispersion or by varying the non-magnetic particle shell for MNPs in the dried powder samples. However, these approaches did not lead to an investigation of ordered MNP arrangements. A high degree of order of the MNP arrangement is important for the characterization of dipolar coupling between MNPs, since the coupling strength strongly depends on the packing density of the MNPs. Different synthesis and deposition strategies have facil-

Synthesis & NP arrangement	Experimental characterization	Theoretical characterization
(dense) structured thin films		
↓		
disordered MNP assemblies of one type of NPs		
↓	entire ensembles	analytical investigation
	↓	↓
ordered MNP arrangements of one type of NPs	spatially resolved	micromagnetic simulation
↓	↓	↓
disordered MNP assemblies of more than one type of NPs	single particle	atomistic simulation
↓		
ordered MNP arrangements of more than one type of MNP		

Table 1.1: Schematic illustration showcasing the recent advancements in the fabrication of hierarchical materials, along with their experimental characterization and theoretical modeling. The contribution of this dissertation to the research in this field is highlighted by the gray shaded areas.

itated the fabrication of highly ordered MNP arrangements [5, 6] and, thus, enabled a more detailed investigation of dipolar coupling phenomena within and between the MNPs. Nowadays, these approaches not only yield highly monodisperse MNP dispersions which is crucial for the fabrication of mesocrystals, but also open up the opportunity to deposit multiple species of NPs of appropriate size and concentrations ratios to enable the fabrication of highly ordered NP arrangements composed of more than one NP species [14, 31, 36, 41, 42]. The employment of multiple NP species arranged into highly ordered lattices is especially interesting, since this approach introduces additional anisotropies at the mesoscopic scale, which opens up unprecedented opportunities to manipulate the properties of a material at the mesoscopic scale. The results from this dissertation contribute to a profound understanding of the characteristics of individual MNP species within both ordered arrangements/ensembles and disordered assemblies, offering valuable insights of the material characteristics for potential future application that incorporate MNPs [54].

In order to obtain profound insight into the individual and collective properties of MNPs, a broad range of techniques may be employed to experimentally characterize the properties of a material [55, 56, 57, 58, 59, 60]. The most widely used methods to investigate dynamic properties of a magnetic material are radio-frequency driven spectroscopies such as ferromagnetic resonance (FMR) [61, 62, 63, 64, 65] or Brillouin light scattering experiments (BLS) [43, 66, 67]. Using, e.g., conventional FMR experiments, the sample is placed in a cavity resonator, which allows one to investigate the macroscopic response of the sample. In the (conventional) FMR experiments the magnetic structure under investigation may be fabricated multiple times on a single substrate in order to ensure sufficiently large signal intensities. The entire sample is then measured as a whole and, thus, this technique is a powerful tool for characterizing the properties of an entire array of magnetic entities. However, modern FMR approaches employ microfabricated resonators, that enable the investigation of much smaller magnetic volumes and, thus, facilitate the characterization of individual magnetic entities instead of an entire array [63, 64, 68, 69, 70, 71, 72, 73, 74]. Nevertheless, even modern FMR approaches still measure the response of the individual magnetic entities as a whole and, thus, spatially resolving the dynamic properties is not possible. BLS on the other hand possesses a spatial resolution to resolve potential magnetic oscillations of the sample [67, 75, 76, 77, 78, 79, 80, 81, 82, 83, 84]. In a BLS experiment, a focused laser beam is directed onto the sample. The laser spot can be scanned across the sample, allowing for targeted analysis of different regions. Measuring the intensity of the inelastically scattered photons as a function of the laser spot position at different external excitations frequencies and external magnetic field strengths enables the investigation of specific areas and provides valuable insights into the sample's properties. Moreover, complementary experimental techniques can be utilized to investigate the dynamic and static properties of magnetic materials. Examples of such techniques include the magneto-optic Kerr effect (MOKE) [85] and magnetic force microscopy (MFM) [61, 88, 86, 87, 62]. These methods offer spatially resolved investigations of magnetic properties, allowing for the characterization of magnetization orientations at specific locations within the magnetic sample. While in a MOKE experiment the rotation of polarized light after the reflection from a magnetized surface is probed, the goal of a MFM experiment is to map the force that is exerted on the tip of the magnetic force microscope. The information of the force distribution can subsequently be related with the magnetization orientation at specific sites of the sample. However, the spatial resolutions of BLS, MOKE, and MFM are limited by the size of the laser spot or the curvature of the MFM tip. Additional experimental techniques that enable for the investigation of properties at the level of individual particles are very rare. The most promising technique is the employment of transmission electron microscopy (TEM) and performing electron holography, which can be used to map the magnetic field distribution of single NPs [38, 89, 90, 91]. In this dissertation, (conventional) FMR experiments and BLS spectroscopy have been employed to systematically characterize the dipolar interactions between MNPs at different length scales within the mesoscopic scale.

In addition to the experimental characterization of the magnetic properties of solids, theoretical investigations are indispensable in order to interpret the experimental findings. Some of the first analytic attempts for investigating magnetic properties at the mesoscopic scale go back to, e.g., A. Aharoni who outlined the dependence of exchange dominated spin waves on the size of the MNPs [8]. Furthermore, in a subsequent publication, the influence of the surface anisotropy on the spectral features of the spin waves within an individual MNPs has been discussed [9, 92, 93]. Since these investigations focused on the exchange dominated regime, following analytical analysis focused on the transition region from quantum mechanical exchange interaction to classical dipolar interactions at the level of the individual MNPs [11]. These studies not only provide insight into the resonant behavior of the spin waves within the MNPs but also into the intensity ratios of the different spin wave modes. Based on the findings of individual MNP properties, these authors further provided a theoretical basis for collective spin wave modes of interacting MNPs [25, 32]. This theory has further been used to predict the relative intensities of the different spin wave modes of interacting MNPs by utilizing BLS experiments. Until today, this theoretical prediction has not been addressed experimentally and, thus, remains to be investigated in more detail [43]. In addition to the cited literature, further publications contributed to a profound understanding of the coupling phenomena between MNPs [19] and the resulting collective phenomena such as the formation of band gaps of a 3D magnonic crystals composed of spherical MNPs embedded in a different magnetic matrix material [26, 27, 28, 29]. In addition to the discussed analytical approaches, numerical simulations of magnetic properties are widely utilized to relate the experimentally observed features with the properties of magnetic samples. In the past, mainly finite difference methods (FDM) have been utilized to simulate the properties of a magnetic structure in the framework of *micromagnetic simulations* [94, 95, 96]. However, FDM divide the magnetic sample into cubic sub cells, which complicates the simulation of curved surfaces, since the sub cells have to be sufficiently small to adequately account for the curvature which increases the computational effort tremendously. Nowadays, finite element methods (FEM) are available to adequately mimic the curvature of magnetic structures [97]. However, both approaches simulate the magnetic properties in the framework of micromagnetic simulations. In this framework, the continuum approximation is applied and instead of simulating the individual ions of the magnetic material, the averaged magnetization and exchange stiffness of the material is used to safe computational resources. This approach is well applicable for samples with lateral lengths of some tens to hundreds of nanometers. Below these lengths, the computational effort to simulate the individual ions which possess a localized magnetic moment may be not too large. In this regard, *atomistic simulations* may be employed to model the properties of individual MNPs at the level of the constituent ions [98, 99]. The comparison between the different numerical methods along with the analytic approaches provide a complementary basis for characterizing the magnetic properties at the mesoscopic scale to obtain a profound understanding of the nature at this scale.

In the following, chapter 2 "Introduction to Magnetism" provides a brief overview of the theoretical foundations of magnetism in solids. Subsequent to the theoretical basics, chapter 3 "Methods" discusses general aspects of the sample fabrication, the characterization techniques employed, and the basics of the theoretical modeling approach. The summary of the results obtained during this work is given in chapter 4 "Summary of Results". This work finally closes with chapter 5 "Conclusion and Outlook" where a brief outlook for future investigations based on the findings of this work is provided.

2 Introduction to Magnetism

In advance to addressing the findings of this dissertation, it may be convenient to first introduce the theoretical basics of magnetism. The physical phenomena related to magnetism in solids can be classified into three categories according to the macroscopic response of the material to an external magnetic field. These responses are referred to (i) diamagnetism, (ii) paramagnetism and (iii) collective magnetism [60, 100, 101, 102, 103, 104]. Within each category, magnetic materials may be further classified by their electric conductivity, which has a crucial impact on the magnetic properties of the solid. In insulating materials, the diamagnetic response can be understood within the framework of *Larmor-diamagnetism* [102]. On the other hand, metallic solids exhibit a diamagnetic response originating from the response of conduction electrons to the external field which is generally known as *Landau-diamagnetism* [106]. The paramagnetic response of insulating materials may be described by the *Curie law* and in the theoretical framework of *Langevin-paramagnetism* [102]. On the other hand, the paramagnetic properties of metallic solids may be described by the theory of *Pauli-paramagnetism* [105]. Unlike diamagnetic or paramagnetic materials, which do not exhibit a spontaneous alignment of the individual magnetic moments without the presence of a significant external magnetic field due to the absence or weakness of explicit interactions, the phenomenon of collective magnetism in solids emerges from the specific interactions between individual magnetic moments. These interactions between magnetic moments give rise to an ordered alignment of the magnetic moments, leading to magnetic states such as ferro-, ferri-, antiferro-, and antiferrimagnetism. Such materials may show a *spontaneous magnetization* below a critical temperature. This spontaneous magnetization is ascribed to the presence of permanent magnetic moments which are either *localized* at the ions on the crystal lattice or *itinerant* and, thus, delocalized throughout the solid [102]. In general, the magnetic response of a solid arises from contributions of different magnetic interactions, and the classification of a solid into dia-, para- or collective magnetism is based on its most dominant magnetic response to an external magnetic field. While all solids exhibit diamagnetism, this property may be superimposed by the paramagnetic or ferromagnetic behavior of the material [102]. In the following section, a brief discussion of ferromagnetic interactions is provided. For a more comprehensive theoretical understanding of magnetism in solids, the reader is referred to the cited literature and the references provided at the end of this chapter.

From a classical point of view within the scope of Maxwell's equations, magnetic moments can interact with one another via the dipole-dipole interaction [10]. For instance, consider two neighboring ions in a solid with a typical separation $r = \left|\overrightarrow{r}\right|$ of a few

Ångstroms. Each ion possesses a magnetic moment $\vec{m}$ with a typical value of a few *Bohr magnetons* μ_B. The resulting dipole-dipole interaction $\mathcal{H}_{dd}$ given by

$$\mathcal{H}_{dd} = \frac{\mu_0}{4\pi r^3}\left(\vec{m}_i\vec{m}_j - \frac{3\cdot\left(\vec{m}_i\vec{r}\right)\left(\vec{m}_j\vec{r}\right)}{r^3}\right) \tag{2.1}$$

yields an energy in the range of $\approx 10^{-26}$ J, which corresponds to a thermal energy of $E_{th} = k_B T$ with $T \approx 2$ K. Here μ_0 represents the magnetic field constant. Thus, the dipole-dipole interaction is much too weak to explain ferromagnetic ordering at elevated temperatures up to ≈ 1400 K [103]. This circumstance already indicates that magnetic properties of solids cannot be described in the framework of classical physics. Moreover, the *Bohr-van Leuween-theorem* states that for a classical system at thermal equilibrium the average magnetic moment vanishes [107, 108]. It follows that magnetism in solids is inherently subject to the principles of quantum mechanics, which will be exemplified in the case of ferromagnetic materials in the following.

At the beginning of the 20th century, in the course of the development of quantum mechanics, W. Heisenberg and P. Dirac discovered that the origin of ferromagnetic ordering in magnetic materials is related to the exchange interaction resulting from the indistinguishability of electrons as identical particles [110, 111]. To introduce this interaction, a simple system consisting of two hydrogen atoms is considered [102]. First, the two atoms can be thought of as isolated when they are separated by an infinite distance. In this case, the associated Hamiltonian of the isolated atoms $\mathcal{H}^{(0)}$ is simply the sum of the two individual one-particle Hamiltonians and the wavefunction reads

$$|\phi\rangle^{(\pm)} = \frac{1}{\sqrt{2}}\left(|\phi_a^{(1)}\rangle\,|\phi_b^{(2)}\rangle \pm |\phi_a^{(2)}\rangle\,|\phi_b^{(1)}\rangle\right), \tag{2.2}$$

where $|\phi_{a/b}^{(1/2)}\rangle$ are the one-particle hydrogen wave functions of the two electrons. By decreasing the distance between the atoms, the Coulomb interaction between the electrons and protons increases and the system can no longer be considered isolated. The Hamiltonian then reads

$$\mathcal{H} = \underbrace{\frac{1}{2m_e}\left(\vec{p}_1^{\,2} + \vec{p}_2^{\,2}\right) - \frac{e^2}{4\pi\epsilon_0}\left(\frac{1}{r_{a1}} + \frac{1}{r_{b2}}\right)}_{=\mathcal{H}^{(0)}} + \underbrace{\frac{e^2}{4\pi\epsilon_0}\left(\frac{1}{R_{ab}} + \frac{1}{r_{12}} + \frac{1}{r_{b1}} + \frac{1}{r_{a2}}\right)}_{=\mathcal{H}^{(1)}} \tag{2.3}$$

which cannot be solved analytically. Here, $\vec{p}_{1,2}$ are the momentum operators of the two electrons, m_e and e are the mass and the charge of the electron, ϵ_0 is the electric field constant, and the distances r_{a1}, r_{b2}, R_{ab}, r_{12}, r_{b1}, and r_{a2} are schematically depicted in figure 2.1 [102]. Thus, for $\mathcal{H}^{(1)} \neq 0$ (finite distance) the solution can only be approximated by applying, e.g., the variation principle. Using the wavefunction of the isolated atoms $|\phi_{a/b}^{(1/2)}\rangle$ given in equation 2.2 as the variation ansatz and considering $\mathcal{H}^{(1)}$ as a perturbation, then the energy of the system is given by

$$E^{(\pm)} = E^{(0)} + \frac{C \pm J^{\text{exc}}}{1 \pm S}, \tag{2.4}$$

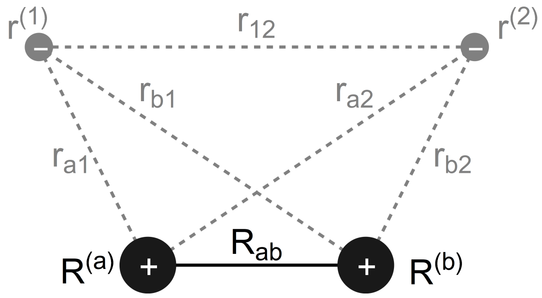

Figure 2.1: Schematic drawing of the different distances between the electrons ($r^{(1)}$ and $r^{(2)}$) and the nuclei ($R^{(a)}$ and $R^{(b)}$) in a hydrogen molecule.

where

$$\begin{aligned} C &= \langle \phi_a(\vec{r}_1)\phi_b(\vec{r}_2)|\, \mathcal{H}^{(1)}\, |\phi_a(\vec{r}_1)\phi_b(\vec{r}_2)\rangle && \text{denotes the ”Coulomb integral”,} \\ S &= \langle \phi_a(\vec{r}_1) \mid \phi_b(\vec{r}_1)\rangle && \text{the ”overlap integral”,} \\ J^{\text{exc}} &= \langle \phi_a(\vec{r}_1)\phi_b(\vec{r}_2)|\, \mathcal{H}^{(1)}\, |\phi_a(\vec{r}_2)\phi_b(\vec{r}_1)\rangle && \text{the ”exchange integral”,} \end{aligned}$$

and $E^{(0)}$ the energy of the isolated system. So far, only the orbital wave function $|\phi\rangle^{(\pm)}$ has been considered being either symmetric $|\phi\rangle^{(+)}$ or antisymmetric $|\phi\rangle^{(-)}$ under the exchange of the electrons. However, a fundamental property of an electron, its spin, has not been taken into account yet. This property has been experimentally observed by O. Stern and W. Gerlach [112] and theoretically described by P. Dirac [111]. As these findings have far-reaching implications, it is convenient to briefly discuss the fundamental characteristics of an electron and the associated phenomena. These include the electron's nature as a spin-1/2 particle, which gives rise to a magnetic moment of the electron that may couple with a magnetic field. Furthermore, relativistic corrections to the Hamiltonian $\mathcal{H}^{(0)}$ can be introduced, giving rise to, e.g., the spin-orbit interaction. Central to this understanding is the *Dirac equation*, which is the result of linearizing the *Schrödinger equation* in the context of relativistic generalization. In the following, a brief overview of the ideas and consequences is provided. For a detailed analysis of this theory, the reader is referred to the references [100, 101, 102]. To begin with, the energy E of a free classical relativistic electron of mass m_e is given by:

$$E = c^2 \vec{p}^{\,2} + m_e^2 c^4 \tag{2.5}$$

where c is the velocity of light, $\vec{p} = \tilde{\gamma} m_e \left(v_x, v_y, v_z\right)$ is the relativistic mechanical momentum, and $\tilde{\gamma} = \left(1 - v^2/c^2\right)^{-1/2}$ the *Lorentz factor*. Applying *Schrödinger's correspondence principle*

$$E \rightarrow i\hbar \frac{\partial}{\partial t} \quad \text{and} \quad \vec{p} \rightarrow \frac{\hbar}{i}\nabla, \tag{2.6}$$

where $\hbar$ is the reduced *Planck constant* and i is the imaginary number, the *Klein-Gordon equation* for the wavefunction $|\psi\rangle$ of the free electron is obtained:

$$\left(\Delta - \frac{1}{c^2}\frac{\partial^2}{\partial t^2} - \frac{m_e^2 c^2}{\hbar^2}\right)|\psi\rangle = 0. \tag{2.7}$$

Upon attempting to solve this equation, a notable complication arises. Equation 2.7 represents a second-order differential equation with respect to time t, necessitating the provision of two initial conditions for both $|\psi\rangle$ and its derivative $|\dot{\psi}\rangle$ in order to obtain a solution. Since the non-relativistic Schrödinger equation is linear in time t, it is reasonable to assume that its relativistic generalization should also be linear with respect to time t, since the introduction of relativity should not alter the initial conditions. Dirac's idea to overcome this complication was to linearize eq. 2.7 by introducing the operators α_i and β with

$$\begin{aligned} \alpha_i\alpha_j + \alpha_j\alpha_i &= 2\delta_{ij}, \\ \alpha_i\beta + \beta\alpha_i &= 0, \\ \beta^2 &= 1. \end{aligned} \tag{2.8}$$

These relations yield:

$$\hat{\alpha} = \begin{pmatrix} 0 & \vec{\sigma} \\ \vec{\sigma} & 0 \end{pmatrix} \quad \text{and} \quad \hat{\beta} = \begin{pmatrix} \mathbb{1}_2 & 0 \\ 0 & -\mathbb{1}_2 \end{pmatrix}, \tag{2.9}$$

where $\vec{\sigma}$ is given by the *Pauli spin matrices* σ_i with

$$\vec{\sigma} = \left(\sigma_x, \sigma_y, \sigma_y\right), \text{ and } \sigma_x = \begin{pmatrix} 0 & 1 \\ 1 & 0 \end{pmatrix}, \sigma_y = \begin{pmatrix} 0 & -i \\ i & 0 \end{pmatrix}, \ \& \ \sigma_z = \begin{pmatrix} 1 & 0 \\ 0 & \text{-1} \end{pmatrix}, \tag{2.10}$$

where $\mathbb{1}_2$ is the 2×2 identity matrix. With that, eq. 2.7 can be transformed into

$$\left(i\hbar\frac{\partial}{\partial t} - c\alpha \cdot \vec{p} - \beta m_e c^2\right)|\psi\rangle = 0, \tag{2.11}$$

which is the *Dirac equation* for a free electron. The corresponding *Dirac Hamiltonian* $\mathcal{H}_D^0$ can be defined by

$$\begin{aligned} i\hbar\frac{\partial}{\partial t}|\psi\rangle &= \mathcal{H}_D^0\,|\psi\rangle\,, \text{ where} \\ \mathcal{H}_D^0 &= c\hat{\alpha}\vec{p} + \hat{\beta}m_e c^2, \end{aligned} \tag{2.12}$$

with the associated energy eigenvalues $E = \pm\sqrt{c^2p^2 + m_e^2c^4}$. The positive (negative) sign of the energy eigenvalue corresponds to the solution for the electron (positron), which is doubly degenerate with the corresponding eigenvectors $\vec{a}_1$ and $\vec{a}_2$. By defining the *Dirac spin operator* as

$$\hat{s} = \frac{\hbar}{2}\hat{\sigma} \quad \text{with} \quad \hat{\sigma} = \begin{pmatrix} \vec{\sigma} & 0 \\ 0 & \vec{\sigma} \end{pmatrix}, \tag{2.13}$$

it can be shown that $\vec{a}_1$ and $\vec{a}_2$ are also eigenvectors of $\hat{s}$ with

$$\hat{s}\vec{a}_1 = +\frac{\hbar}{2}\vec{a}_1 \quad \text{and} \quad \hat{s}\vec{a}_2 = -\frac{\hbar}{2}\vec{a}_2. \tag{2.14}$$

The resulting eigenstates can be interpreted as a "new" quantum number, the *spin* of the electron with the eigenvalues being $\pm\hbar/2$. The above consideration of a free relativistic electron can be extended to the case of an electron in the presence of an electromagnetic field. This can be done by substituting the mechanical momentum with the canonical momentum of the electron in an electromagnetic field in the Dirac equation (eq. 2.11) and including an electrostatic potential φ_e by

$$\vec{p} \rightarrow \vec{p} + e\vec{A} \quad \text{and} \quad E \rightarrow E + e\varphi_e, \tag{2.15}$$

where $\vec{A}$ is the magnetic vector potential. This yields the Dirac Hamiltonian of an electron in an electromagnetic field $\mathcal{H}_D$ with

$$\mathcal{H}_D = c\hat{\alpha}(\vec{p} + e\vec{A}) + \hat{\beta} m_e c^2 - e\varphi_e. \tag{2.16}$$

In the non-relativistic limit, where the velocity v is much smaller than the speed of light c and, thus, $\tilde{\gamma} \ll 1$, the Dirac Hamiltonian $\mathcal{H}_D$ may be transformed into the *Pauli Hamiltonian* $\mathcal{H}_P$ with,

$$\mathcal{H}_P = \frac{1}{2m_e}\left(\vec{p} + e\vec{A}\right)^2 + \frac{2\mu_B}{\hbar}\left(\vec{s} \cdot \vec{B}\right) - e\varphi_e, \tag{2.17}$$

where $\vec{s}(=\hbar/2 \cdot \vec{\sigma})$ is the spin of the electron with the corresponding eigenvalues $\pm\hbar/2$ and $\mu_B = e\hbar/2m_e$ the *Bohr magneton*. An important consequence of this derivation is that the spin of the electron is associated with a magnetic moment $\vec{m}_s = -g\mu_B/\hbar \cdot \vec{s}$ ($g = 2$ is the *Landé-factor* of the electron) which may couple to a magnetic field $\vec{B}$. The full derivation of $\mathcal{H}_D$ in the non-relativistic limit is somewhat extensive and, thus, the reader is referred to the literature [100, 101, 102] for a more detailed analysis and here only the *spin-orbit coupling* arising from the coupling of the electron's spin $\vec{s}$ with the magnetic field $\vec{B}$ is discussed.

As the electron performs an "orbital motion" around the nucleus which is associated with an angular momentum, this motion induces a magnetic field which couples to the magnetic moment of the electron $\vec{m}_s$. This is described by the spin-orbit interaction Hamiltonian $\mathcal{H}_{so}$ by

$$\mathcal{H}_{so} = -\frac{e}{2m_e^2c^2}\left[\left(\nabla\varphi_e \times \vec{p}\right) \cdot \vec{s}\right] = -\frac{e}{2m_e^2c^2}\left(\frac{1}{r}\frac{d\varphi_e}{dr}\right)\left(\vec{l} \cdot \vec{s}\right) = \lambda_{so}\left(\vec{l} \cdot \vec{s}\right), \tag{2.18}$$

where

$$\varphi_e(r) = \frac{Z^* e}{4\pi\epsilon_0 r}, \quad \nabla\varphi_e(r) = \frac{\vec{r}}{r}\frac{d\varphi_e}{dr} \quad \text{and} \quad \lambda_{so} = \frac{1}{8\pi\epsilon_0 m_e^2 c^2} \cdot \frac{Z^* e^2}{r^3} \tag{2.19}$$

has been exploited. Here λ_{so} is the spin-orbit coupling constant, $\vec{l} = \vec{r} \times \vec{p}$ is the angular momentum of the electron, Z^* the (screened) number of nuclear charges, ϵ_0 the electric field constant, and r the distance of the electron to the nucleus. As a consequence, even in the absence of an external magnetic field, there exists an "internal" magnetic field which couples the magnetic moment and thus the spin of the electron to its orbital angular momentum. This interaction gives rise to the magnetocrystalline anisotropy, which will be discussed in more detail below. Before that, we return to the discussion of exchange interaction that gives rise to the collective alignment of the magnetic moments of the ions within a magnetic solid.

In order to address the quantum mechanical exchange interaction, we now return to the perturbation ansatz introduced by equations 2.3 and 2.4, and construct the total wavefunction $|\psi\rangle$ as the product of the orbital wavefunction $|\phi\rangle$ and the spin wavefunction $|\chi\rangle$ by

$$|\psi^{(1,2)}\rangle = |\phi\left(\vec{r}_1, \vec{r}_2\right)\rangle^{(\pm)} \cdot |\chi\left(\vec{s}_1, \vec{s}_2\right)\rangle \tag{2.20}$$

with the spin orientations $\vec{s}_1$ and $\vec{s}_2$ of the two electrons [102]. Since electrons are spin-1/2 particles and, thus, follow *Fermi-Dirac-statistics* and the *Pauli exclusion principle*, the total wavefunction $|\psi\rangle$ of the fermionic system is required to be antisymmetric under the exchange of the electrons $|\psi^{(1,2)}\rangle = -|\psi^{(2,1)}\rangle$. Taking into account that the symmetric solution of the orbital wavefunction $|\phi\rangle^{(+)}$ represents the binding (ground) state of the hydrogen molecule, the spin wavefunction $|\chi\rangle$ is required to be antisymmetric to fulfill the Pauli exclusion principle. In order to reflect this circumstance in the Hamiltonian $\mathcal{H}$ which acts on the total wavefunction $|\psi\rangle = |\phi\rangle \cdot |\chi\rangle$, an effective Hamiltonian $\mathcal{H}^{(\mathrm{eff})}$ may be constructed such that the symmetry of the total wavefunction $|\psi\rangle$ is always antisymmetric under the exchange of the electrons. By introducing the exchange constant $\mathcal{J}$ defined as

$$\mathcal{J} = E^{(+)} - E^{(-)}, \tag{2.21}$$

$\mathcal{H}^{(\mathrm{eff})}$ can be written as

$$\begin{aligned} \mathcal{H}^{(\mathrm{eff})} &= -\frac{1}{\hbar^2}\mathcal{J} \cdot \vec{s}_1\vec{s}_2 \quad \text{and, thus,} \\ \mathcal{H}^{(\mathrm{eff})} &= -\frac{1}{\hbar^2}\sum_{i\neq j}\mathcal{J}_{\mathrm{ij}} \cdot \vec{s}_{\mathrm{i}}\vec{s}_{\mathrm{j}}, \end{aligned} \tag{2.22}$$

where the second equation is the generalization of the effective Hamiltonian to a set of interacting spins and their associated magnetic moments [102]. This type of exchange interaction is denoted as the *direct exchange interaction* since the localized magnetic moment of an ion interacts with the magnetic moment of its neighboring ion directly via the overlap of the corresponding wave functions. As a result, the magnetic moments of the ions show an ordered alignment giving rise to collective magnetic properties of the solid. In a wide range of scenarios, the magnetic moments of ions are primarily associated with the spins of electrons occupying partially filled orbitals. However, it is important to consider that the total magnetic moment of an ion may also incorporate contributions from the orbital angular momentum of the electrons.

However, in most magnetic solids the direct exchange interaction is not responsible for the collective magnetism of the localized magnetic moments of the ions, since the distances between the ions are too large and, thus the overlap of the wave functions becomes too small [113]. Exchange interactions in magnetic solids primarily occur in a different fashion, such as *indirect* and *itinerant exchange interaction*. Prior to discussing the indirect exchange interactions of magnetic oxides such as magnetite (Fe_3O_4), the material investigated over the course of this dissertation, some aspects concerning collective magnetism in metals should be briefly emphasized. Collective magnetism in metals may occur either (i) due to the interaction of localized magnetic moments of the ions with delocalized conduction electrons giving rise to the *Rudermann-Kittel-Kasuya-Yosida (RKKY) interaction*, or due to (ii) the spontaneous polarization of delocalized electrons as a result of an energetic shift of the spin-polarization dependent density of states

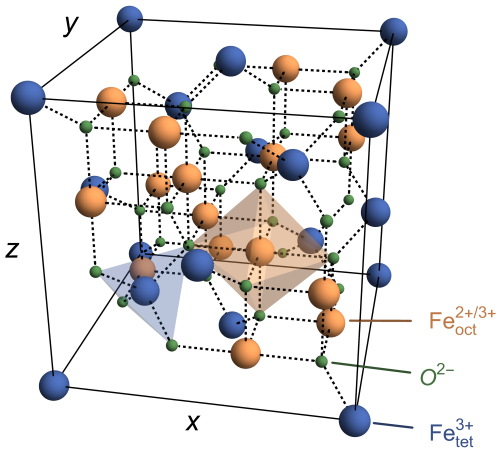

Figure 2.2: The crystal structure of magnetite (Fe_3O_4) is built of two sublattices A and B. On sublattice A, Fe^{3+} ions (blue spheres) are tetrahedrally coordinated by oxygen ions (green spheres), which is highlighted by the faint blue tetrahedron. On sublattice B, Fe^{3+} and Fe^{2+} ions (orange spheres) are octahedrally coordinated by oxygen ions and equally distributed, which is highlighted by the faint orange octahedron.

yielding *itinerant* or *band ferromagnetism* [102]. Both of the interactions require highly mobile electrons and, thus, these interactions predominantly occur in materials such as metals which are good electrical conductors. Since the electron mobility in insulating magnetic materials is very low, their macroscopic magnetic properties ascribed to the ordered alignment of localized magnetic moments relies on different coupling phenomena between the localized magnetic moments. In the following, the two most relevant indirect exchange interactions occurring in magnetic oxides are discussed using magnetite (Fe_3O_4) as an example [113].

Within magnetite, iron ions are distributed on two sublattices, which is exemplified in figure 2.2 [114]. On sublattice A, Fe^{3+} ions are tetrahedrally coordinated by oxygen ions, and on sublattice B, Fe^{2+} and Fe^{3+} ions are equally distributed and octahedrally coordinated by oxygen ions [115]. The magnetic interaction between the iron ions is mediated by the oxygen ions between them and depends on the valence and the bond angle of the associated iron ions [113].

For interacting iron ions of the same valence, such as Fe^{3+}_{tet} and Fe^{3+}_{oct}, the *superexchange interaction* is the interaction responsible for an alignment of the magnetic moments of the two iron ions. Figure 2.3 (a) schematically depicts this circumstance for a bond angle of 180° and 90°. First, we consider the 180° bond angle. The spins of the five *d*-electrons of each iron ion show parallel alignment according to *Hund's rules* [102]. The electrons involved in the bond between the iron ions and the oxygen ion may "hop" between the iron and the oxygen ion simultaneously, which is illustrated by the dotted arrows. Since the p_x-orbital of the oxygen ion may be occupied by two electrons only and, thus, is completely filled as depicted in the figure, the electrons within this orbital are aligned antiparallel according to Hund's rules. Thus, due to the Pauli principle, the bond between the oxygen ion and the iron ions yields antiparallel alignment of the

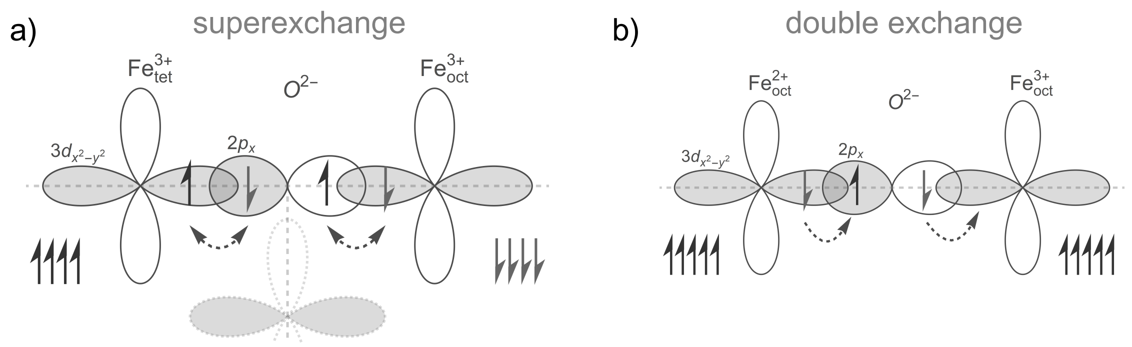

Figure 2.3: Schematic illustration of indirect exchange interactions associated with hopping of electrons between orbitals. The dotted arrows indicate the associated simultaneous "hopping" processes. The continuous black and gray arrows close to the iron ions indicate the electrons that do not contribute to the bond to the oxygen ion, while the electron in the irons $d_{\mathrm{x}^2-\mathrm{y}^2}$-orbital forms the bond to the oxygen's ion p_x-orbital. The sign of the involved $d_{\mathrm{x}^2-\mathrm{y}^2}$- and p_x-orbitals are indicated by white and gray shading for negative and positive sign of the wavefunction, respectively. a) Superexchange occurs when transition-metal ions of the same valance interact via the mediation of the oxygen ion. This interaction is highly antiferromagnetic for a 180° bond angle and slightly ferromagnetic for 90° bond angles (depicted by faint $d_{\mathrm{x}^2-\mathrm{y}^2}$-orbital underneath the oxygen ion). Superexchange in magnetite is most prominent for the interaction between the two sublattice iron ions $\mathrm{Fe}^{3+}_{\mathrm{tet}}$ and $\mathrm{Fe}^{3+}_{\mathrm{oct}}$. b) Double exchange occurs in mixed valences, such as the $\mathrm{Fe}^{2+}_{\mathrm{oct}}$ and $\mathrm{Fe}^{3+}_{\mathrm{oct}}$ ions on the octahedral sites of the magnetite crystal. This yields a ferromagnetic alignment of the two magnetic moments of the iron ions.

associated spins of the electrons and, therefore, results in antiparallel alignment of the associated magnetic moments of the two iron ions [113]. Figure 2.3 (a) demonstrates the antiparallel alignment resulting from a bond angle of 180°. In the figure, the bond of the iron ions to the oxygen ion is illustrated using atomic orbitals, which are constructed by linear combinations of the spherical harmonics $\mathcal{Y}_l^m$ with l and m as the azimuthal and magnetic quantum number. This yields the $d_{\mathrm{x}^2-\mathrm{y}^2}$-orbital $\left(= 1/\sqrt{2}\left(\mathcal{Y}_2^2 + \mathcal{Y}_2^{-2}\right)\right)$ of the iron ions and the oxygen's p_x-orbital $\left(= 1/\sqrt{2}\left(\mathcal{Y}_1^1 - \mathcal{Y}_1^{-1}\right)\right)$, where each orbital may be occupied by a maximum of two electrons with antiparallel aligned spin. In addition, fig. 2.3 (a) also illustrates the interaction of the two iron ions mediated by the oxygen ion for a 90° bond angle, as indicated by the faintly depicted $d_{\mathrm{x}^2-\mathrm{y}^2}$-orbital underneath the oxygen ion. It should be highlighted that the alignment of the spin orientations of the two iron ions depends on the overlap of the associated iron and oxygen wave functions and, thus, the signs of the wave functions. It can concluded that overlap becomes zero for a bond angle of 90°, which can be understood by considering the upper (white and thus negative) lobe of the faintly depicted iron ions $d_{\mathrm{x}^2-\mathrm{y}^2}$-orbital that overlaps with both the positive and negative lobes of the oxygen's p_x-orbital. This results in a net overlap of zero and, thus, the two iron ions are no longer solely coupled via the p_x-orbital but via a combination of the p_x- and p_y-orbitals. Since the virtual hopping process of the two oxygen p_x- and p_y-electrons results in two holes at the oxygen ion, Hund's rules imply parallel alignment of the remaining p_x- and p_y-electrons and, thus, lead to a weak ferromagnetic magnetic ordering of the iron ions [113, 114, 115]. This angle-dependent ordering of magnetic ions interacting via superexchange has been thoroughly studied and is summarized within the framework of the *Goodenough-Kanamori-Anderson rules* [113].

The interaction between the localized magnetic moments of the ions changes when iron ions of different valences interact with each other via the mediation of the oxygen ion between them. Consider the interaction between the $\mathrm{Fe}^{2+}_{\mathrm{oct}}$ and $\mathrm{Fe}^{3+}_{\mathrm{oct}}$ ions within the octahedral sublattice as depicted in figure 2.3 (b). Since the $\mathrm{Fe}^{2+}_{\mathrm{oct}}$ ion possesses one electron more than a half-filled *d*-orbital, this additional electron shows an antiparallel alignment of its spin with respect to the orientation of the other five *d*-electrons of this ion. To fulfill Hund's rules, the simultaneous hopping process of the associated electrons to the neighboring $\mathrm{Fe}^{3+}_{\mathrm{oct}}$ ion via the oxygen ion then favors parallel alignment of the five *d*-electrons of each iron ion. This so-called *double exchange interaction* yields ferromagnetic ordering of the magnetic moments of the iron ions involved [102]. Thus, it follows that the localized magnetic moments of the $\mathrm{Fe}^{2+}_{\mathrm{oct}}$ and $\mathrm{Fe}^{3+}_{\mathrm{oct}}$ ions on sublattice B show parallel alignment with respect to each other. On the other hand, the superexchange interaction between the localized magnetic moments of the $\mathrm{Fe}^{3+}_{\mathrm{tet}}$ and $\mathrm{Fe}^{3+}_{\mathrm{oct}}$ ions on the two sublattices A and B yields antiparallel alignment. As a result, the total net magnetic moment of magnetite relates exclusively to the $\mathrm{Fe}^{2+}_{\mathrm{oct}}$ ions since the $\mathrm{Fe}^{3+}_{\mathrm{tet}}$ and $\mathrm{Fe}^{3+}_{\mathrm{oct}}$ ions are present in equal amounts and their magnetic moments oppose each other [114].

However, the interactions discussed above explain the ordered alignment of the localized magnetic moments of the ions within a magnetic solid only. The effective Hamiltonian constructed to describe the exchange interaction between the localized magnetic moments of adjacent ions in equation 2.22 is isotropic and solely relies on the relative orientations of the magnetic moments with respect to one another. In general, magnetic materials show magnetic anisotropies, which give rise to preferred orientation of the ions' magnetic moments along specific spatial directions, which cannot be explained by equation 2.22 alone [102, 116, 117]. Such anisotropic behavior is observed experimentally, for instance, by measuring hysteresis curves [109] or by investigating dispersion relations of spin waves along different directions [118], which yields deviations between these specific spatial directions. The origin of such preferential orientations of the magnetic moments of the ions can be ascribed to two different properties of a magnetic material, which are related to the crystalline structure of the solid and its shape [119, 120].

At the atomic scale, the crystalline structure of the solid gives rise to the *magnetocrystalline anisotropy* [66, 116]. The origin of this anisotropy lies in the coupling of the magnetic moments of the ions with the crystal lattice which determines the symmetry of the anisotropy. On the one hand, the magnetic moment of an ion may couple via dipole-dipole interaction $\mathcal{H}_{\mathrm{dd}}$ (see eq. 2.1) with the magnetic moment of its neighboring ions. Since the ions are organized on the specific atomic sites, the dipole-dipole interaction gives rise to preferred orientations of the individual magnetic moments with respect to the crystal lattice. However, this interaction is typically very weak and, thus, makes a minor contribution to the magnetocrystalline anisotropy. On the other hand, the predominant contribution to the magnetocrystalline anisotropy arises from the interaction of the electron's spin with its orbital motion at the ion. The coupling of the electron's spin with its orbital angular momentum $\vec{l}$ is described by the spin-orbit interaction $\mathcal{H}_{\mathrm{so}}$

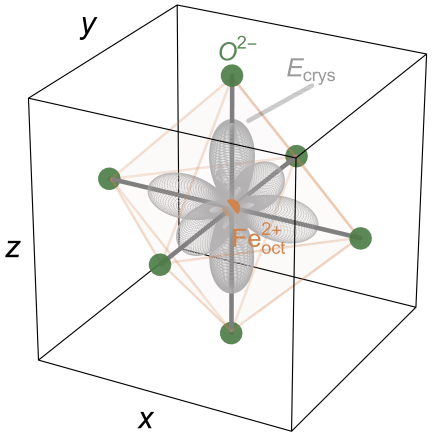

Figure 2.4: Representation of the magnetocrystalline energy surface $E_{\mathrm{crys}}(\vec{m})$ for different orientations of the magnetic moment $\vec{m}$ of an octahedrally coordinated $\mathrm{Fe}^{2+}_{\mathrm{oct}}$ ion (depicted as the orange sphere) in magnetite as a result of the interaction of the iron ion with the surrounding oxygen ions (depicted in green). The corresponding magnetic hard axes are along the <100>-directions, whereas the magnetic easy axes are parallel to the <111>-directions.

given by eq. 2.18. Since the ions are organized on a crystal lattice, as exemplified in the case of magnetite in fig. 2.2, their corresponding electron orbitals are thus spatially fixed relative to the neighboring ions. Consequently, the orbital angular moment $\vec{l}$ associated with the orbital motion of the electron also reflects the symmetry of the crystal. As $\vec{l}$ is spatially fixed and the orientation of the electron's magnetic moment associated with its spin is coupled to $\vec{l}$ via $\mathcal{H}_{\mathrm{so}}$, there exist preferred orientations of the magnetic moment of the ion which coincide with the crystal's directions of high symmetry. As a consequence, preferential stable orientations of the ion's magnetic moments may form, which are usually denoted as *easy axes* since these orientations correspond to a minimum energy. *Hard axes* on the other hand, reflect orientations of the ion's magnetic moments that correspond to a maximum in energy. Until today, there is no satisfactory theory to relate the magnetocrystalline anisotropy to the fundamental quantum mechanical characteristics of the material [121]. Thus, a phenomenological approach is utilized, which employs an expansion of the crystal field by introducing the crystal field potential $V(\vec{r})$ that reflects the crystal symmetry [116]. In the case of cubic crystal symmetry as observed for magnetite (see fig. 2.2), the energy associated with the orientation of the magnetic moment of the ions results in a cubic symmetry of the magnetocrystalline anisotropy energy and, thus, can be written as [95, 116]

$$E_{\mathrm{crys}}(\vec{m}) = \frac{2K_1 V}{M_{\mathrm{sat}}}\left(\left(m_x^2+m_y^2\right)\cdot m_z^2+\left(m_x^2+m_z^2\right)\cdot m_y^2+\left(m_z^2+m_y^2\right)\cdot m_x^2\right)+\ldots \tag{2.23}$$

where K_1 is the first-order anisotropy constant, V is the volume of the magnetic solid, M_{sat} its saturation magnetization and the m_i are the normalized components of the magnetic moments $\vec{m}$ of the ions that constitute the solid. Usually, it is sufficient to consider the first-order term only, as the contribution of higher orders is much smaller

geometry		N_x	N_y	N_z
sphere:	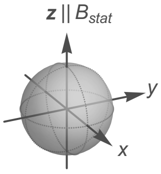	1/3	1/3	1/3
cylinder:	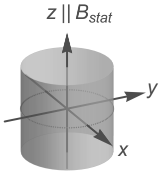	1/2	1/2	0
thin film:	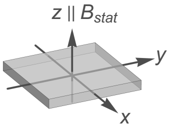	0	0	1

Table 2.1: Demagnetization factors of a sphere, a cylinder and a thin film. The external field B_{stat} is applied along the z-axis [122].

[66]. In the crystal field approach, the interaction of the iron ion's $3d$-electrons with the crystal field may be repulsive or attractive [116], which in the case of magnetite yields the preferred orientations (magnetic easy axes) of the magnetic moment $\vec{m}$ orientated along the diagonals of the cube and, thus, along the <111>-directions. Figure 2.4 depicts the energy surface E_{crys} of the octahedrally coordinated $\text{Fe}^{2+}_{\text{oct}}$ ion in magnetite being enhanced for $\vec{m}$ pointing towards an oxygen ion (<100>-directions – magnetic hard axes) and being lowered for the intermediate orientation. Thus, the interactions of the ions at the atomic scale contribute to magnetic anisotropies of the magnetic material. In addition to the occurrence of magnetic anisotropies related to the atomic arrangement on the crystal lattice, the finite size of the solid introduces boundary conditions that affect the magnetostatics of the magnetic solid giving rise to contributions to the magnetic anisotropies at the mesoscopic and macroscopic scale [10, 30, 123].

Consider a uniformly magnetized solid, i.e., $\text{div}(\vec{M}(\vec{r})) = \nabla\vec{M} = 0$, where $\vec{M}(\vec{r}) = d\vec{m}(\vec{r})/dV$ is the magnetization with $\vec{m}(\vec{r})$ the magnetic moment located at $\vec{r}$ and V the volume. Then, a contribution to the magnetic anisotropy arises from effective magnetic surface charges σ_{M} at the surface of the solid creating a magnetic surface potential φ_{M}, which may be written as

$$\begin{aligned} \nabla^2\varphi_{\text{M}} = \Delta\varphi_{\text{M}} = -\sigma_{\text{M}} = \vec{n}\cdot\vec{M} \\ \text{and, thus,}\quad \varphi_{\text{M}} = \frac{1}{4\pi}\oint_S \frac{\vec{n}\cdot\vec{M}}{\vec{r}-\vec{r}\,'}\text{d}\vec{r}\,'. \end{aligned} \tag{2.24}$$

Here φ_M is the magnetic scalar potential and $\vec{n}$ the normal vector of the surface S of the solid. As a result, the particular geometry of the surface S and therefore the shape of the magnetic body determines φ_M. By using

$$\begin{aligned} \vec{B}_{\text{shape}} &= -\mu_0 \nabla \varphi_M \\ E_{\text{shape}} &= -\vec{m} \cdot \vec{B}_{\text{shape}} \end{aligned} \tag{2.25}$$

the associated *demagnetizing field* $\vec{B}_{\text{shape}}$ and demagnetization energy E_{shape} related to the shape of the magnetic entity can be calculated referring to the so-called *shape anisotropy* [10]. In general, the analytical calculation for arbitrarily shaped solids is hardly feasible and therefore usually performed numerically [120, 124, 125, 126, 127]. This becomes particularly sophisticated when dealing with periodic structures in which isolated magnetic solids are arranged into highly ordered assemblies [128, 129]. However, some special geometries should be emphasized here since these play an important role in the analysis of the results of the FMR and BLS measurements performed in this work. In the special case of ellipsoidal bodies [117, 124], the demagnetization field can be represented by introducing a demagnetization tensor $\underline{\underline{N}}$ by

$$\vec{B}_{\text{shape}} = 4\pi\mu_0 \cdot \underline{\underline{N}} \cdot \vec{M}. \tag{2.26}$$

Here, $\underline{\underline{N}}$ is a tensor of rank 2, whose trace equals 1 and whose only non-zero elements are its diagonal elements. This yields, e.g., the demagnetizing factors given in table 2.1 for a sphere, a cylinder and a thin film [119, 122]. Here, the spherical and thin film demagnetization tensors are especially important for the particular experiments performed over the course of this dissertation. The relevance of the demagnetization tensor will be further discussed in section 3.2.1 "Ferromagnetic Resonance".

Since the demagnetizing field $\vec{B}_{\text{shape}}$ is defined for uniformly magnetized solids, it is convenient to discuss the associated energy in more detail. Reformulating eq. 2.25 more generally by integrating over the volume of the solid

$$E_{\text{shape}} = -\int_V \vec{M}(\vec{r}) \cdot \vec{B}(\vec{r}) dV, \tag{2.27}$$

it follows that the energy E_{shape} scales with the volume of the magnetic solid. Since the parallel alignment of the magnetic moments of a macroscopic magnetic solid, i.e. $\text{div}(\vec{M}(\vec{r}))=0$, is associated with an increase of its magnetic energy when increasing the volume, the magnetic solid will eventually form magnetic domains of different orientations in order to reduce this energetic cost. On the other hand, the decrease of E_{shape} resulting from the different orientations of the magnetic moments causes an increase of the exchange energy at the border between two domains. This increase of exchange energy is minimized by a gradual rotation of the orientation of the magnetic moments when passing from one to the other domain also known as a *domain wall*. In nature, two different types of domain walls have been observed, which deviate in the way the gradual rotation of the magnetic moments occurs at the boundary between the two domains. When perpendicularly passing through the plane of the domain wall, in a *Bloch type domain wall*, the rotation of the magnetic moments occurs in the plane parallel to the domain wall. Contrarily, in *Néel type domain walls*, the rotation of the magnetic moments occurs in the plane perpendicular to the plane of the domain wall. Since

E_{shape} scales with the volume of the magnetic solid and competes with the exchange interaction, there exists a critical diameter d_{crit} of magnetic solids given by

$$d_{\text{crit}} = \frac{72\sqrt{AK}}{\mu_0 M_s^2}, \tag{2.28}$$

below which it is not energetically favored to form domain walls [60] and, thus, below d_{crit} the magnetic entity is in a *single domain state*. Here, A is the exchange stiffness [130] and K the magnetocrystalline anisotropy constant. In addition, by further decreasing the volume of the magnetic solid, its magnetocrystalline anisotropy energy also decreases (see eq. 2.23). Since the magnetic anisotropy energies stabilize the orientation of the solid's magnetization against thermal fluctuations, a further decrease of the solids volume may eventually approach a critical size where the thermal energy is comparable with the anisotropy energy. Then, the orientation of the magnetization may flip randomly under the influence of thermal fluctuations even though, the magnetic moments of the ions within the solid are still aligned due to the exchange interaction between them. This property of small magnetic solids occurs in the range of some tens of nanometers and is known as *superparamagnetim* [60], since the small magnetic solid behaves similarly to a paramagnet, but differs in terms of its susceptibility, which is much higher for superparamagnetic particles.

For a more detailed overview of the different magnetic interactions and phenomena, the reader is referred to the literature [10, 30, 55, 56, 57, 58, 60, 100, 101, 102, 104, 117, 118, 121, 123].

3 Methods

In the following, the basic aspects of the fabrication of the samples investigated within the scope of this work is outlined. In addition to the fabrication of the samples, their experimental characterization using FMR experiments in Publication 1 [131] and Publication 3 [132] as well as BLS experiments in Publication 2 [16] is also discussed. The complex nature of magnetic interactions occurring at various length scales can pose challenges in interpreting the thereby deduced experimental findings. The interplay of different magnetic phenomena and their manifestations in the observed spectra require careful analysis and theoretical modeling to gain a comprehensive understanding of the underlying physical processes. To aid in the understanding of these phenomena, theoretical studies have been employed, offering valuable insights and facilitating the interpretation of experimental results. In all three publications a simulation software is used in order to relate the observed properties to the underlying magnetic interactions. This theoretical modeling approach is briefly described in the last section of this chapter.

3.1 Sample Preparation

In principle, the fabrication of mesocrystals composed of NPs facilitates the manipulation of the material characteristics at the mesoscopic scale (i) by altering the shape and size of the NPs, (ii) by varying their arrangement on the mesocrystal lattice, and (iii) by structuring the the mesocrystal into ensembles of a desired geometry. The following two chapters briefly summarize the synthesis of the NPs, their deposition into highly ordered arrangements and their structuring using lithographic techniques.

3.1.1 Nanoparticle Synthesis & Deposition

In order to synthesize MNPs consisting of magnetite (Fe_3O_4), several methods may be utilized such as the thermal decomposition of iron acetylacetonate (Fe(acac)) or iron oleate complexes (Fe(oleate)) which are summarized in Ref. [54]. The MNPs for Publication 1 and Publication 2 have been purchased from Sigma Aldrich, which have been synthesized by thermally decomposing iron oleate complexes. For Publication 3, the MNPs have been synthesized according to Refs. [4, 6, 7] in collaboration with the research group of X. Ye. In the synthesis, the MNP diameter d_{MNP} is controlled by adjusting the reaction temperature [7]. Coating the MNPs with a non-magnetic polymer

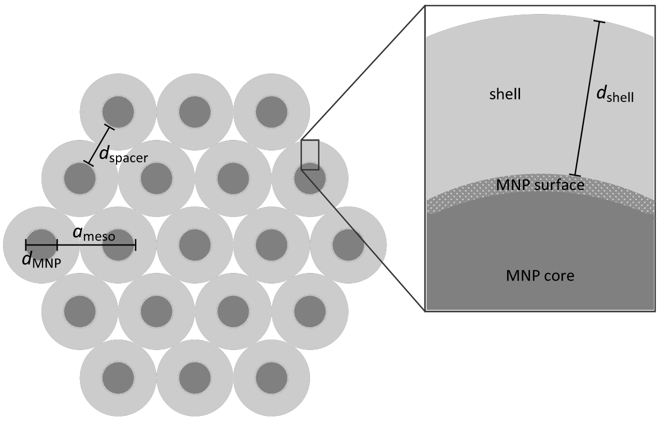

Figure 3.1: Sketch of a hexagonal MNP mesocrystal with the lattice constant a_{meso}. The MNPs with diameters d_{MNP} are coated with a non-magnetic polymer shell with a thickness of d_{shell}. The spacing between the MNPs $d_{\text{spacer}} \approx 2 \cdot d_{\text{shell}}$ can be precisely varied by adjusting the molecular weight of the polymer.

(polystyrene - PS) of specific molecular weight enables the precise manipulation of the spacing between the MNPs d_{spacer} [6], as illustrated in figure 3.1.

The deposition of the MNPs into mesocrystals onto a desired substrate may be achieved by dispersing the MNPs in an appropriate solvent and spin-coating the dispersion onto the substrate [41, 133, 134], as has been done in Publication 3. Highly ordered MNP mesocrystals will only form, when the size distribution of the MNPs is very narrow and, thus, monodisperse. Usually, the standard deviation of the size distribution of the MNPs used in this work is below 5% [41]. During a spin-coating process of the dispersion onto a desired substrate, the MNP form highly ordered mesocrystals by exploiting their evaporation induced self-assembling as depicted in fig. 3.2 (a) [41, 133, 134]. Once the deposition is completed, the particles usually show a high degree of ordering, which can be further increased by subsequently exposing the sample to the vapor of the corresponding solvent in the dispersion. The choice of solvent for dispersing the particles depends on the specific coating of the magnetic nanoparticles (MNPs). For MNPs coated with oleic acid (OA) and PS, toluene has been utilized, as described in Publications 2 and 3. On the other hand, water has been employed as the solvent for MNPs coated with polyethylene glycol (PEG), as demonstrated in Publication 1. By controlling the temperature and flow rate of the vapor during the exposure, a rearrangement of the MNPs is facilitated which may increase the degree of MNP ordering. This method is also known as "solvent vapor annealing" as described in Ref. [7].

Another approach employed in the scope of Publication 2, the so-called *Langmuir-Schaefer method* [16, 34, 37, 38], exploits self-assembling processes of NPs during evaporation of the solvent on top of a liquid subphase as schematically depicted in fig. 3.3. Water or diethylene glycol (DEG) are used as the subphase in case of toluene as solvent of the dispersion. In order to avoid adhesion of the subphase to the inner wall of the trough, the latter is made of polytetrafluoroethylene (PTFE). The use of PTFE as the material for the trough ensures that the subphase remains separate and allows for smoother and more controlled evaporation induced self-assembling of the NPs. It is

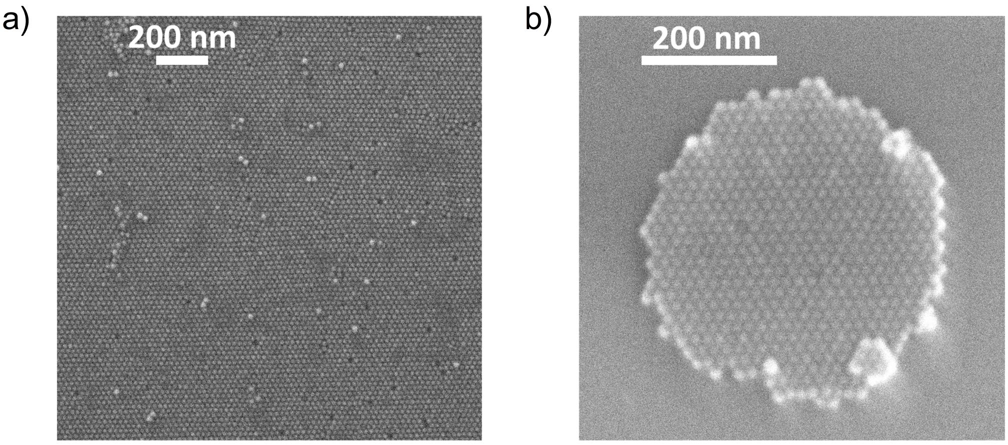

Figure 3.2: Scanning electron microscope images taken from Publication 2 (see section 4.2). a) Image of a highly ordered mesocrystal. b) By adding a small amount of PMMA to the solvent prior to the deposition of the MNPs onto the substrate, a subsequent patterning using EBL is facilitated. Exposing the previously deposited MNP mesocrystal with an electron beam with sufficient energy and duration (and thus dose), the exposed areas will remain on the substrate after a subsequent lift-off process [15]. The images have been taken from Ref. [16]

intuitive that the solvent used has to float on top of the subphase and, thus, it needs to have a lower density than the subphase. After the solvent evaporated entirely, the mesocrystal floats on top of the subphase and may be subsequently be transferred onto a substrate by dipping the substrate gently onto the surface of the subphase. To prevent potential damage to the mesocrystal during the transfer process, a pre-coating of the substrate with a thin layer of PMMA of approximately 50 nm in thickness, or treatment with chlorotrimethylsilane can be employed. The PMMA layer further aids a subsequent structuring using electron beam lithography (EBL) as described in the following chapter.

Both methods described above yield highly ordered MNP mesocrystals, if the quality of the MNP dispersion is high enough, i.e., the particle size distribution is very narrow. Subsequent structuring of the mesocrystals can be achieved by employing EBL, which is described in the following section and schematically depicted in fig. 3.3 in the last step. Furthermore, Publication 1 demonstrates the fabrication of structured, non-ordered assemblies of MNPs by creating openings in a polymethyl methacrylate (PMMA) film, which are subsequently filled using the meniscus force deposition method [3, 131]. This involves placing a droplet of the MNP dispersion onto the pre-structured PMMA film and then contacting it with a glass plate from above, resulting in the formation of a meniscus between the substrate and the glass plate as schematically depicted in fig. 3.4. By gently pulling the glass plate across the substrate surface, the meniscus is pulled across the opening and thereby filling them with MNPs.

3.1.2 Patterning: Electron Beam Lithography

As presented in chapter 1 "Introduction", the great advantage of hierarchical materials such as mesocrystals is that they introduce additional degrees of freedom to tune the

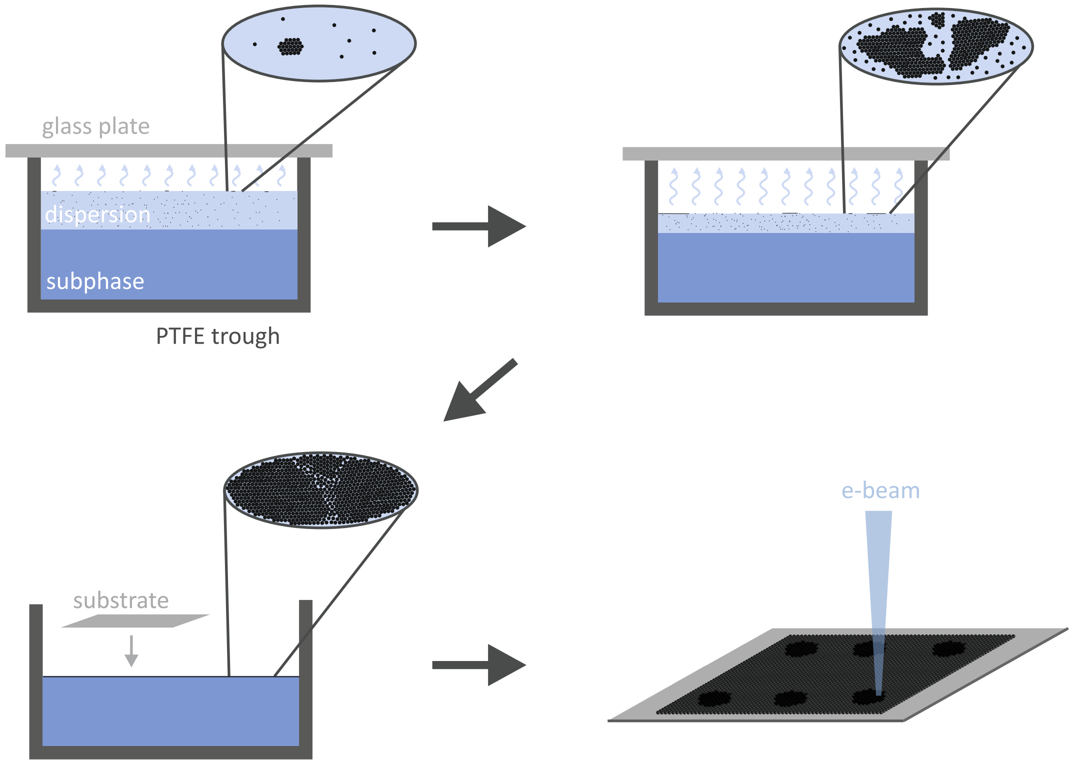

Figure 3.3: Fabricating mesocrystals composed of NPs may be achieved by utilizing the Langmuir-Schaefer deposition method, where self-assembling of the NPs is exploited during the evaporation of the solvent. The evaporation rate of the solvent and, thus, the time for the self-assembling process can be adjusted by covering the trough with a glass plate. After the complete evaporation of the solvent, the mesocrystal floates ontop of the subphase and is transferred onto the substrate by dipping the substrate surface on the surface of the subphase. In a following fabrication step, the mesocrystal can be further structured by employing EBL and a subsequent lift-off process.

characteristics of the material on different length scales. In addition to manipulating material characteristics by tuning the properties of the individual MNPs, the precise control of their collective behavior opens up further possibilities to modify the characteristics of the material. On the one hand, the MNP's spatial arrangement into different mesocrystal lattices may affect the properties of the whole structure [5], while, on the other hand, the shape of the ensemble affects the collective properties on the next higher hierarchical level as schematically depicted in the top of the middle column in fig. 1.1. Structuring the MNP arrangements into ensembles with desired shapes is thus an additional opportunity to precisely control the collective properties of the MNPs in the ordered ensembles, which may be achieved by employing lithographic techniques on a previously deposited mesocrystal. In Publication 2, EBL is employed where the structures are exposed to an electron beam. Using suitable electron doses during the exposure, the solubility of the MNP coating is altered, which facilitates a precise removal of MNPs from specific areas of the substrate in a subsequent lift-off process [15]. PS coated MNPs inherently serve as a negative resist, whereas OA coated MNPs should be deposited onto the substrate

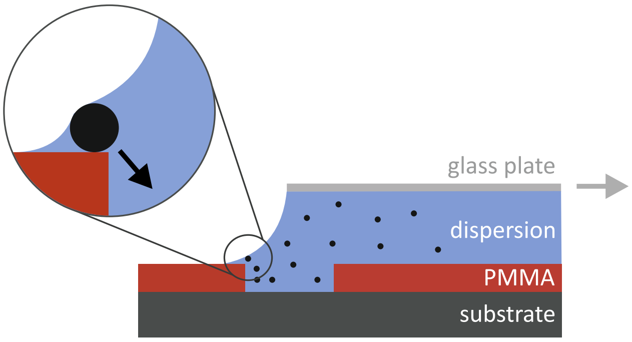

Figure 3.4: Stuctured NP assemblies can be deposited onto a substrate by structuring openings in a previously deposited PMMA film and filling the openings using the meniscus force deposition method. The dispersion forms a meniscus between the substrate and a glass plate, which results in a force acting on the NPs. This can be exploited to fill the openings by dragging the plate across the substrate.

with a small amount of PMMA added to the dispersion to ensure a sufficient change in solubility after the exposure. Proceeding as described above requires an electron dose high enough to alter the solubility of the exposed areas. In order to keep the electron dose during the exposure low enough, a thin film of PMMA may be deposited on the substrate before transferring the floating MNP film onto the substrate. An example of the hereby fabricated structured MNP ensemble is depicted in figure 3.2 (b).

3.2 Characterization Techniques

3.2.1 Ferromagnetic Resonance

Within the framework of (conventional) FMR experiments, the magnetic sample is placed in an external static magnetic field B_{stat} and exposed to a perpendicularly acting oscillating microwave field B_ω of constant frequency $\omega = 2\pi \cdot f$ (here X band frequencies) [59, 79, 135, 136]. A schematic drawing of the experimental set up is depicted inf fig. 3.5. Sweeping the strength of B_{stat} and measuring the intensity of the reflected microwave field enables the investigation of resonant excitations which occur at a specific field strength B_{res}. Usually, these resonant signals are weak and challenging to detect, and correspondingly, good signal amplification is required. Commonly, lock-in amplifier techniques are employed to enhance the sensitivity of the spectroscope. In this context, B_{stat} is superimposed by a small, oscillating/modulating magnetic field B_{mod} with a typical strength of 0.1 G - 2.5 G and frequencies up to 100 kHz. The absorbance of the sample is basically measured at the two field strengths $B_{\text{stat}} + B_{\text{mod}}$ and $B_{\text{stat}} - B_{\text{mod}}$ and subsequently correlated with the strength of B_{mod}. This approach then yields the FMR spectrum, which corresponds to the derivative of the absorption spectrum as illustrated

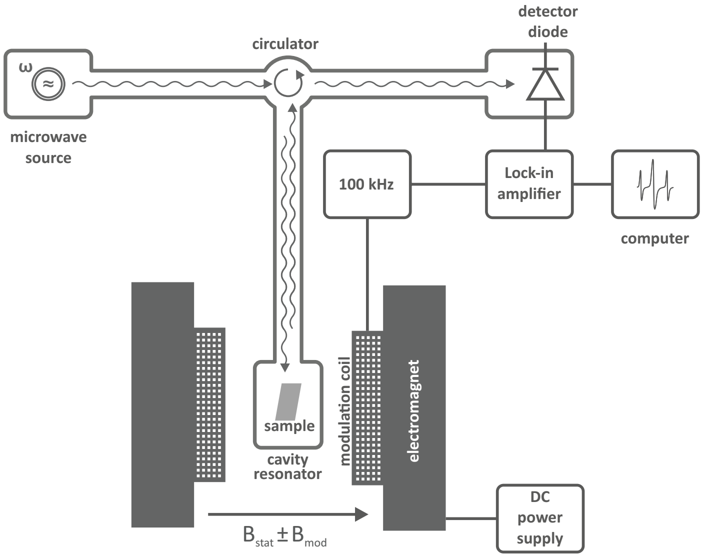

Figure 3.5: In a conventional FMR experiment, the sample is placed in a cavity resonator between the two poles of an electromagnet. The electromagnet creates a static external magnetic field B_{stat}, which is superimposed by a small modulation field B_{mod} created by the modulation coils. During the experiment, the sample is exposed to a microwave field B_{ω} created by the microwave source and the reflected intensity of the microwave field is measured by a detector diode. A FMR spectrum is obtained by measuring the reflected microwave intensity at different static magnetic field strengths B_{stat} using a lock-in amplifier. For a more detailed diagram of the experimental set-up, the reader is referred to Refs. [59, 79]

in fig. 3.6 (a) and (b).

The specific field strength B_{res} at which the resonant absorption occurs depends on the magnetic interactions involved, the geometry of the sample, and the orientation of B_{stat} with respect to the sample. C. Kittel provided the theory of ferromagnetic resonance absorption for different experimental circumstances on the basis of the (undamped) equation of motion of the magnetization M in an external static magnetic field B_{stat} [122]. Throughout this dissertation, the samples investigated are deposited on a flat substrate, and thus their macroscopic geometry can effectively be regarded as a plane or a thin film. Thus, two distinct orientations of B_{stat} with respect to the plane can be identified, where B_{stat} lies within the plane of the sample or is oriented perpendicularly. The two orientations yield different B_{res} since the corresponding resonance conditions deviate from one another due to the altered demagnetization fields. Assuming B_{stat} to be oriented along the z-direction (B_{z}=B_{stat}) and B_{ω} along the x-direction, the resonance condition reads

$$\frac{\omega}{\gamma} = \sqrt{\left[B_{\text{z}} + \mu_0 \left(N_y - N_z\right) \cdot M\right] \cdot \left[B_{\text{z}} + \mu_0 \left(N_x - N_z\right) \cdot M\right]} \tag{3.1}$$

where ω is the angular frequency of the microwave field, γ the gyromagnetic ratio of the sample, μ_0 the magnetic field constant, M the magnetization of the sample, and the N_i the demagnetization factors along the direction $i = x,y,z$ according to table 2.1. This

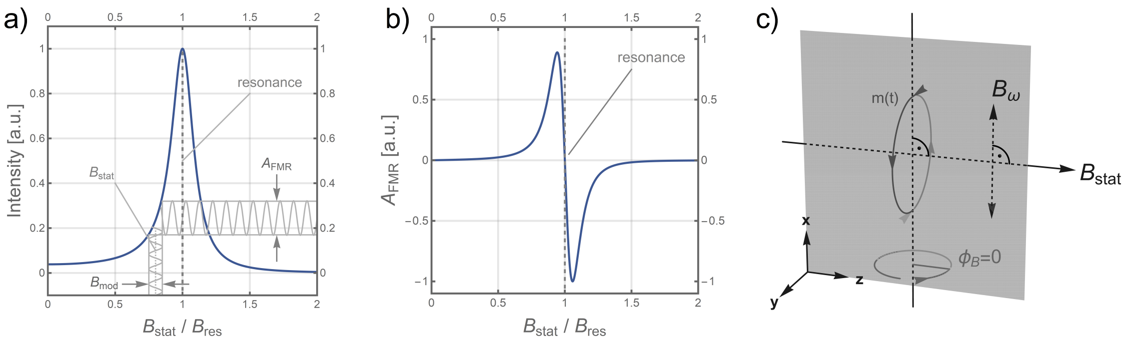

Figure 3.6: Usually, FMR signals are very weak. Lock-In-amplifier techniques are used to obtain sufficiently large FMR amplitudes. Thus, the FMR signals are typically displayed as b) the derivative of a) the absorption spectrum. c) In order to obtain large intensities A_{FMR}, the static external magnetic field and the oscillating microwave field lie within the sample plane.

then yields the resonance condition for B_z being parallel to the film plane ($\phi_B = 0°$, $N_x = N_z = 0$, and $N_y = 1$) as depicted in figure 3.6 (c):

$$\frac{\omega}{\gamma} = \sqrt{\left[B_z + \mu_0 M\right] \cdot B_z}. \tag{3.2}$$

For B_z being perpendicular to the film plane ($\phi_B = 90°$, $N_x = N_y = 0$, and $N_z = 1$), the resonance condition reads

$$\frac{\omega}{\gamma} = B_z - \mu_0 M. \tag{3.3}$$

For paramagnetic samples, B_z simply equals B_{stat}, but for ferromagnetic samples, all interactions and their associated magnetic fields need to be included in B_z, and thus, $B_z = B_{\mathrm{stat}} + B_{\mathrm{dd}} + B_{\mathrm{exc}} + B_{\mathrm{aniso}} +$ etc. For the coherent uniform oscillation mode, also known as the *Kittel mode* [2, 11], the magnetic moments show no tilting against each other, thus $B_{\mathrm{exc}} = 0$ and, therefore, the motion of the magnetic moments is predominantly governed by the dipolar coupling field B_{dd} and the anisotropy field B_{ansio}. The anisotropy field B_{ansio} includes the contributions of the shape anisotropy B_{shape}, the magnetocrystalline anisotropy B_{crys}, and the surface anisotropy B_{surf}. Since the building blocks of the mesocrystals investigated in this work are spherical, the contribution of the shape anisotropy is isotropic (see table 2.1). The contribution of the surface anisotropy does not affect the uniform Kittel mode [9, 92] and, thus, B_{surf} can be neglected for the investigation of the Kittel mode as has been done throughout this dissertation. Here, the only potential contributions of the surface anisotropy to the effective anisotropy field B_{ansio} would result from deviations from the spherical shape, which is negligible for the samples investigated in this work [9, 92]. Thus, the predominant contribution of anisotropy field B_{ansio} is the magnetocrystalline anisotropy [93] and, therefore, B_z reduces to $B_z = B_{\mathrm{stat}} + B_{\mathrm{dd}} + B_{\mathrm{crys}}$.

Taking into account that the conventional FMR set-up employs a cavity resonator, the sample is excited by a uniform microwave field B_ω. Thus, the investigation of spin waves and the quantized counterpart also known as magnons with wave vectors different than the Kittel mode ($k_{\mathrm{M}} \neq 0$) are not accessible by FMR experiments [80, 135]. In addition, as cavity resonators are utilized to expose the sample to a microwave field B_ω, only a single frequency $\omega_{\text{ext}} = \text{const.}$ can be used since the cavity resonators are built for only this specific frequency ω_{ext}. Furthermore, a sample consisting of an array of magnetic entities is always measured as a whole since it is entirely embedded inside the cavity resonator. To overcome these limitations, another experimental approach (Brillouin light scattering) is employed, which is demonstrated in Publication 2.

However, it is worth mentioning, that nowadays modern approaches of FMR experiments exist that enable (i) the investigation of the dynamic properties of magnetic samples at different frequencies, or (ii) individual magnetic nanostructures using "planar microresonators". By utilizing coplanar waveguides for the transmittance of the microwave, the sample may be exposed to a broad range of frequencies instead of a very narrow range as in the case of conventional FMR experiments due to the utilization of customized cavity resonators. While broadband FMR experiments may provide further insight into the dynamic properties of the sample at various frequencies ω_{ext}, an inherent drawback of utilizing coplanar waveguides is that they generally exhibit a lower quality factor, commonly referred to as the *Q-factor,* when compared to cavity resonators. The Q-factor quantifies the efficiency of energy storage in a resonant system relative to the amount of energy dissipated through transmission. Thus, a higher Q-factor indicates higher energy storage in the system. In the case of coplanar waveguides, their design is not optimized for a specific frequency ω_{ext}, which leads to increased energy dissipation. Consequently, the Q-factor of coplanar waveguides is reduced compared to that of cavity resonators [136]. In order to measure the response of the sample at the different frequencies and external static magnetic field strengths a vector network analyzer (VNA) may be utilized in combination with lock-in amplification techniques. A different approach introduced by R. Natkowicz *et al.* employs planar microresonators to replace the cavity resonators in the conventional experiment and enhance the Q-factor such that individual magnetic nanostructures may be measured [63, 64, 68, 69, 70, 71, 72, 73, 74]. Again, a particular experiment will be performed using a single frequency ω_{ext}, but by designing the microresonators appropriately, various frequencies ω_{ext} may be used for different experiments on individual micro- to nanometer sized magnetic entities [72, 73, 74, 137].

3.2.2 Brillouin Light Scattering

BLS experiments involve analyzing the dynamic properties of a magnetic sample by measuring the intensity of photons which have scattered inelastically with a magnetic excitations or spin wave within the sample [17, 67, 78, 75, 80, 138]. As in the case of FMR experiments, the magnetic sample is placed in a static external magnetic field B_{stat} to characterize the material properties at different external conditions. In order to probe its dynamic magnetic properties, a sufficiently high temperature of the sample is required such that magnons, the quantized spin waves, are thermally excited. In addition, to enhance the scattering rate of the impinging photons by magnons, the sample may be exposed to an oscillating magnetic field B_ω which acts perpendicular to B_{stat}. In order to expose the sample to an oscillating magnetic field, it may be placed on top of a coplanar waveguide, which is employed to transmit the microwave field. The physical process used to detect magnetic excitations is schematically depicted in figure 3.7

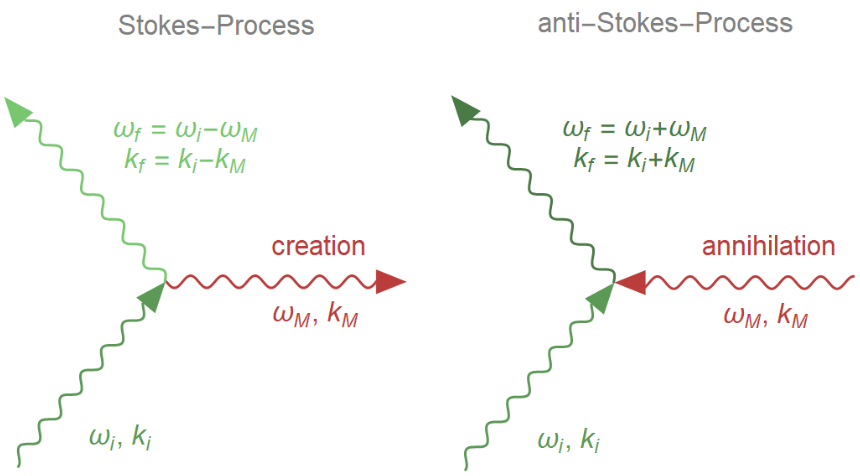

Figure 3.7: Exposing the magnetic solid to photons of a specific energy $\hbar\omega_\mathrm{i}$ and momentum $\hbar k_\mathrm{i}$, the photon may scatter inelastically either creating (Stokes-process) or annihilating (anti-Stokes-process) a magnon with an energy $\hbar\omega_\mathrm{M}$ and momentum $\hbar k_\mathrm{i}$ yielding a shift of the wave vector k_f and of the frequency ω_f of the scattered photon [67].

[67]. Monochromatic, linearly polarized light impinges on the sample. The impinging photons may then be scattered either elastically (Rayleigh-scattering) or inelastically by creating (Stokes-process) or annihilating a magnon (anti-Stokes-process) of a specific angular frequency ω_M. The information about the dynamic magnetic properties of the sample are thus associated with the inelastic scattering process which yields an energy gain (annihilation - anti-Stokes-process) or loss (creation - Stokes-process) of the scattered photon by $\Delta E = \pm\hbar\omega_\mathrm{M}$, respectively. This gain/loss corresponds to a frequency shift of the inelastically scattered photon of $\omega_\mathrm{f} = \omega_\mathrm{i} \pm \omega_\mathrm{M}$, where ω_i is the angular frequency of the impinging photons and ω_f the angular frequency of the inelastically scattered photons. This frequency shift can be analyzed by employing a sufficiently sensitive interferometer [67], such as a "tandem-(3+3)-Fabry-Pérot interferometer" (TFPI).

A schematic view of the BLS set-up is depicted in fig. 3.8. In order to analyze the dynamic properties of a magnetic sample using BLS spectroscopy, the incident laser beam is initially broadened by a telescope to fully illuminate the objective as shown in fig. 3.8 a). At beam splitter 1 (BS1) a reference beam is created which is used to stabilize the TFPI. The transmitted laser beam passes through BS2 and is subsequently reflected onto the sample by the polarizing beam splitter (PBS). The $\lambda/2$-plate is used to rotate the polarization plane of the incident photons such that they are completely reflected onto the sample by the PBS. The PBS is a crucial element of the experimental set-up, since this component splits the reflected laser beam into the inelastically and elastically scattered photons, as the inelastic scattering process rotates the polarization plane of the photons by 90° [79]. Hence, the inelastically scattered photons pass through the PBS after the reflection from the sample, while the elastically scattered photons, which do not experience a polarization change, are directed to the camera by BS2 for imaging the sample. It should be noted, that the extinction ratio between the two perpendicular polarization directions of the PBS has to be very high ($>10^5$) since the scattering crosssec-

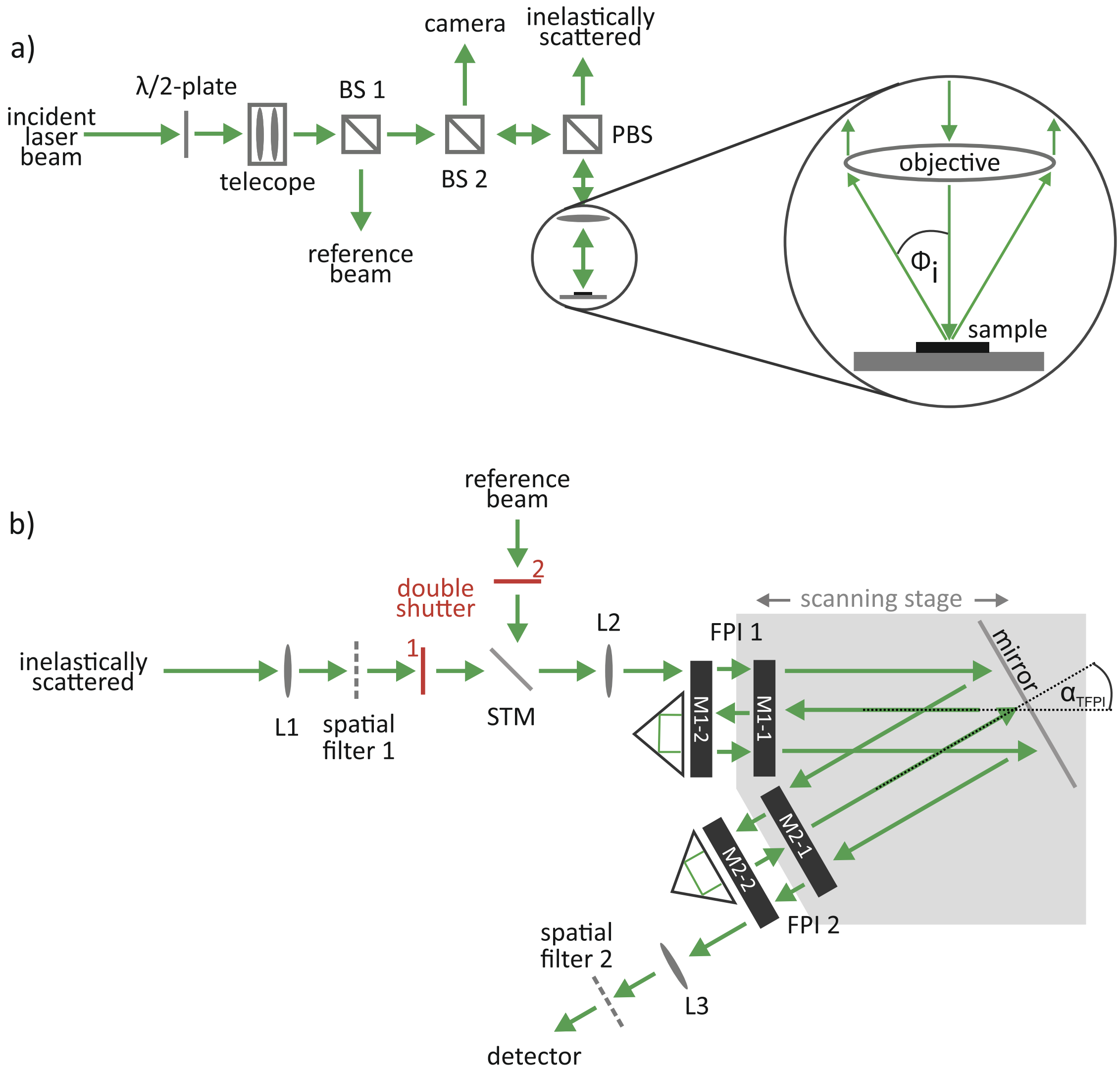

Figure 3.8: Schematic drawing of the beam line in a BLS experiment. a) The incident laser beam is directed into a telescope to widen the beam diameter such that the full aperture of the objective is illuminated. The first beam splitter (BS1) is utilized to create a reference beam used for the interferometer, while the second beam splitter (BS2) directs the elastically scattered light to a camera in order to visualize the sample. The polarizing beam splitter (PBS) divides the scattered photons into inelastically and elastically scattered photons. Since the inelastic scattering process of photons with magnons is associated with a rotation of the polarization by 90°, these photons pass through the PBS, while elastically scattered photons are directed to the camera. The $\lambda/2$-plate is used to ensure a maximum reflection at the PBS of the incident laser beam onto the sample. b) After the inelastic scattering process, the photons are directed into the tandem-(3+3)-Fabry-Pérot interferometer. The spatial filters may be used to analyze photons with a specific scattering angle ϕ_i. The spectral analysis of the photons is achieved by varying the distance of the individual FPIs by moving the scanning stage. Since the employment of a single FPI does not facilitate the explicit assignment of the scattering process related to different transmission orders, two FPIs are employed which are tilted by an angle α_TFPI in order to suppress signals of the different transmission orders [78, 80].

tions of photons by magnons are very small [80, 77]. A larger extinction ratio thus aids a better signal-to-noise ratio of the spectrometer. The inelastically scattered photons are subsequently directed to the TFPI as shown in fig. 3.8 b). The spatial filters are used to analyze photons that have been scattered by an angle ϕ_i only as shown in fig. 3.8 a). The double shutter ahead of the semitransparent mirror (STM) is used to either direct the reference beam through the TFPI in order to stabilize the interferometer, or the inelastically scattered photons to probe the sample. A detailed description of the operating principle of the TFPI is provided in Refs. [78, 79, 80]. In brief, one mirror of each of the two individual Fabry-Pérot interferometer (FPIs) is mounted to a scanning stage, denoted as M1-1 and M2-1, respectively, while M1-2 and M2-2 are fixed and can not be moved. The optical axes of the two FPIs are tilted by an angle α_{TFPI} such that by moving the scanning stage by a distance Δd, the distances between the the mirrors of the two FPIs are altered by Δd for FPI1 and $\Delta d \cdot \cos\alpha_{\text{TFPI}}$ for FPI2. The consequence of the coupling of the two FPIs is that transmissions of higher orders through the individual FPIs will be suppressed, which allows for a specific assignment of the magnonic signals. After passing through the TFPI, the intensity of the scattered photons is then measured by a detector for a given position of the scanning stage. The positions of the scanning stage determines the distance between the mirrors of the mirrors of the two FPIs. Since the distances between the FPIs determine the wavelength and, thus, the frequency of the photons that can pass through, a BLS spectrum is obtained by sweeping Δd and measuring the intensity of the detected photons. The observed spectral features can then be correlated with the dynamic magnetic properties of the sample by the energy shift of the scattered photon $\hbar\omega_f$ which is related to the energy of the magnon $\hbar\omega_M$ and the impinging photons $\hbar\omega_i$ by

$$\hbar\omega_f = \hbar\omega_i \pm \hbar\omega_M. \tag{3.4}$$

For infinite solids, where magnons may be described as plane waves, the conservation of momentum is also fulfilled and thus,

$$\hbar\vec{k}_f = \hbar\vec{k}_i \pm \hbar\vec{k}_M, \tag{3.5}$$

where $\vec{k}_f$, $\vec{k}_i$, and $\vec{k}_M$ are the wave vectors of the scattered and impinging photon, and of the magnon, respectively. The great advantage of BLS experiments is that this technique may enable the investigation of magnons with $\vec{k}_M \neq 0$, by varying the angle of the beam of impinging photons with respect to the sample normal. In accordance with *Noether's theorem*, the conservation of momentum given in eq. 3.5 is applicable to the in-plane components of the wave-vectors solely due to the break of translational symmetry at the surface of the sample [67]. Thus, by varying the angle of incidence ϕ_i of the impinging photons, the in-plane component of the wave vector of the impinging photons $\vec{k}_i$ may be altered. Since the energy of the annihilated/created magnon depends on its wave vector which is correlated with the frequency ω_M by the material's dispersion relation, the measurement of the energy gain/loss $\Delta E = \pm\hbar\omega_M$ of the inelastically scattered photons for different angles of incidences ϕ_i enables the measurement of this dispersion relation [17, 67, 75]. The wave vector of the magnon is related to ϕ_i by:

$$k_M = 2 \cdot \frac{2\pi}{\lambda_{\text{phot}}} \cdot \sin\phi_i, \tag{3.6}$$

where λ_{phot} is the wavelength of the impinging photons. It can easily be concluded that there exists a maximum wave vector (i.e., a minimum wavelength) of the magnon that is experimentally accessible. For an infinite solid body, the maximum wave vector of a magnon $k_{\text{M,max}}$ that can be probed is restricted by the maximum transfer of momentum. This is the case when the photons are scattered by an angle $\phi_{\text{i}} = 90^\circ$ yielding a maximum wave vector of $k_{\text{M,max}} = 23.6$ rad/μm (minimum wave length of 266 nm) when using a 532 nm laser [67, 80]. Strictly speaking, equations 3.4, 3.5, and 3.6 derived from Noether's theorem are valid only for magnons within infinite magnetic solids. For finite samples, these equations may not hold true and break down [138]. Consequently, magnons within finite structures do no longer possess a sharp wave vector but are composed of a distribution of wave vectors resulting from the *Fourier transform* of the spatial spin wave profile [77, 80, 138]. As a result, there exists an overlap of the Fourier transform of the spin wave profile with the range of $\left[0{,}2k_{\text{i}}\right]$ for the inelastically scattered photons, enabling the detection of spin waves of much smaller wavelength than, e.g., 266 nm resulting from equation 3.6 [76, 77]. An additional advantage of this technique is that it is not restricted to a single specific frequency of the driving microwave field B_ω, as it is the case for (conventional) FMR experiments. Using coplanar waveguides, the sample can be driven with various excitation frequencies allowing for the characterization in a much broader frequency range. An overview of experimental investigations of magnon dispersion relations in 1D and 2D magnonic crystals may be found in references [24, 33, 78, 81, 83], while 3D magnonic crystals have not been investigated experimentally yet.

3.3 Theoretical Modeling

The utilization of numerical simulations on suitable model systems provides a valuable tool for interpreting the magnetic phenomena observed experimentally. By simulating the system, it becomes possible to link the observed spectral features to the specific material characteristics associated with them. Such simulations are especially powerful to obtain further insight into the static and dynamic properties of the magnetic structures. The numerical modeling approaches used are based on the *Heisenberg model*, where the magnetic moments are assumed to be well-localized at the ions at the corresponding atomic sites on the crystal lattice [98]. Thus, this approach is very powerful for most magnetic materials with low electrical conductivity but it fails for band ferromagnets with highly mobile electrons such as for iron, cobalt, and nickel [100, 101, 102]. For highly conductive magnetic materials, a different approach derived within the framework of the *Hubbard model* has to be considered, which will not be discussed here [102].

The total magnetic moment of an ion is related to its partially filled electronic orbitals. Thus, it is convenient to first consider an isolated ion possessing a total angular momentum vector $\vec{J}$ with the corresponding expectation value

$$\left\langle \hbar \vec{J} \right\rangle = \hbar \sqrt{J\left(J+1\right)}, \tag{3.7}$$

where J is the total angular momentum quantum number. The projection of $\vec{J}$ on to the quantization axis (z-axes in the following) yields $\langle \hbar J_z \rangle = \hbar m_j$, where m_j is the secondary magnetic quantum number. This then gives the magnetic moment m_z of the ion with $m_z = -g\mu_\mathrm{B} m_j = \gamma\hbar m_j$, where γ is the gyromagnetic ratio, μ_B the Bohr magneton, and g the Landé (or g-factor) of the ion. The potential energy of the magnetic moment $\vec{m}$ in an external static magnetic field along the z-direction $\vec{B}_\mathrm{stat} = (0{,}0{,}B_\mathrm{stat})$ can then be represented by the *Zeeman energy*

$$\mathcal{H}_\mathrm{Zee} = -m_z B_\mathrm{stat} = -\gamma\hbar m_j B_\mathrm{stat}, \tag{3.8}$$

which yields the equation of motion of the expectation value of $\vec{m}$ [59, 79] given by:

$$\frac{\mathrm{d}\langle \vec{m} \rangle}{\mathrm{d}t} = \frac{i}{\hbar}\Big\langle \big\{ \mathcal{H}_\mathrm{Zee}, \vec{m} \big\} \Big\rangle = -\frac{i}{\hbar}\gamma B_\mathrm{stat} \left\langle \left\{ \hbar m_j, \hbar \vec{J} \right\} \right\rangle = -\gamma \langle \vec{m} \rangle \times \vec{B}_\mathrm{stat}, \tag{3.9}$$

where $\{a{,}b\} = ab$ - ba is the commutator of the quantum mechanical operators a and b. The above equation is the macroscopic equation of motion of the magnetic moment in an external magnetic field, which describes a precession of the magnetic moment $\vec{m}$ around the direction of the external magnetic field $\vec{B}_\mathrm{stat}$.

The localized magnetic moments of the ions within the solid, which arise from partially filled electron orbitals of the ions, can be considered as a thermodynamic subsystem. This subsystem is thermally coupled to other subsystems of the solid, including the crystal lattice and the conduction electrons, forming a complex interplay of thermal interactions within the material [99]. The thermodynamic coupling of the different subsystems results in energy dissipating from the magnetic system into the other reservoirs resulting in a damping of the precession of $\vec{m}$ around the direction of $\vec{B}_\mathrm{stat}$. Several mechanisms are related with the damping process, for which two illustrative examples will be discussed [79, 99]. For example, by considering the dipolar interactions between the localized magnetic moments at their respective lattice sites, one can gain a conceptual understanding of the coupling between the magnetic and lattice systems. As the dipolar coupling depends on the distance between the ions, lattice vibrations affect the corresponding distances and thus give rise to the coupling of the two subsystems [118]. Moreover, the coupling between the two subsystems can further be understood in terms of the spin-orbit coupling, which directly links the orientation of the ion's magnetic moment to the crystal lattice. The two mechanism illustrate the interplay between the magnetic properties and the structural characteristics of the material, resulting in a damping of the precessional motion of $\vec{m}$ around the direction of $\vec{B}_\mathrm{stat}$. To account for the dissipation of energy from the precessional motion and, thus, the damping, the equation of motion must be expanded by an effective phenomenological damping parameter that comprises all potential damping processes. This yields the *Landau-Lifshitz-Gilbert equation*, where the damping is proportional to its angular velocity $\mathrm{d}\vec{m}/\mathrm{d}t$ yielding

$$\frac{\mathrm{d}\vec{m}}{\mathrm{d}t} = \frac{\gamma}{1+\alpha^2}\left(\vec{m} \times \vec{B}_\mathrm{stat} + \alpha \cdot \vec{m} \times \frac{\mathrm{d}\vec{m}}{\mathrm{d}t} \right), \tag{3.10}$$

where α is the phenomenological damping factor. The damped precessional motion of $\vec{m}$ is illustrated schematically in figure 3.9. The figure also depicts the torque terms

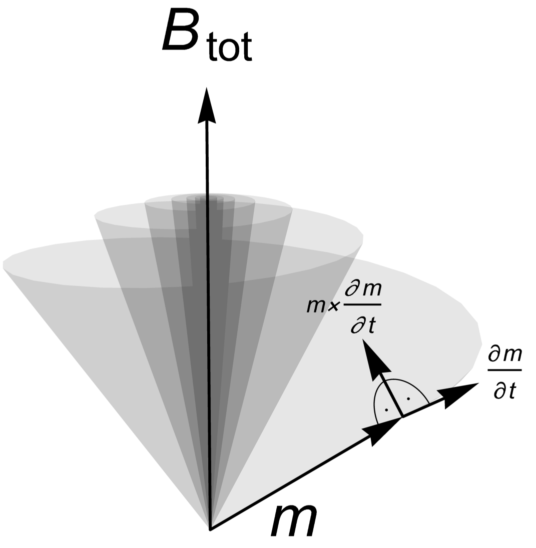

Figure 3.9: According to the Landau-Lifshitz-Gilbert equation (eq. 3.8) a magnetic moment performs a precessional motion around the direction of a (total) magnetic field $\overrightarrow{B}_{\text{tot}}$ due to the torque $\partial\overrightarrow{m}/\partial t = -\gamma \cdot \overrightarrow{m} \times \overrightarrow{B}_{\text{tot}}$. Since the spin system is thermally coupled to other thermal reservoirs, energy dissipates out of the spin system resulting in a damping of this motion described by $\overrightarrow{m} \times \partial\overrightarrow{m}/\partial t$.

responsible for the precession and damping of the magnetic moment. Without any external energy input, the orientation of $\overrightarrow{m}$ gradually aligns with the direction of $\overrightarrow{B}_{\text{stat}}$.

As has been discussed in section 3.2.1 "Ferromagnetic Resonance", the total magnetic field $\overrightarrow{B}_{\text{tot}}$, which acts on the magnetic moments of the ions in a magnetic solid, comprises all relevant magnetic interactions. Thus $\overrightarrow{B}_{\text{stat}}$ in equation 3.10 has to be replaced by the total magnetic field $\overrightarrow{B}_{\text{tot}}$ given by

$$\overrightarrow{B}_{\text{tot}} = \overrightarrow{B}_{\text{stat}} + \overrightarrow{B}_{\text{exc}} + \overrightarrow{B}_{\text{dip}} + \overrightarrow{B}_{\text{aniso}} + ... \tag{3.11}$$

The corresponding magnetic fields related to the different interactions may be obtained by [98]

$$\overrightarrow{B}_i = -\mu_0 \frac{\partial E_i}{\partial \overrightarrow{m}_i}, \tag{3.12}$$

where E_i is the energy associated with the corresponding magnetic interaction. Considering the aforementioned factors, magnetic materials can be modeled using two distinct frameworks, depending on the length scales under investigation. For simulations at very small length scales, atomistic simulations are employed, which simulate the magnetic moments of the ions individually [98]. On the other hand, for simulations which focus on larger length scales, micromagnetic simulations are utilized, employing a continuum approximation to capture the material characteristics [118, 139]. In the simulation of magnetic materials, despite of the chosen framework, the material is represented as a collection of interacting subunits. These subunits can be individual ions, or small magnetic volumes, depending on the scale of the simulation. The interactions between the subunits are typically modeled using appropriate mathematical expressions following eq.

3.12. In addition to the interactions between the subunits, external oscillating fields may also be incorporated into the simulation. These fields can mimic the effect of experimental techniques, such as applying a magnetic field or performing spectroscopic measurements, allowing for the investigation of the dynamic properties of the magnetic sample. By studying the response of the system to these external fields, valuable insight into the behavior of the material can be obtained, aiding in the interpretation and understanding of experimental observations. In order to obtain insight into the dynamic properties of the idealized model system, the time evolution of the whole structure has to be calculated. In general, such a complex calculation cannot be performed analytically, and thus numerical approaches are employed to overcome this difficulty. Here, the widely utilized open-source software such as OOMMF employs a fourth-order explicit (predictor-corrector) Runge-Kutta solver [94]. In general, implicit methods may also be useful to numerically calculate the time evolution of the subunits. In this work, the Fortran90 ODE-solver has been employed for integrating the equation of motion which is based on the backward differentiation formula (BDF) methods [140]. The great advantage of this BDF method is its applicability to "stiff" initial value problems (IVP). In this context, the "stiffness" of the IVP has to be understood on the basis of the *Lipschitz continuity*, which restricts the upper boundary of the chosen time step for the integration to avoid instabilities and oscillations when integrating the equation of motion [141]. After calculating the time evolution of all subunits for different external field strengths, e.g., in the context of modeling FMR spectra, it becomes important to analyze and relate the calculated spectral features to specific characteristics of the sample structure. To achieve this, *Fourier transforms* are performed on each subunit, allowing for the identification of resonant regions within the magnetic structure at the specific external conditions.

4

Summary of Results

Throughout this dissertation, the characteristics of magnetic nanoparticles associated with dipolar coupling phenomena on the mesoscopic scale (see fig. 1.1 referring to Ref. [3]) have been investigated. To provide a comprehensive understanding of the scientific path followed in this work, an overview of the three articles published over the course of this work is provided. In brief, the successive publications comprise studies in which the impact of dipolar coupling phenomena at different hierarchical levels on the collective magnetic behavior has been systematically investigated. Starting with the characterization of the interactions between disordered nanoparticle assemblies, followed by the investigation of the properties of the individual ordered ensembles and, finally, the analysis of the characteristics of the individual MNPs which constitute the arrangement were addressed in more detail.

4.1 Publication 1: Investigation of the dipole interaction in and between ordered arrangements of magnetic nanoparticles

Isolated monolithic magnetic nanostructures may possess several resonant excitations [22, 44, 69] when studied by FMR and BLS experiments. These excitations can subsequently be assigned to different resonant areas within the nanostructures using theoretical modeling [26, 81]. Decreasing the distance between the individual nanometer sized magnetic entities enhances the dipolar coupling between them resulting in distinct spectral dependences. However, hierarchical magnetic nanostructures composed of MNPs have not yet been investigated in detail experimentally and, thus, the dynamic coupling effects associated with the dipolar interaction within hierarchical structures remain to be investigated.

In Publication 1, the investigation of dipolar coupling effects between circularly patterned MNP assemblies has been addressed. The diameters of the MNP assemblies fabricated range between 720 nm to 300 nm and the spacing between the assemblies ranges from 700 nm to 50 nm. The constituent MNPs posses diameters of 20 nm and are coated with polyethylene glycol resulting in a spacing between the MNPs of approximately 2 nm. The characterization of the MNP assemblies has been performed using angle dependent FMR experiments. It has been shown that two resonant excitations may occur, one main resonance attributed to the central area of the circular assembly and one satellite resonance assigned to resonant excitations near the edges of the assembly. By decreasing the spacing between the assemblies, the dipolar coupling between MNPs of neighboring assemblies is more pronounced near the edges, and thus the resonance field of the satellite resonance exhibits an angle dependence at sufficiently short spacings.

The Publication highlights the dipolar coupling between MNPs within an individual MNP assembly and between MNPs of neighboring assemblies. It is shown that the collective properties of MNPs with diameters of 20 nm arranged into assemblies of some hundreds of nanometers show characteristics comparable to those of monolithic magnetic structures. However, their spectral properties differ.

The samples for this publication have been fabricated and measured by N. Neugebauer. The simulation software has been developed by M. Czerner and N. Neugebauer and the corresponding simulations for this publication have been performed by N. Neugebauer. This article is the result of a fruitful scientific discourse between the authors, in which, in addition to Nils Neugebauer, especially the contribution of Prof. Peter J. Klar, Prof. Christian Heiliger, Prof. Detlev M. Hofmann and Dr. Matthias T. Elm should be emphasized. Their contribution was primarily to contribute to the interpretation and understanding of the results and to provide impetus for the necessary experimental and theoretical work.

PHYSICAL REVIEW B **101**, 104409 (2020)

Investigation of the dipole interaction in and between ordered arrangements of magnetic nanoparticles

Nils Neugebauer,[1,*] Alexander Fabian,[2,3] Matthias T. Elm,[1,3,4] Detlev M. Hofmann,[1,3] Michael Czerner,[2,3] Christian Heiliger,[2,3] and Peter J. Klar[1,3]
[1]*Institute of Experimental Physics I, Justus Liebig University Giessen, Heinrich-Buff-Ring 16, 35392 Giessen, Germany*
[2]*Institute for Theoretical Physics, Justus Liebig University Giessen, Heinrich-Buff-Ring 16, 35392 Giessen, Germany*
[3]*Center for Materials Research (LaMa), Justus Liebig University Giessen, Heinrich-Buff-Ring 16, 35392 Giessen, Germany*
[4]*Institute of Physical Chemistry, Justus Liebig University Giessen, Heinrich-Buff-Ring 17, 35392 Giessen, Germany*

(Received 26 November 2019; revised manuscript received 3 February 2020; accepted 18 February 2020; published 9 March 2020)

Magnetite nanoparticles (particle diameter $d_{\mathrm{NP}} = 20$ nm) were arranged into chains of cylinderlike entities of fixed radius R with constant spacings D between neighboring entities. For this purpose, chains of circular openings were defined in a 250-nm-thick electron-sensitive resist on a Si substrate by electron beam lithography. These patterns were subsequently filled with the magnetite nanoparticles using a variant of the meniscus force deposition method. To study the dipolar magnetic interaction between the spherical magnetite particles within the cylinders as well as that between cylinders, three series of chain arrangements were prepared, each with another constant average cylinder radius ($R = 360$, 240, and 160 nm). The three samples of each series differ in terms of their D values, which vary between 700 nm (no intercylinder coupling) and 50 nm (magnetic coupling between cylinders). Angle-dependent ferromagnetic resonance (FMR) measurements revealed that for large R and D only one broad resonance appears, while for $R = 240$ and 160 nm two resonances are present. At short D, an angular dependence of the resonances induced by the coupling between the cylinders is clearly visible. Furthermore, the amplitude of the main resonance decreases, and side bands occur when the cylinders of the chain are hollow, i.e., when some nanoparticles are removed from the center of each cylinderlike entity. The dynamics of the coupled magnetic dipoles of the magnetite particles and its impact on the FMR spectra of the samples, i.e., associating the different resonances to characteristic collective oscillations of the magnetic moments within the ordered arrangement of magnetite nanoparticles, can be understood using micromagnetic simulations based on a numerical solution of the Landau-Lifschitz-Gilbert equation.

DOI: 10.1103/PhysRevB.101.104409

I. INTRODUCTION

Nanosized magnetic structures still attract a great deal of interest because their magnetic properties are not only determined by their chemical constituents, but also by their shape and their spatial arrangement into different patterns [1–3]. Such magnetic nanostructure arrangements provide a vast playground for tuning magnetic properties according to the needs of specific applications [4,5]. While interactions on the atomic scale, e.g., exchange interaction or magnetocrystalline anisotropy, determine the formation of magnetic domains of smaller entities, long-range coupling phenomena such as dipole-dipole interactions affect the properties of the entire magnetic nanostructure arrangement, leading, e.g., to the so-called shape anisotropy [3,6–9]. Commonly, top-down approaches are used to fabricate ordered arrangements of magnetic nanostructures. An example of a top-down approach is the combination of lithographic techniques and thin-film deposition. The latter may be performed by vacuum deposition methods such as physical vapor deposition, sputter deposition, or others [7,10–13]. Depending on the distance between the single nanomagnets, the collective behavior of such patterned magnetic thin films is governed by short-range exchange coupling [10,14,15] or long-range dipolar coupling [5,11,16,17] between the magnetic compounds.

An alternative approach for fabricating magnetic structures comprises the use of lithographic techniques for defining openings in a resist layer on a substrate, which are subsequently filled with magnetic nanoparticles (MNPs) employing bottom-up techniques such as Langmuir-Blodgett film formation, dip-coating, spin-coating, etc. The successful self-assembly of MNP films has been widely demonstrated for ordered [18–21], as well as for randomly packed nanoparticles [22–24]. The advantage of such MNP-based entities compared to conventionally fabricated magnetic nanostructures is that their magnetic properties are much more susceptible to interstructure dipolar interactions, since the nanoparticles constructing the entity cannot couple via predominant exchange interaction. This offers an additional degree of freedom to tune the properties of the magnetic structures. Although size- and shape-dependent magnetic properties of MNPs have already been investigated for randomly oriented [25–28] as well as regularly ordered [22–24] clusters of MNPs, systematic

---

[*] Nils.Neugebauer@physik.uni-giessen.de

studies of the properties of patterned regular arrangements of MNP entities and especially the dipolar coupling between the entities are still lacking.

In this work we study the dipolar magnetic coupling between cylindrical entities of MNPs by ferromagnetic resonance spectroscopy (FMR) as a function of cylinder size, degree of filling, and spacing between these cylindrical entities. FMR is established as a powerful tool for investigating the dynamic properties of the magnetization of single magnetic nanostructures as well as coupling phenomena in magnetic arrangements [10,11,15,29–31]. The MNP sample is placed in an external magnetic field H_{ext}. While the magnetic field is swept, the sample is continuously exposed to a microwave radiation field H_{mw} (with a constant frequency $f = \omega/2\pi$). It excites a collective oscillation within the MNP arrangement each time when the external magnetic field fulfills the corresponding resonance condition:

$$\begin{aligned}\frac{\omega}{\gamma} &= H_{\text{eff}}\\ &= H_{\text{ext}}^{\text{res}} + H_{\text{int}},\end{aligned} \tag{1}$$

where H_{eff} denotes the effective local magnetic field, $\gamma = ge/2m$ is the gyromagnetic ratio, g the Landé factor, e is the elementary charge, and m is the mass of the electron. $H_{\text{ext}}^{\text{res}}$ denotes the external magnetic field strength, at which the resonance condition is fulfilled, and H_{int} is the internal magnetic field a magnetic moment experiences due to its surrounding. A classical description of the collective behavior is obtained by assigning a magnetic moment $\vec{m}_i(\vec{r}, t)$ to each MNP and by allowing for a long-range dipole-dipole interaction with the neighboring shells of MNPs [32–35]. The time evolution of the macroscopic magnetization $\vec{M}(\vec{r}, t)$ is then given by a superposition of all $\vec{m}_i(\vec{r}, t)$ described by the Landau-Lifshitz-Gilbert (LLG) equation. The numerical solution of this equation allows us to relate the measured FMR resonance signals to characteristic excitations of the $\vec{m}_i(\vec{r}, t)$ and thus to spatial locations within the MNP entities studied.

II. METHODS

A. Sample preparation

Electron beam lithography (EBL) was used to prepare openings in a 250-nm-thick resist layer consisting of polymethyl methacrylate (PMMA) spin-coated onto a (100) silicon substrate. Using low doses during EBL exposure (<3000 μC/cm^2), the PMMA serves as a positive resist when developed for 45 s in a solution of water and isopropanol (1:2 in volume). In a subsequent preparation step, the resulting openings are filled with MNPs using a variant of the horizontal dip-coating process employing a MNP suspension [32]. Since bare particles are not dispersible due to attractive forces between them, surface functionalization of the MNP is required to prevent agglomeration. Depending on the polarity of the surfactant, particles can be dispersed in nonpolar or polar solvents. We chose an aqueous suspension of polyethylene glycol-coated spherical Fe_3O_4 nanoparticles (particle concentration $\sim 4.5 \times 10^{13}$ particles/mL) showing an average diameter of $d_{\text{NP}} = 20$ nm (Sigma-Aldrich product number: 725366). When the dispersion is pipetted onto the patterned substrate and covered with a glass plate, a meniscus forms at the surface of the suspension between the edge of the glass plate and the substrate. In moving the glass plate across the substrate, the meniscus, as it is dragged across the substrate, pushes the MNPs into the openings of the resist layer and deposits them there, but not on the surface of the resist layer. The deposition process may be repeated several times until the openings are entirely filled with MNPs. After evaporation of the suspension's solvent, the magnetic nanostructure arrangement is obtained. The MNP arrangements were designed to study magnetic coupling phenomena within closely packed MNP entities of defined shape and size as well as coupling between such entities as a function of spacing. We chose to arrange the MNPs to cylindrical entities with a radius defined by the radius of the resist openings and an average height of $h \approx 80$ nm. Employing the meniscus force deposition method leads to a compact filling of the openings with MNPs. The height of the nanoparticle entities show slight deviations, as more MNPs accumulate near the edges of the circular openings compared to the center of each opening. For further information and a detailed description of the horizontal dip-coating process, see Refs. [32,36]. The cylindrical entities were arranged into linear chains with a periodic spacing D along the chain direction, denoted as x-direction in the following. To enhance the FMR signal strength, a parallel arrangement of chains with a spacing of at least 3 μm along the y-direction, perpendicular to the chain direction, was fabricated. Thus, the magnetic nanostructure arrangements of each sample consist of cylinders with fixed radius R and height h of closely packed MNPs arranged on a rectangular grid where the spacing D along x is in a range where coupling between the cylindrical entities may occur whereas the spacing along y is too large to yield a detectable magnetic coupling. A circular shape of the entities was chosen, as it should yield an isotropic behavior of the FMR signal for isolated entities, when the orientation to an external field is varied in-plane of the sample, since the demagnetization fields of the cylinder are uniform in this plane. Thus, any major deviation from an isotropic behavior should have its origin in coupling phenomena between the cylindrical entities. The spacing D in the x-direction was constant for each sample, but varied throughout each set of samples covering the range from 700 to 50 nm, a range where the onset of detectable coupling between neighboring cylindrical entities should occur. Three series of rectangular arrangements of cylindrical MNP entities were examined: Set 1 consists of cylinders with radii of $R = (340 \pm 16)$ nm, Set 2 of cylinders with $R = (240 \pm 8)$ nm, and Set 3 of cylinders with $R = (160 \pm 10)$ nm. Decreasing the radii of the cylindrical MNP entities leads to a larger contribution of MNPs near the edge of the entity to the overall magnetic response. The ratio of the number of these particles near the edge to that of the particles in the central region is determined by the radius of the cylindrical arrangement R. We refer to this ratio as the edge-to-volume ratio in what follows. It is proportional to $1/R$ and thus increases from Set 1 to Set 3. Furthermore, we have placed samples of Set 3 in an ultrasonic bath with acetone for 20 s at 20 °C, which allowed us to remove MNPs from the center of their cylindrical entities, resulting in ringlike or hollow-cylinderlike entities with an

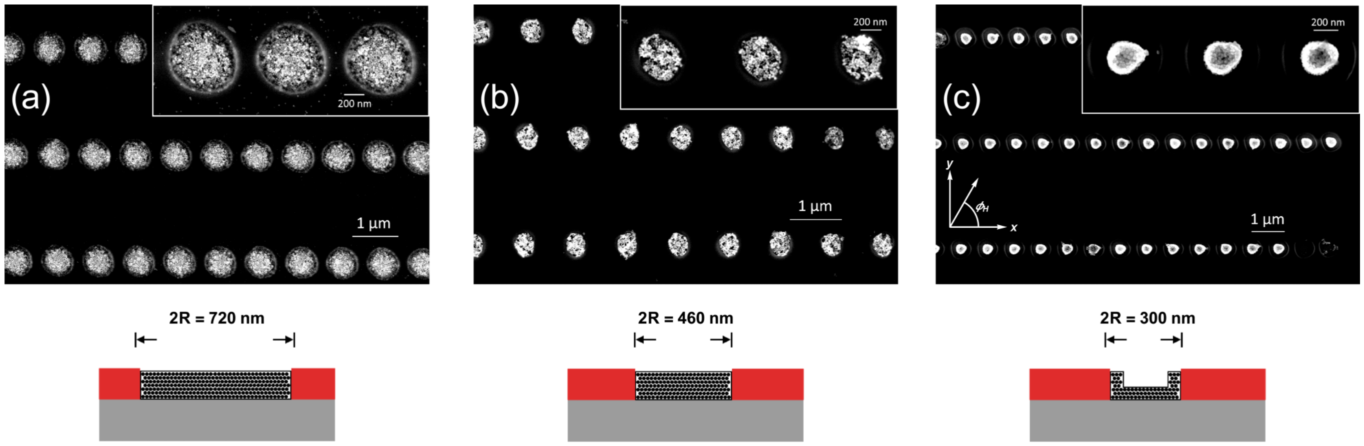

FIG. 1. SEM images and corresponding idealized schematic drawings of single entities of three different samples, one of each set: (a) sample S1_R360_D210 (Set 1), (b) sample S2_R230_D610 (Set 2), and (c) sample S3_R150_D500 (Set 3). Images (a) and (b) show part of the rectangular arrangements of entities of closely packed MNPs where the entities can be considered “full cylinders,” whereas in image (c) MNPs from the center of the entity are removed yielding “hollow cylinders” as building blocks of regular arrangement.

even larger edge-to-volume ratio. Figure 1 shows scanning electron microscopic (SEM) images of three samples, one of each set along with an idealized schematic drawing of a corresponding single entity. The cylindric entities show slight deviations from a perfect circular shape. To estimate the influence of these irregularities on the angle dependence of the FMR signal, the ratio between the radius in the x- and y-directions (R_x and R_y) was determined at different areas of each sample. The average R_x/R_y ratio of each sample is given in Table I together with the corresponding radii R and distances D between the entities. The largest deviation from a perfect aspect ratio of $R_x/R_y = 1$ is only ≈11%. As the demagnetizing field within entities of a comparable aspect ratio is found to be almost isotropic [37], a nearly isotropic behavior of the entities in the sample plane can be expected.

B. Theoretical modeling

Theoretical modeling is indispensable for obtaining deeper insights into the magnetization dynamics of the MNP arrangements and for elucidating how excitations of collective oscillations of the MNPs are affected by the shape of the corresponding arrangement and the presence of an adjacent entity of MNPs [38–40]. In particular, theoretical simulations may unveil the complex eigenmodes of the system. Our code was built for two purposes: First, for obtaining the energetically most preferred configurations under external conditions, and second, for simulating the dynamic behavior of the MNP magnetic dipoles. The Monte Carlo–Metropolis algorithm was used for a fast generation of the preferred configuration of the magnetic dipoles of the MNP arrangement [41,42]. The equation of motion (LLG equation) for each MNP carrying a magnetic moment $\vec{m}_i(\vec{r}, t)$ was solved numerically [39,40,43]. For each MNP, a magnetic moment of $m = 8 \times 10^4 \mu_B$, where μ_B is the Bohr magneton, was chosen, which represents a typical magnetic moment of a magnetite nanoparticle of 20 nm diameter [32]. The effective magnetic field acting on each dipole moment $\vec{m}_i(\vec{r}, t)$ is given by a superposition of the dipolar interaction forces acting on $\vec{m}_i(\vec{r}, t)$ due to the dipoles of nanoparticles in neighboring shells and the external field. To ensure numerical stability during the simulations, both explicit and implicit numerical solvers were tested and compared. This comparison, in addition to a variation of the time step, enabled fast generation of the associated FMR spectrum.

The FMR spectrum is derived by performing a Fourier transformation (FT) of the total magnetization $\vec{M}(\vec{r}, t)$ over 100 periods of the microwave radiation field after transient oscillations disappeared [44]. Performing a two-dimensional FT yields the spatial areas of the MNP arrangement contributing to each resonance.

TABLE I. Overview of the different sample sets.

Sample set	Label	R_x/R_y	R (nm)	D (nm)
1	S1_R360_D210	1.03	360	210
	S1_R320_D150	0.97	320	150
	S1_R340_D80	1.07	340	80
2	S2_R230_D610	0.92	230	610
	S2_R250_D80	0.97	250	80
	S2_R240_D50	0.98	240	50
3	S3_R175_D700	0.94	175	700
	S3_R150_D500	1.11	150	500
	S3_R160_D320	1.02	160	320

III. RESULTS

The angle-dependent FMR experiments were carried out at room temperature using a Bruker ESP 300E spectrometer at X-band frequencies (∼9.5 GHz) for all three sets of samples. The angle was varied in-plane of the sample, such that the vector of the external magnetic field remained parallel to the sample surface at all measurement angles. The orientation $\phi_H = 0^\circ$ is defined by the situation where the external magnetic field points along the x-direction [see Fig. 1(c)], i.e., along the direction of the MNP entity chain, where magnetic interaction between the entities may occur. Contour plots of the FMR amplitude are used to visualize the evolution of each

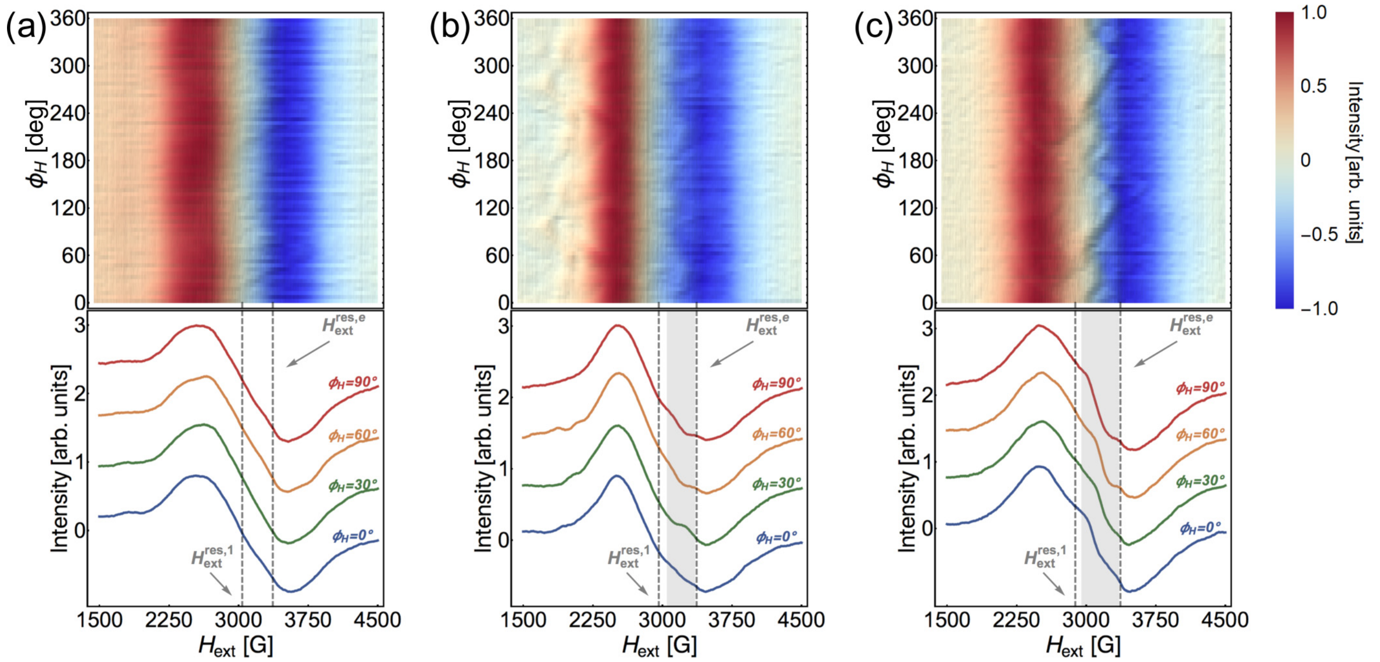

FIG. 2. Measured FMR spectra of the samples of Set 1 consisting of parallel arrangements of chains of cylindrical MNP entities with radii $R = (340 \pm 16)$ nm. The distance D between the neighboring MNP entities of the chain is largest, $D = 210$ nm, for the sample whose results are shown in (a) and smallest, $D = 80$ nm, for the one whose results are shown in (c). The contour plots show the evolution of each resonance in dependence on the orientation of the external magnetic field with respect to the chain axis (angle ϕ_{H}) and on the strength of the external magnetic field. The FMR spectra shown below are recorded at four different angles ϕ_{H}. (a) Sample S1_R360_D210, (b) sample S1_R320_D150, and (c) sample S1_R340_D80.

resonance. The angle is shown on the vertical axis from 0° to 360° and the external field on the horizontal axis, ranging from 1500 to 4500 G. Additionally, four selected spectra recorded at $\phi_{\mathrm{H}} = 0°$, 30°, 60°, and 90°, respectively, are used to show the specific derivative of the absorbance of each sample at these angles.

A. Sample Set 1

The results of FMR measurements for all three samples of Set 1 with MNP entities having the largest radius $R = (340 \pm 16)$ nm are shown in Fig. 2. The spacing D of the cylinder chains varies from left to right from 210 to 80 nm. Sample S1_R360_D210 exhibits one broad resonance with a large full width at half-maximum (FWHM) and a slightly asymmetric shape at $H_{\mathrm{ext}}^{\mathrm{res,1}} = 3050$ G as well as another rather sharp resonance at $H_{\mathrm{ext}}^{\mathrm{res,e}} = 3370$ G. The resonance position of the latter corresponds to a g-factor of ≈2, which is also observed in the FMR spectra of the other two samples of this series. We assign this resonance to free electrons of the polymer surfactant [45] and thus discard it in the discussion below. The resonance $H_{\mathrm{ext}}^{\mathrm{res,1}}$ exhibits no angular dependence, as can be seen in the corresponding contour plot of Fig. 2(a). The situation alters when the distance between the MNP entities of the chain decreases. Already at $D = 150$ nm, the shape of the spectra has changed significantly. While the FMR resonance of sample S1_R360_D210 is only slightly asymmetric around $H_{\mathrm{ext}}^{\mathrm{res,1}}$, the resonance of sample S1_R320_D150 reveals a strong asymmetry, which cannot be explained solely by a single resonance [46]. The presence of more than one resonance is supported by the corresponding contour plot of sample S1_R320_D150 shown in Fig. 2(b), which shows a broad, angle-independent resonance at $H_{\mathrm{ext}}^{\mathrm{res,1}} = 2950$ G and a narrow, slightly angle-dependent resonance $H_{\mathrm{ext}}^{\mathrm{res,2}}$ varying its resonance position between 3100 and 3400 G. This trend is confirmed by the results of sample S1_R340_D80, which exhibits an even smaller spacing $D = 80$ nm between the MNP entities. The broad resonance remains angle-independent at $H_{\mathrm{ext}}^{\mathrm{res,1}} = 2910$ G, while the angular dependence of the high-field resonance $H_{\mathrm{ext}}^{\mathrm{res,2}}$ becomes more pronounced. The angular dependence exhibits a period of 180° corresponding to the twofold symmetry in plane of the chain. It shows an even stronger angular dependence in the range between 3100 and 3400 G than sample S1_R320_D150. We interpret this finding as a signature of magnetic coupling between adjacent MNP entities. Since the effective magnetic field acting on each MNP depends strongly on the number of neighboring MNPs, the effect of adjacent entities should be strongest in case of MNPs, which experience only a weak coupling to other MNPs of their entity. Such MNPs are located near the entity edge, since MNPs on these sites interact with fewer neighbors compared to those on sites in the entity center.

To further support this assumption, additional angle-dependent measurements were also performed on samples of Set 2, which exhibits larger edge-to-volume ratios, since the radii of the cylindrical entities are only about 2/3 of those of Set 1.

B. Sample Set 2

Figure 3(a) shows the results for sample S2_R230_D610. Its FMR spectra exhibit one broad, strongly asymmetric main

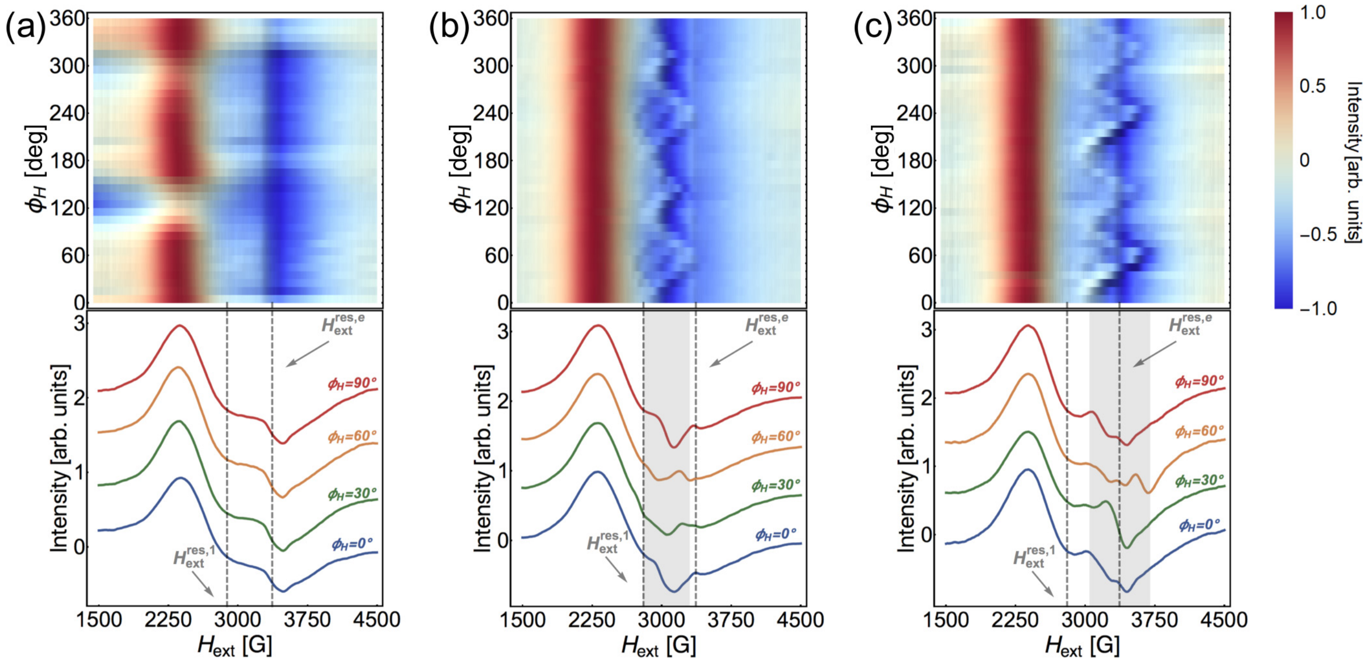

FIG. 3. Measured FMR spectra of the samples of Set 2 consisting of parallel arrangements of chains of cylindrical MNP entities with radii $R = (240 \pm 8)$ nm. The distance D between the neighboring MNP entities of the chain is largest, $D = 610$ nm, for the sample whose results are shown in (a) and smallest, $D = 50$ nm, for the one whose results are shown in (c). The contour plots show the evolution of each resonance in dependence on the orientation of the external magnetic field with respect to the chain axis (angle $\phi_{\rm H}$) and on the strength of the external magnetic field. The FMR spectra shown below are recorded at four different angles $\phi_{\rm H}$. (a) Sample S2_R230_D610, (b) sample S2_R250_D80, and (c) sample S2_R240_D50.

resonance at $H_{\rm ext}^{\rm res,1} = 2900$ G and the resonance at $H_{\rm ext}^{\rm res,e} = 3370$ G of the free electrons. The main resonance, as in the case of Set 1, is of an asymmetric shape that is attributed to the presence of an additional smaller resonance at slightly higher fields. We believe that the 180° symmetry of its resonance position visible in the contour plot of Fig. 3(a) is due to a misalignment of the sample in the resonator yielding a magnetic field component out of plane. Since the main FMR resonance is only slightly asymmetric and the spacing $D = 610$ nm between the MNP entities of the chains is still fairly large, we believe that coupling effects between the entities are negligible. Decreasing the spacing D to 80 nm, corresponding to sample S2_R250_D80, a second high field resonance $H_{\rm ext}^{\rm res,2}$ arises at about 3100 G, with a behavior somewhat similar to that of the high-field resonance of sample S1_R340_D80 of Set 1, which has the same spacing D [see Fig. 3(b)]. The main resonance of sample S2_R250_D80 possesses a resonance field $H_{\rm ext}^{\rm res,1} = 2950$ G that is again independent of the in-plane orientation of the external magnetic field. The high-field resonance $H_{\rm ext}^{\rm res,2}$ shows an increased amplitude compared to sample S2_R230_D610 and a twofold symmetry as apparent in the contour plot. This strong angular dependence of $H_{\rm ext}^{\rm res,2}$ results from enhanced coupling between adjacent MNP entities, which is further confirmed by the results of the third sample of this series, sample S2_R240_D50, where the spacing D is even lower, i.e., 50 nm only [see Fig. 3(c)]. It should be noted that the smaller R of Set 2 compared to Set 1 yields an increased edge-to-volume ratio, which in turn leads to an increased contribution of the high-field resonance to the overall FMR response. It is a further indication and confirmation that this signal originates from near-edge MNPs within the MNP entities. It also implies that the angle-independent main signal $H_{\rm ext}^{\rm res,1}$ predominantly arises from MNPs in the center of the MNP entities. MNPs in this central region experience a magnetic dipolar coupling with the surrounding nearest neighbors, i.e., the MNPs show a collective behavior. Thus, they respond almost isotropically to the external magnetic field, i.e., the magnitude of the effective field acting on their magnetic moment is independent of the orientation of the external magnetic field for those MNPs.

C. Sample Set 3

Finally, FMR measurements of sample Set 3 are shown in Fig. 4. The samples consist of rectangular assemblies of cylindrical entities with a mean radius of $R = 160$ nm only. Furthermore, MNPs of the central region of the entities were removed in order to generate an even larger edge-to-volume ratio. Again all samples of this series exhibit a $g \approx 2$ resonance of free electrons, which we will not discuss further. Figure 4(a) depicts the FMR results of sample S3_R175_D700 with the largest spacing between the entities along the chain, i.e., $D = 700$ nm. The FMR spectra show again an asymmetric main resonance, but at a slightly higher resonance field $H_{\rm ext}^{\rm res,1} = 3010$ G than the main resonances of the corresponding large-D samples of Set 1 and Set 2. This finding is attributed to the fact that considerably fewer particles interact with each other within the smaller hollow MNP entities of Set 3. As a consequence, the dipolar field contribution to the effective field present at the MNP positions is lower, requiring a higher external field to fulfill the resonance condition. A weak additional resonance is also present

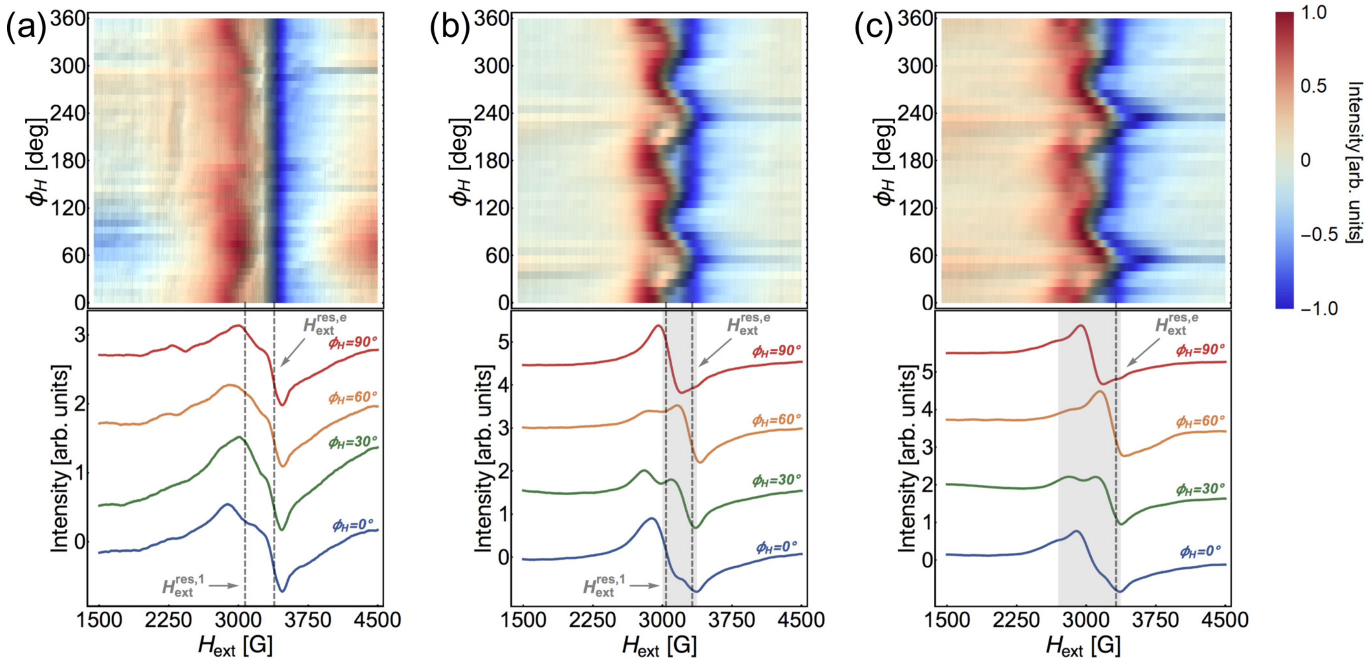

FIG. 4. Measured FMR spectra of the samples of Set 3 consisting of parallel arrangements of chains of hollow-cylindrical MNP entities with radii $R = (160 \pm 10)$ nm. The distance D between the neighboring MNP entities of the chain is largest, $D = 700$ nm, for the sample whose results are shown in (a) and smallest, $D = 320$ nm, for the one whose results are shown in (c). The contour plots show the evolution of each resonance in dependence on the orientation of the external magnetic field with respect to the chain axis (angle ϕ_H) and on the strength of the external magnetic field. The FMR spectra shown below are recorded at four different angles ϕ_H. (a) Sample S3_R175_D700, (b) sample S3_R150_D500, and (c) S3_R160_D320.

at $H_{ext}^{res,2} = 3150$ G. Both resonances do not show a significant angular dependence, i.e., at this D value adjacent entities do not interact. Decreasing the spacing D from 700 to 500 nm in sample S3_R150_D500 introduces an angular dependence of the high-field resonance, while $H_{ext}^{res,1}$ remains still virtually constant as shown in Fig. 4(b). When the distance between neighboring entities is even smaller, i.e., $D = 320$ nm, for sample S3_R160_D320, even the main resonance exhibits an angular dependence indicating that after removal of the MNPs from the center of the cylindrical MNP entities, hardly any MNPs are left, which experience an effective field caused by a collective behavior of surrounding MNPs. This can be seen in the contour plot in Fig. 4(c) in the range between 2600 and 3000 G. Considering the FMR spectra for the four selected angles, it becomes apparent that the first resonance reaches its maximum at $\phi_H = 60^\circ$ and $H_{ext}^{res,1} = 2980$ G, while for $\phi_H = 0^\circ$ it is lower at $H_{ext}^{res,1} = 2850$ G.

D. Micromagnetic simulations

To correlate the different resonances observed in the FMR measurements with characteristic properties of the MNP entities, micromagnetic simulations were carried out for several ordered MNP arrangements. The three arrangements A to C are designed to study the interplay between inter- and intraentity coupling.

(A) Three cylindrical entities are arranged in a line with a spacing of $D = 60$ nm. The entities are initialized by cutting a cylinder with radius $R = 140$ nm and height $h = 80$ nm from a hexagonal grid. As we assume an ideal close packing, the circumferences of the cylinders show some slight hexagon-like deviations from the ideal circular shape. The magnetic moment assigned to each MNP sphere is formally positioned in its center.

(B) Three cylindrical entities are arranged in a line also showing radii of $R = 140$ nm, heights of $h = 80$ nm, and spacings of $D = 60$ nm, but with some MNPs, i.e., magnetic moments, removed from the central region of each entity (radius $r = 80$ nm).

(C) The dimensions and spacings of the second arrangement are retained, but even more MNPs are removed from the center of each entity, i.e., forming a hollow cylinder of closely packed MNP spheres, corresponding to the third MNP arrangement simulated.

In addition to the simulations of the chainlike arrangements A to C, we also performed simulations of isolated MNP entities being equal in size, form, and shape to the central entity of the corresponding chainlike arrangements. These reference calculations allow us to distinguish between interentity effects and intraentity effects in the magnetic response of the arrangements. Therefore, in what follows, we will focus on the magnetic field response of the entities in the center of the arrangements A to C as we consider such a central entity as representative for one located on a site of an infinitely long linear chain of MNP entities of equal spacing. This assumption implies that the interentity coupling of a member of the chain with all others is dominated by that with its nearest-neighboring entities. To confirm this assumption, one can consider an infinitely long chain of magnetic moments m_i each representing one entity. All magnetic moments point along the external field direction and are separated by the distance a. The dipolar field H_{chain} acting on the magnetic

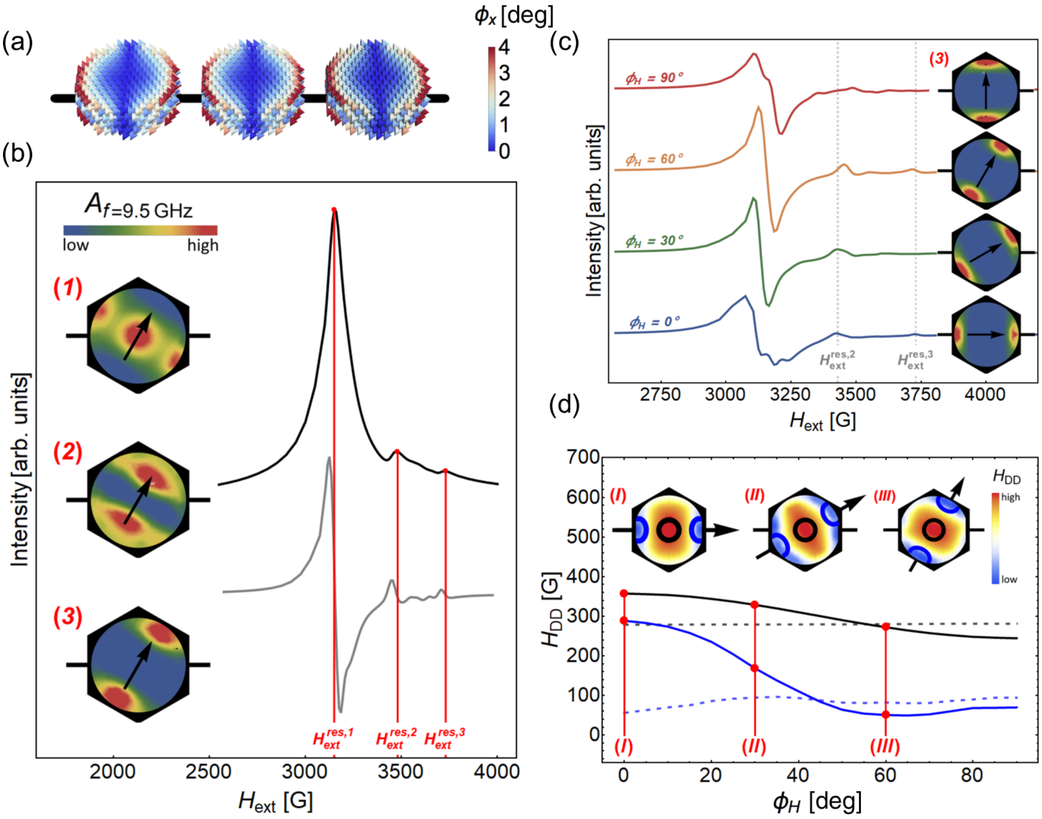

FIG. 5. (a) Orientation of the magnetic moments of the single MNPs of arrangement A for H_{ext} of 4500 G parallel to the line direction ($\phi_{\mathrm{H}} = 0°$). The coloring represents the misalignment ϕ_x of the magnetic moments with respect to the external field direction. (b) Simulated absorbance and its derivative for $\phi_{\mathrm{H}} = 60°$ of the same MNP arrangement, exhibiting a main resonance at $H_{\mathrm{ext}}^{\mathrm{res,1}} = 3150$ G and two additional resonances at $H_{\mathrm{ext}}^{\mathrm{res,2}} = 3490$ G and $H_{\mathrm{ext}}^{\mathrm{res,3}} = 3700$ G. The colored insets unveil the regions, which contribute most to the signals. (c) Varying ϕ_{H} shows an evolution of the high field resonances (2) and (3), showing their highest resonance fields and amplitudes at $\phi_{\mathrm{H}} = 60°$. The colored images represent the FT amplitudes of collective oscillation (3) at the corresponding $H_{\mathrm{ext}}^{\mathrm{res,3}}$ at different ϕ_{H}. (d) Dependence of the dipolar field contribution H_{DD} of the central entity with varying orientation of the external magnetic field ϕ_{H}. The continuous black/blue lines depict the component of H_{DD} parallel to H_{ext} of the central region (indicated by a black circle) and the front/back-edge (indicated by blue ellipses) of the central entity, respectively. The dashed lines represent the component of H_{DD} parallel to H_{ext} of the same locations, but for the corresponding isolated MNP entity. The corresponding areas are shown in the insets for $\phi_{\mathrm{H}} = 0°$, 30°, and 60°.

moment at the origin ($m_{i=0}$) caused by all other magnetic moments of the chain is given by

$$H_{\mathrm{chain}}(r_{\mathrm{i}} = 0) = \sum_{i=1}^{\pm\infty} \frac{\mu_0}{4\pi(|i|a)^3}(3e_{\mathrm{c}}(m_i e_{\mathrm{c}}) - m_i)$$
$$= C\sum_{i=1}^{\infty}\frac{1}{i^3} = C\left(\frac{1}{1^3} + \underbrace{\frac{1}{2^3} + \frac{1}{3^3} + \cdots}_{\approx 0.202}\right), \quad (2)$$

where μ_0 and e_{c} represent the magnetic constant and the lattice vector of the chain, respectively. The sum converges to the value of the Riemann ζ-function at $\zeta(3) \approx 1.202$, also known as the Apéry constant. Thus accounting for nearest-neighbor coupling between entities only, i.e., neglecting all magnetic moments m_i with $i > 1$ in Eq. (2), leads to an error of ≈16.8% ($\approx\frac{0.202}{1.202}$) for the dipole field. This is acceptable since the internal fields are usually one order of magnitude smaller than the external field strengths at which the resonances occur in the micromagnetic simulations, i.e., the error in the simulated resonance position is less than 2%. Figure 5(a) shows the orientation of the magnetic moments of arrangement A consisting of three entirely filled cylindrical entities of MNPs in a line for H_{ext} pointing in the x-direction ($\phi_{\mathrm{H}} = 0°$) with a field strength of 4500 G. The coloring of each magnetic moment represents its orientation with respect to this direction. Additional calculations reveal that for field strengths $H_{\mathrm{ext}} > 2500$ G, the magnetic moments can be regarded as parallel to H_{ext}, i.e., the largest deviation of the orientation of the magnetic moments $\vec{m}_i$ from the external field direction is less than 8°. This implies that the total magnetization of every entity (given by the sum of the magnetizations of its MNPs) in such arrangements is essentially aligned along the external magnetic field at fields where the FMR resonances occur. As a consequence, the dipolar fields of the two total magnetizations of the neighboring entities in arrangements A to C will yield a contribution to the dipolar field H_{DD} at the individual sites of the central MNP entity reflecting the interentity coupling (not shown).

Figure 5(b) shows the simulated FMR spectrum of the central entity of MNP arrangement A for an angle between the magnetic field and the line direction of $\phi_{\mathrm{H}} = 60°$. Both the absorption spectrum and its derivative are shown. The main resonance occurs at $H_{\mathrm{ext}}^{\mathrm{res},1} = 3150$ G and two other resonances can be distinguished at $H_{\mathrm{ext}}^{\mathrm{res},2} = 3470$ G and $H_{\mathrm{ext}}^{\mathrm{res},3} = 3700$ G.

The FMR resonance occurring at a particular field value can be correlated with its characteristic collective excitation by performing a two-dimensional FT of the magnetic structure at this field. The colored insets in Fig. 5(b) show top views of the central cylindrical MNP entity of the assembly of three entities in a line for $H_{\mathrm{ext}} = 3150$, 3470, and 3700 G. The coloring represents the FT amplitudes at the excitation frequency of the microwave $A_{f=9.5\,\mathrm{GHz}}$ (i.e., not the orientation of the magnetic moments, as these are virtually all aligned along the field direction) assigned to each MNP. The higher the FT amplitude of a MNP, the more it contributes to the FMR signal at this field. Thus, the amplitude contour plots derived by the two-dimensional FT for a particular field reveal the locations that predominantly contribute to the FMR signal at this field. It can be seen in the figure that the main signal at $H_{\mathrm{ext}}^{\mathrm{res},1} = 3150$ G originates from resonant excitation of magnetic moments primarily located in the central region of the entity plus a slight contribution of the lateral sides. By increasing the external field strength, the regions of highest activity migrate to the front/back-side of the MNP entity, as can be seen for the resonant excitations (2) and (3) corresponding to external field strengths of $H_{\mathrm{ext}} = 3470$ and 3700 G, respectively.

The simulated angle dependence of the FMR spectra of arrangement A is shown in Fig. 5(c). The FMR spectrum calculated for an angle of $\phi_{\mathrm{H}} = 0^\circ$, where the magnetic field points along the line of the three cylindrical MNP entities, shows a strongly asymmetric resonance at $H_{\mathrm{ext}}^{\mathrm{res},1} = 3150$ G and several additional smaller resonances at higher fields. In the following, we focus on the two strongest ones at $H_{\mathrm{ext}}^{\mathrm{res},2} = 3470$ G and $H_{\mathrm{ext}}^{\mathrm{res},3} = 3700$ G. When ϕ_{H} is increased, the resonance field $H_{\mathrm{ext}}^{\mathrm{res},1}$ of the main resonance is virtually constant, whereas the resonance fields $H_{\mathrm{ext}}^{\mathrm{res},2}$ and $H_{\mathrm{ext}}^{\mathrm{res},3}$ exhibit a strong angular dependence. The angular dependence in the simulation partly originates from the nonideal, hexagonlike shape of the cylinders and thus shows a weak sixfold symmetry. The nonideal shape more strongly affects collective excitation (2) and (3) as the actively contributing MNPs are located at the edge of the MNP entity, whereas the main resonance, which arises from activity of the MNPs located in the center of the entity, exhibits almost no angular dependence. However, the nonideal shape is not solely responsible for the observed angular dependence of the resonance fields. Considering an isolated MNP entity, the pairs of FMR spectra for ϕ_{H} of 0° and 60° (external field perpendicular to a hexagon edge) as well as for 30° and 90° (external field pointing to a hexagon corner) should be identical. However, it is clearly visible that this is not the case in the simulations for the central entity of a chain consisting of three cylinders. This is a strong indication that the presence of the neighboring cylinders and the dipolar field contributions of their total magnetizations (basically aligned along the external field direction) indeed affect the dipolar field at the positions of the MNPs of the central entity, i.e., that the MNP entities separated by $D = 60$ nm couple. To further illustrate this point, we have indicated the resonance fields of the collective excitations (2) and (3) in the calculated FMR spectra for $\phi_{\mathrm{H}} = 0^\circ$ in Fig. 5(c). The resonance fields determined for $\phi_{\mathrm{H}} = 0^\circ$ and 60° as well as for $\phi_{\mathrm{H}} = 30^\circ$ and 90° do not coincide, either for the collective excitation (2) or for (3). Furthermore, the insets of Fig. 5(c) depict spatial mappings of the MNP activity corresponding to the characteristic excitation (3) at its resonance field for the different ϕ_{H} values. It should be noted that the locations of the MNPs within the entity, which contribute most to the activity pattern of the collective excitation (3), rotate about the entity edge following the magnetic field orientation. Thus, the active sites differ for different ϕ_{H}, but the total excitation pattern is virtually the same, i.e., the highest activity is at the front edge facing the magnetic field and the corresponding back edge on the opposite side. Comparable results are also obtained for regular nanodot arrays prepared from patterned ferromagnetic thin films. In those structures also two resonances in the FMR spectra occurred, which were attributed to excitation of the center and the edge of the nanodots [29,31]. However, in contrast to our results, both resonances revealed an angle dependence due to magnetic coupling between the nanodots.

We will now address in more detail the impact of the total magnetizations of neighboring MNP entities on the dipolar field contributions H_{DD} acting on a magnetic moment located within the central MNP entity of the chainlike arrangement of three entities. We will do this analysis for different characteristic sites within the central entity in order to better understand the site's impact on the occurring resonances. The dipolar field contribution at the site of a specific MNP within the central entity may be calculated by summing up the dipolar contributions of all other magnetic moments of MNPs of the entire chainlike arrangement A. The resulting dipolar field vector at this site is subsequently projected onto the direction of the external magnetic field vector in order to obtain its component parallel to H_{ext}. The same calculation was performed for the corresponding isolated entity where the local dipolar fields solely originate from MNPs of the same entity, i.e., it reflects the intraentity coupling only.

The insets in Fig. 5(d) show spatial maps in the top view of the strength of the projected dipolar field contribution H_{DD} at different sites of the central MNP entity of arrangement A for $\phi_{\mathrm{H}} = 0^\circ$, 30°, and 60° at an external field strength of 3500 G. It is clearly visible that the dipolar field near the entity front- or back-side (highlighted by blue ellipses, where the indicated field vector enters and exits the entity) is reduced with respect to the dipolar field in its central region (highlighted by a black circle). These differences result because fewer MNP neighbors contribute to H_{DD} experienced by a MNP located at the edges compared to one in the center of the entity. Such local variations of the dipolar field H_{DD} are directly reflected by the external field value $H_{\mathrm{ext}}^{\mathrm{res}}$ at which the resonant excitation of these MNPs occurs. The resonance condition reads

$$\frac{\omega}{\gamma} = H_{\mathrm{eff}} = H_{\mathrm{ext}}^{\mathrm{res}} + H_{\mathrm{DD}}, \tag{3}$$

where H_{DD} represents the internal magnetic field compared to Eq. (1). The resonance field H_{eff} defined by Eq. (3) represents a property of the MNPs, which is independent of the location of the MNP. It only depends on the microwave frequency ω used in the experiment (which is not varied during experiment) and on γ, which represents its gyromagnetic ratio. It follows that, when the component of H_{DD} parallel to H_{ext} is high, a lower external field strength is required to fulfill

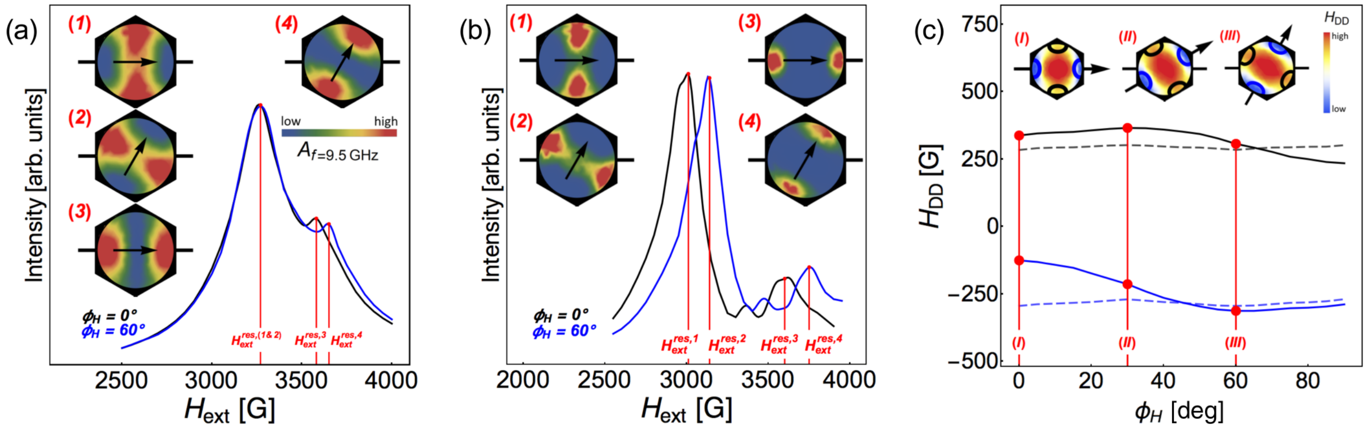

FIG. 6. (a) Simulated absorbance of three interacting circular assemblies with removed MNPs from the central area, corresponding to MNP arrangement B. This additional increase of the edge-to-volume ratio further enlarges the contribution of the high-field resonance. (b) Having removed even more central particles in MNP arrangement C further increases the edge-to-volume ratio, which leads to a larger contribution of the high-field resonance to the absorption spectrum. The insets unveil the regions contributing to the signals. (c) Removing magnetic moments from the central region strongly affects the dipolar field contribution H_{DD}. The continuous black/blue lines depict the component of H_{DD} parallel to H_{ext} the front/back-edge (indicated by blue ellipses) of the left/right-edge (indicated by black circles), respectively, of arrangement C. The corresponding areas are given in the insets for $\phi_{\mathrm{H}} = 0°$, 30°, and 60°. The dashed lines represent the component of H_{DD} parallel to H_{ext} of the same locations, but for the corresponding isolated arrangement.

the resonance condition. Vice versa, a higher external field strength is needed when H_{DD} is low as it is the case for the MNPs located at the edge of the entity. The inset of Fig. 5(d) also shows that the locations at the edge of the entity, where the dipolar field H_{DD} is lowest (blue circles), vary following the orientation of the in-plane magnetic field. This finding is in concordance with the spatial maps of the FMR activity for different ϕ_{H} depicted in Fig. 5(c) and reflects that the excitation pattern of the MNP ensemble for a specific resonance changes gradually with rotating magnetic field and that different MNPs contribute to almost the same excitation pattern.

The main graph of Fig. 5(d) shows the strength of the characteristic dipolar fields H_{DD} in the spatial regions, which yield dominant FT amplitudes of the collective excitations, as a function of the magnetic field orientation ϕ_{H} for the central entity of the chainlike arrangement A as well as of the corresponding isolated entity. Solid lines refer to arrangement A and dashed lines to the isolated entity. Black lines correspond to the dipolar field in the central region of the central entity, which is mainly excited at resonance (1) and marked by a black circle in the maps shown in the insets. This region is stationary when the external field rotates, i.e., it involves basically the same MNPs for all ϕ_{H}. The blue lines correspond to the characteristic front/back-edge regions mainly excited at resonance (3). These regions are marked by blue ellipses, which rotate along the edge of the entity following the in-plane rotation of the external magnetic field, i.e., for each ϕ_{H} different MNPs are involved in the excitation. For the isolated entity, the angle dependence of H_{DD} of the central region (black dashed line) is virtually constant, whereas the dipolar field characteristic for the edge excitation (blue dashed line) exhibits a weak sixfold symmetry. As discussed above, this weak sixfold symmetry is caused by the hexagonal shape of the MNP entity and reflects the differences between MNPs located at edges and corners along the circumference. In concordance with the discussion above, H_{DD} in the central region is always larger than in the front/back region. The corresponding angle-dependent H_{DD} curves for the chainlike arrangement (solid lines) deviate significantly from those of the isolated MNP entity revealing the impact of the interentity coupling on the central entity in the chainlike arrangement. Again, the dipolar field contribution H_{DD} in the center of the entity is always larger than in the front/back regions. However, for both regions H_{DD} significantly decreases as ϕ_{H} increases from 0° to 90°. At $\phi_{\mathrm{H}} = 0°$ the total magnetizations of the MNP entities are aligned in a head-to-tail arrangement along the chain direction. Thus, the dipolar contributions of the two neighboring entities lead to an enhancement of the local dipolar field in both characteristic regions of the central entity. The situation is different at $\phi_{\mathrm{H}} = 90°$. In this case, the total magnetizations of all three entities of the chain are in a side-by-side alignment, consequently the dipolar field contributions of the two total magnetizations of the neighboring entities cause a reduction of the local dipolar fields in the characteristic regions of the central entity of arrangement A. Furthermore, the strong interentity coupling causes a twofold symmetry of $H_{\mathrm{DD}}(\phi_{\mathrm{H}})$, which is more pronounced for the characteristic edge region. The reason is the stronger variation of the intraentity coupling in this region, when it moves along the edge of the entity from a hexagon corner to a hexagon edge. The superposition of the sixfold symmetry of the intraentity coupling and the twofold symmetry of the interentity coupling causes the weak minimum of the $H_{\mathrm{DD}}(\phi_{\mathrm{H}})$ curve at about $\phi_{\mathrm{H}} = 60°$ characteristic for the front/back region of arrangement A.

In the experiment, the front/back regions are responsible for the resonances arising at higher external magnetic fields. These $H_{\mathrm{ext}}^{\mathrm{res}}$ show an angle dependence, best seen in Figs. 2(c) and 3(c). According to the resonance condition, the external field $H_{\mathrm{ext}}^{\mathrm{res}}$ must be larger, when H_{DD} in the region of the contributing MNP is low, and vice versa. The resonance $H_{\mathrm{ext}}^{\mathrm{res}}$, characteristic for the edges of the MNP entities in Fig. 2(c), shows maxima at about 60°, 120°, 240°, and 300°, and minima in between. The two minima corresponding to the external field aligned along the chain direction exhibit the lowest $H_{\mathrm{ext}}^{\mathrm{res}}$ values. Thus, the observed angular dependence of the higher resonances in the measured FMR spectra indeed reflects the interentity dipolar magnetic coupling in the MNP arrangements.

The analysis of the simulated MNP arrangements B and C and their isolated counterparts yields further information about the interplay of intra- and interentity coupling effects in the MNP arrangements. In the series of arrangements B to C, the number of MNPs in the central region of the MNP entities is gradually reduced. Figure 6(a) shows the absorption spectra corresponding to the central entity of MNP arrangement B for two different orientations of the external field. The insets show the associated two-dimensional FT contour plots of the resonances occurring. In comparison with the corresponding results of arrangement A, three major differences can be distinguished: First, the regions actively contributing to the main resonance migrate to the edge of the entities, which becomes apparent by comparing the collective oscillation of the main resonance of arrangement B [Fig. 6(a)] with the one of arrangement A [Fig. 5(b)]. Second, the resonance fields of MNP arrangement B are slightly higher, which is a consequence of the lower dipolar field contributions since fewer magnetic moments of MNPs contribute to H_{DD}. Third, the ratio of the amplitude of the high-field resonance (where the edge regions contribute most to the signal) with respect to the amplitude of the main resonance (originating from the central region and more strongly now also from left/right-side regions) increases as the number of MNPs in the central region decreases, leading to an enlarged edge-to-volume ratio.

The trend is further confirmed by the simulation results of arrangement C. Figure 6(b) shows the absorption spectra of the central entity of MNP arrangement C for two orientations of the external field along with the corresponding two-dimensional FT contour plots of the occurring resonances. Removing even more MNPs from the central region of the entities results in an even stronger contribution and a more pronounced angular dependence of the high-field resonance. Furthermore, it is not only the high-field resonance exhibiting an angular dependence, but also the main resonance. The main resonance now mainly arises from MNPs located in the left/right region. Thus, the collective excitation pattern corresponding to the main resonance is gradually transformed from arrangement A to C, i.e., the corresponding characteristic active region in arrangement A is located in the center of the central entity, while it is located in the left/right side region in arrangement C. Due to its location on the edge of the entity, the left/right side characteristic region, as the back/front characteristic region, rotates along the entity edge as ϕ_{H} is varied. Therefore, the corresponding resonance field exhibits a stronger dependence on ϕ_{H} in good agreement with the FMR results on the third sample set depicted in Fig. 4. These findings clearly prove that the FMR response of an MNP arrangement is strongly affected by the shape of its entities. This explanation is further corroborated by the results shown in Fig. 6(c) for the $H_{\mathrm{DD}}(\phi_{\mathrm{H}})$ curves calculated for the two characteristic regions, i.e., the front/back region (blue ellipses in the corresponding maps shown as an inset) and the left/right region (black ellipses in the corresponding maps shown as an inset). The $H_{\mathrm{DD}}(\phi_{\mathrm{H}})$ curves of the two characteristic regions in the case of the chainlike arrangement C (solid lines) show both a pronounced twofold angle dependence in contrast to the corresponding curves of the isolated counterpart (dashed lines). The differences between $H_{\mathrm{DD}}(\phi_{\mathrm{H}})$ of arrangement C and those of its isolated counterpart can be explained along the lines of the discussion of the results depicted Fig. 5(d) for arrangement A and its isolated counterpart. However, the magnitude of the local dipolar fields and even its orientation in the characteristic regions are different, as is best seen for the back/front region, which corresponds to the same collective excitation in arrangements A and C. The total dipolar field is negative for this region for all angles ϕ_{H} in the case of arrangement C, when all MNPs in the center of the entity are removed, and positive in the case of arrangement A, when the MNPs in the center are present. Thus, changing the degree of filling of the entities of the chain has a strong impact: It changes the collective excitation patterns corresponding to the FMR resonance observed as well as the relative magnitudes of inter- and intraentity coupling.

IV. CONCLUSIONS

We studied the magnetic response of MNP assemblies consisting of chains of cylindrical MNP entities formed out of closely packed spherical magnetite MNPs. A systematic study of the impact of the varying size and shape of the MNP entities as well as the distance between MNP entities along the chain on the FMR spectra was carried out. Utilizing micromagnetic simulations, we clarified the origin and the angular dependence of the FMR resonances observed, and we correlated them with specific collective excitations of the magnetic moments of the MNPs forming the entities of the ordered MNP arrangements. In the case of full cylindrical entities, the main FMR resonance was attributed to resonant magnetic moments located mainly in the center of the entities, while the high-field resonances were assigned to collective excitations of magnetic moments close to the edges of the entities. By removing MNPs from the central region of the entities forming the ordered MNP arrangement, i.e., making them hollow cylinders, the ratio of the amplitudes of the main resonance and the high-field resonances was manipulated. Furthermore, we demonstrated that a magnetic dipolar coupling between the entities forming the chain is present and can be detected in the angle-dependent FMR spectra. As expected, the coupling increases with decreasing spacing between the entities. The effect is more pronounced for smaller entities and mainly affects the resonances of higher collective excitations which originate from MNPs at the edges of the entities. In conclusion, this implies that coupling phenomena between MNP entities are not only affected by the interentity spacing, but they also depend crucially on the dipolar coupling between the single nanoparticles forming the entity, which can be manipulated not only by the arrangement of the nanoparticles but also by the shape of the entity. Using MNP entities as building blocks for arrays of magnetic nanostructures therefore offers an additional degree of freedom for optimizing their magnetic properties for future applications.

[1] G. Salazar-Alvarez, J. Qin, V. Sepelak, I. Bergmann, M. Vasilakaki, K. N. Trohidou, J. D. Ardisson, W. A. A. Macedo, M. Mikhaylova, M. Muhammed, M. D. Baro, and J. Nogues, Cubic versus spherical magnetic nanoparticles: The role of surface anisotropy, Am. Chem. Soc. **130**, 40 (2008).

[2] T. Shinjo, T. Okuno, R. Hassdorf, K. Shigeto, and T. Ono, Magnetic vortex core observation in circular dots of permalloy, Science **289**, 930 (2000).

[3] M. Varon, M. Beleggia, T. Kasama, R. J. Harrison, R. E. Dunin-Borkowski, V. F. Puntes, and C. Frandsen, Dipolar magnetism in ordered and disordered low-dimensional nanoparticle assemblies, Sci. Rep. **3**, 1234 (2013).

[4] J. I. Martin, J. Nogues, K. Liu, J. L. Vincent, and I. K. Schuller, Ordered magnetic nanostructures: Fabrication and properties, J. Magn. Magn. Mater. **256**, 449 (2003).

[5] G. Carlotti, Pushing down the lateral dimension of single and coupled magnetic dots to the nanometric scale: Characteristics and evolution of the spin-wave eigenmodes, Appl. Phys. Rev. **6**, 031304 (2019).

[6] P. Guardia, A. Labarta, and X. Batlle, Tuning the size, the shape, and the magnetic properties of iron oxide nanoparticles, J. Phys. Chem. C **115**, 390 (2011).

[7] R. P. Cowburn, Probing antiferromagnetic coupling between nanomagnets, Phys. Rev. B **65**, 092409 (2002).

[8] R. Pulwey, M. Zölfl, G. Bayreuther, and D. Weiss, Magnetic domains in epitaxial nanomagnets with uniaxial or fourfold crystal anisotropy, J. Appl. Phys. **91**, 7995 (2002).

[9] D. Toulemon, Y. Liu, X. Cattoen, C. Leuvrey, S. Begin-Colin, and B. P. Pichon, Enhanced collective magnetic properties in 2D monolayers of iron oxide nanoparticles favored by local order and local 1D shape anisotropy, Langmuir **6**, 1621 (2016).

[10] S. Jung, B. Watkins, L. DeLong, J. B. Ketterson, and V. Chandrasekhar, Ferromagnetic resonance in periodic particle arrays, Phys. Rev. B **66**, 132401 (2002).

[11] O. N. Martyanov, V. F. Yudanov, R. N. Lee, S. A. Nepijko, H. J. Elmers, C. M. Schneider, and G. Schönhense, Ferromagnetic resonance investigation of collective phenomena in two-dimensional periodic arrays of Co particles, Appl. Phys. A **81**, 679 (2005).

[12] X. K. Hu, H. Dey, N. Liebing, H. W. Schumacher, G. Csaba, A. Orlov, G. H. Bernstein, and W. Porod, Coherent precession in arrays of dipolar-coupled soft magnetic nanodots, J. Appl. Phys. **117**, 243905 (2015).

[13] Y. Takagaki, C. Herrmann, and E. Wiebicke, Dipole-dipole interaction in square arrays of MnAs nanodisks on GaAs(001), J. Phys Condens. Matter **20**, 225007 (2008).

[14] F. Hoffmann, A. Stankoff, and H. Pascard, Evidence for an exchange coupling at the interface between two ferromagnetic films, J. Appl. Phys. **41**, 1022 (1970).

[15] N. I. Polushkin, Excitation of coupled oscillations in lateral ferromagnetic heterostructures, Phys. Rev. B **77**, 180401(R) (2008).

[16] N. I. Polushkin, S. A. Michalski, L. Yue, and R. D. Kirby, Evidence of Long-Wavelength Collective Excitations in Magnetic Superlattices, Phys. Rev. Lett. **97**, 256401 (2006).

[17] S. Mondal, S. Choudhury, S. Barman, Y. Otani, and A. Barman, Transition from strongly collective to completely isolated ultrafast magnetization dynamics in two-dimensional hexagonal arrays of nanodots with varying inter-dot separation, RCS Adv. **6**, 110393 (2016).

[18] J. Pang, S. Xiong, F. Jaeckel, Z. Sun, D. Dunphy, and C. J. Brinker, Free-standing, patternable nanoparticle/polymer monolayer arrays formed by evaporation induced self-assembly at a fluid interface, J. Am. Chem. Soc. **130**, 3284 (2008).

[19] P. Maury, M. Escalante, D. N. Reinhoudt, and J. Huskens, Directed assembly of nanoparticles onto polymer-imprinted or chemically patterned templates fabricated by nanoimprint lithography, Adv. Mater. **17**, 2718 (2005).

[20] S. Maenosono, T. Okubo, and Y. Yamaguchi, Overview of nanoparticle array formation by wet coating, J. Nano. Res. **5**, 5 (2003).

[21] L. J. Heyderman and R. L. Stamps, Artificial ferroic systems: Novel functionality from structure, interactions and dynamics, J. Phys.: Condens. Matter **25**, 363201 (2013).

[22] J. A. De Toro, P. S. Normile, S. S. Lee, D. Salazar, J. L. Cheong, P. Muniz, J. M. Riveiro, M. Hillenkamp, F. Tournus, A. Tamion, and P. Nordblad, Controlled close-packing of ferrimagnetic nanoparticles: An assessment of the role of interparticle superexchange versus dipolar interactions, J. Phys. Chem. C **117**, 10213 (2013).

[23] S. Morup, M. F. Hansen, and C. Frandsen, Magnetic interactions between nanoparticles, Beilstein J. Nanotechnol. **1**, 182 (2010).

[24] G. Muscas, G. Concas, S. Laureti, A. M. Testa, R. Mathieu, J. A. De Toro, C. Cannas, A. Musinu, M. A. Novak, C. Sangregorio, S. S. Lee, and D. Peddis, The interplay between single particle anisotropy and interparticle interactions in ensembles of magnetic nanoparticles, Phys. Chem. Chem. Phys. **20**, 28634 (2018).

[25] V. F. Puntes, P. Gorostiza, D. M. Aruguete, N. G. Bastus, and A. P. Alivisatos, Collective behavior in two-dimensional cobalt nanoparticle assemblies observed by magnetic force microscopy, Nat. Mater. **3**, 263 (2004).

[26] S. Sun, H. Zeng, D. B. Robinson, S. Raoux, P. M. Rice, S. X. Wang, and G. Li, Monodisperse MFe_2O_4 (M=Fe, Co, Mn) Nanoparticles, J. Am. Chem. Soc. **126**, 273 (2004).

[27] M. M. Noginov, N. Noginova, O. Amponsah, R. Bah, R. Rakhimov, and V. A. Atsarkin, Magnetic resonance in iron oxide nanoparticles: Quantum features and effect of size, J. Magn. Magn. Mater. **320**, 2228 (2008).

[28] K. Hu, J. Sun, Z. Guo, P. Wang, Q. Chen, M. Ma, and N. Gu, A novel magnetic hydrogel with aligned magnetic colloidal assemblies showing controllable enhancement of magnetothermal effect in the presence of alternating magnetic field, Adv. Mater. **27**, 2507 (2015).

[29] G. N. Kakazei, X. M. Liu, J. Ding, V. O. Golub, O. Y. Salyuk, R. V. Verba, S. A. Bunyaev, and A. O. Adeyeye, Large four-fold magnetic anisotropy in two-dimensional modulated $Ni_{80}Fe_{20}$ films, Appl. Phys. Lett. **107**, 232402 (2015).

[30] G. N. Kakazei, T. Mewes, P. E. Wigen, P. C. Hammel, A. N. Slavin, Yu. G. Pogorelov, M. D. Costa, V. O. Golub, K. Y. Guslienko, and V. Novosad, Probing arrays of circular magnetic microdots by ferromagnetic resonance, J. Nanosci. Nanotechnol. **8**, 2811 (2008).

[31] G. N. Kakazei, Yu. G. Pogorelov, M. D. Costa, T. Mewes, P. E. Wigen, P. C. Hammel, V. O. Golub, T. Okuno, and V. Novosad, Origin of fourfold anisotropy in square lattices of circular ferromagnetic dots, Phys. Rev. B **74**, 060406 (2006).

[32] A. Fabian, M. Czerner, C. Heiliger, M. T. Elm, D. M. Hofmann, and P. J. Klar, Domain formation in rectangular magnetic nanoparticle assemblies, Phys. Rev. B **98**, 054401 (2018).

[33] C. Martinez-Boubeta, K. Simeonidis, D. Serantes, I. Conde-Leboran, I. Kazakis, G. Stefanou, L. Pena, R. Galceran, L. Balcells, C. Monty, D. Baldomir, M. Mitrakas, and M. Angelakeris, Adjustable hyperthermia response of self-assembled ferromagnetic Fe-MgO core-shell nanoparticles by tuning dipole-dipole interactions, Adv. Funct. Mater. **22**, 3737 (2012).

[34] K. Nakata, Y. Hu, O. Uzun, O. Bakr, and F. Stellacci, Chains of superparamagnetic nanoparticles, Adv. Mater. **20**, 4294 (2008).

[35] K. Butter, P. H. H. Bomans, P. M. Frederik, G. J. Vroege, and A. P. Philipse, Direct observation of dipolar chains in iron ferrofluids by cryogenic electron microscopy, Nat. Mater. **2**, 88 (2003).

[36] A. Fabian, M. T. Elm, D. M. Hofmann, and P. J. Klar, Hierarchical structures of magnetic nanoparticles for controlling magnetic interactions on three different length scales, J. Appl. Phys. **121**, 224303 (2017).

[37] M. Grimsditch, Y. Jaccard, and I. K. Schuller, Magnetic anisotropies in dot arrays: Shape anisotropy versus coupling, Phys. Rev. B **58**, 11539 (1998).

[38] C. Schoeppner, K. Wagner, S. Stienen, R. Meckenstock, M. Farle, R. Narkowicz, D. Suter, and J. Lindner, Angular dependent ferromagnetic resonance analysis in a single micron sized cobalt stripe, J. Appl. Phys. **116**, 033913 (2014).

[39] R. F. L. Evans, W. J. Fan, P. Chureemart, T. A. Ostler, M. O. A. Ellis, and R. W. Chantrell, Atomistic spin model simulations of magnetic nanomaterials, J. Phys. Condens. Matter **26**, 103202 (2014).

[40] B. Skubic, J. Hellsvik, L. Nordström, and O. Eriksson, A method for atomistic spin dynamics simulations: Implementation and examples, J. Phys. Condens. Matter **20**, 315203 (2008).

[41] A. Zaim, M. Kerouad, and Y. El Amraoui, Magnetic properties of a ferrimagnetic core/shell nanocube Ising model: A Monte Carlo simulation study, J. Magn. Magn. Mater. **321**, 1077 (2009).

[42] J. O. Andersson, C. Djurberg, T. Jonsson, P. Svedlindh, and P. Nordblad, Monte Carlo studies of the dynamics of an interacting monodispersive magnetic-particle system, Phys. Rev. B **56**, 13983 (1997).

[43] J. L. Garcia-Palacios and F. J. Lazaro, Langevin-dynamics study of the dynamical properties of small magnetic particles, Phys. Rev. B **58**, 14937 (1998).

[44] S. Jung, J. B. Ketterson, and V. Chandrasekhar, Micromagnetic calculations of ferromagnetic resonance in submicron ferromagnetic particles, Phys. Rev. B **66**, 132405 (2001).

[45] S. Masur, B. Zingsem, T. Marzi, R. Meckenstock, and M. Farle, Characterization of the oleic acid/iron oxide nanoparticle interface by magnetic resonance, J. Magn. Magn. Mater. **415**, 8 (2016).

[46] S. Kopyl, A. A. Timopheev, V. S. Bystrov, I. Bdikin, B. M. S. Teixeira, E. Maevskij, N. A. Sobolev, and A. C. M. Sousa, FMR study of carbon nanotubes filled with Fe_3O_4 nanoparticles, J. Magn. Magn. Mater. **358-359**, 44 (2014).

4.2 Publication 2: Frequency and magnetic field dependent properties of ordered magnetic nanoparticle arrangements

Based on the findings of Publication 1, Publication 2 provides a more detailed analysis of the properties of individual MNP ensembles of circular shape. Here, the ensembles are fabricated using a dispersion of MNPs with diameters of 20 nm which are coated with oleic acid resulting in a spacing between the MNPs of approximately 2 nm. The MNPs have been deposited onto a substrate with a small amount of PMMA added to the solvent. Using a variant of the Langmuir-Schaefer deposition method, 2D hexagonally arranged monolayers have been fabricated. The addition of PMMA facilitates the subsequent patterning of the MNP film into circular ensembles using EBL as, e.g., shown in fig. 3.2 b) for a circularly shaped ensemble with a diameter of 450 nm.

The characterization of the structures has been performed by employing BLS microscopy in collaboration with the research group of H. Schultheiss on both, the structured MNP ensembles and the non-structured thin films. Varying the external driving microwave frequency and the external magnetic field strength, the occurrence of the main and the satellite resonance observed and reported in Publication 1 was confirmed. Performing a 2D mapping of the BLS intensity of the circular MNP ensemble, the associated resonant areas in the center of the structure for the main signal and the rim for the satellite signal are found not only theoretically, but also experimentally. Comparing the results of the ensembles of Publication 2 with the assemblies of Publication 1 of approximately the same diameter, a reduction of the line widths can be observed. This is in good agreement with previous theoretical modeling in the literature [142] highlighting the importance of the degree of order of the MNP arrangement. In addition, frequency dependent measurements at different field strengths of the static external magnetic field have been performed. It has been demonstrated that the line width of the main signal decreases with increasing field, whereas the line width of the satellite signal increases. Furthermore, by increasing the external magnetic field strengths, the intensity ratio of the satellite signal with respect to the main signal decreases.

The samples for this publication have been fabricated by N. Neugebauer. The experimental characterization has been performed by T. Hache and N. Neugebauer. The theoretical simulations and calculations have been performed by N. Neugebauer. This article stems from an enriching scientific dialogue among the authors. Particularly noteworthy is the substantial input from Prof. Peter J. Klar, Dr. Helmut Schultheiss, Prof. Christian Heiliger, Prof. Detlev M. Hofmann, and Dr. Matthias T. Elm, in addition to Nils Neugebauer. Their main contribution was to develop an understanding of the magnetic interactions and to put the experimental and theoretical results into a scientific context.

PHYSICAL REVIEW B **103**, 094438 (2021)

Frequency- and magnetic-field-dependent properties of ordered magnetic nanoparticle arrangements

Nils Neugebauer,[1,*] Toni Hache,[2,3] Matthias T. Elm,[1,4,5] Detlev M. Hofmann,[1,4] Christian Heiliger,[4,6]
Helmut Schultheiss,[2,7] and Peter J. Klar[1,4]
[1]*Institute of Experimental Physics I, Justus Liebig University Giessen, Heinrich-Buff-Ring 16, 35392 Giessen, Germany*
[2]*Helmholtz-Center Dresden-Rossendorf, Institute of Ion Beam Physics and Materials Research, Bautzner Landstraße 400, 01328 Dresden, Germany*
[3]*Institute for Physics, Technische University Chemnitz, 09107 Chemnitz, Germany*
[4]*Center for Materials Research (ZfM/LaMa), Justus Liebig University Giessen, Heinrich-Buff-Ring 16, 35392 Giessen, Germany*
[5]*Institute of Physical Chemistry, Justus Liebig University Giessen, Heinrich-Buff-Ring 17, 35392 Giessen, Germany*
[6]*Institute for Theoretical Physics, Justus Liebig University Giessen, Heinrich-Buff-Ring 16, 35392 Giessen, Germany*
[7]*Technische Universität Dresden, 01062 Dresden, Germany*

(Received 5 November 2020; revised 16 February 2021; accepted 15 March 2021; published 24 March 2021)

We present investigations of the frequency and magnetic field dependent properties of ordered magnetic nanoparticles (MNPs) arrangements consisting of magnetite (Fe_3O_4) nanoparticles with an average diameter of 20 nm by employing micro Brillouin light scattering microscopy. We utilized electron beam lithography to prepare hexagonally arranged, circularly shaped MNP assemblies consisting of a single layer of MNPs using a variant of the Langmuir-Blodgett technique. By comparing the results with nonstructured, layered superlattices of MNPs, further insight into the influence of size and geometry of the arrangement on the collective magnetic properties is obtained. We show that at low static external field strengths, two signals occur in frequency dependent measurements for both nonstructured and structured assemblies. Increasing the static external field strength results in a sharpening of the main signal, while the satellite signal decreases in its intensity and increases in its linewidth. The occurrence of multiple signals at low external field strengths is also confirmed by sweeping the static external field and keeping the excitation frequency constant. Furthermore, two-dimensional spatial mapping of the resonances reveals that the main and the satellite signal originate from the center and the edge, respectively, of a single circular MNP assembly. Micromagnetic simulations confirm these assignments and the dependence of the two signals on the static external field strength, justifying an interpretation of the observed characteristics in terms of different local environments of MNPs forming the MNP assembly.

DOI: 10.1103/PhysRevB.103.094438

I. INTRODUCTION

The development and improvement of novel electronic devices employed in technological applications has driven modern science to find and unveil new approaches, e.g., in preparing novel functional units in electronic circuits or magnetic devices. In recent years, conventional fabrication processes, in which top-down and bottom-up techniques were used to create structured thin films, have been challenged by various novel experimental approaches, which utilize nanoscale components such as magnetic quantum dots, nanoclusters, or likewise nanoparticles [1–8]. Using nanoparticles as building blocks of devices yields additional degrees of freedom to manipulate the fundamental device characteristics, which is not possible using bulk materials only [9–13]. Employing nanoparticles has therefore attracted great and increasing interest during the past decades, since the controllability of their shape, size, composition [14], and arrangement in highly ordered structures is steadily advancing [5,11,14–17]. However, the potential use of nanoparticles in devices for a specific application requires a detailed knowledge of the fundamental interactions of the nanoparticles with their environment. In particular in the case of magnetic nanoparticles this also includes interactions between the nanosized constituents themselves and, thus, their collective behavior [12,18–21]. The fundamental interactions between magnetic nanoparticles are governed by dipole interactions, since the magnetic core of each particle is surrounded by an organic shell (oleic acid), which prevents an electronic contact between the particles and, thus, e.g., exchange interaction between them [22–24]. Certainly, dipole interactions between magnetic nanoparticles become more and more important as the size of the MNPs themselves and the lateral extension of their arrangement in ordered and densely packed structured superlattices decreases [25–29]. In the light of a continuous miniaturization of electronic circuits and magnetic devices, the finite size and the shape of the functional unit becomes more and more important as the surface to volume ratio increases with decreasing arrangement size [30,31]. Depending on the unit's size and shape different local environments occur, which makes a detailed understanding of the interaction

---

[*] Nils.Neugebauer@physik.uni-giessen.de

of the magnetic moment of a MNP with its environment indispensable.

Here we present an investigation of the dipolar interaction between MNPs within circularly structured as well as nonstructured, layered superlattices. Micro Brillouin light scattering (μBLS) microscopy is employed to investigate frequency and external field dependent properties of the corresponding nanoarrangements. On these length scales, dipole interactions between the different constituents determine the overall magnetic properties. Obtaining a deep understanding of the collective dipolar behavior of the MNP arrangements and of their response to the simultaneously applied external magnetic field and microwave field represents the motivation of this work. Insight into the collective properties of the MNP arrangements is further provided by carried out micromagnetic simulations of the corresponding model systems, which enables one to determine the internal dipole field distribution and to identify the active regions of the arrangement yielding a specific resonant excitation.

II. METHODS

A. Sample preparation

The preparation of the ordered MNP arrangement for the μBLS experiments comprises two main fabrication steps. First, a microwave antenna is defined on a high-resistance silicon wafer ($>10\,000\ \Omega/\mathrm{cm}$). The antenna is later used to excite magnetic oscillations within the corresponding magnetic structure in the μBLS experiment. For this purpose, the wafer is coated with a 300-nm-thick PMMA A4 950 K layer. It allows one to pattern the antenna by electron beam lithography (EBL) using a low dose of $D = 1000\ \mu\mathrm{C/cm^2}$ (at an acceleration voltage of 15 kV) during an electron beam lithography (EBL) process. When a low dose is used, PMMA serves as a positive resist. Thus the exposed areas are dissolved during the development process, i.e., during the immersion in an isopropanol-water solution (volume ratio 2:1) for 45 seconds. Subsequently, a 5-nm-thick chromium layer serving as an adhesion aid and a 100 nm gold layer as the antenna material are deposited using electron beam evaporation. The residual PMMA with the metal layers on top are removed by placing the wafer in an ultra sonic bath filled with acetone for 10 minutes at 20 °C yielding the gold antenna of the desired shape.

Afterwards, the second fabrication step is performed. It comprises the formation of the MNP arrangement on top of the antenna structure defined on the silicon wafer. Following the technique proposed by Pang [32] *et al.*, magnetite ($\mathrm{Fe_3O_4}$) MNPs with an average diameter of $d_{\mathrm{NP}} = 20$ nm suspended in toluene (standard variation $\sigma = 5$ nm, particle concentration $c \sim 4.5 \times 10^{13}$ particles/mL - Sigma-Aldrich product number: 725366) are diluted by adding 50 parts of toluene as solvent to one part of the original suspension. In order to enable patterning of the MNPs during the EBL exposure, five parts of 950 K PMMA A4 are added to the diluted MNP suspension. To ensure good homogeneity of the suspension, the mixture is placed in an ultrasonic bath for 10 minutes at room temperature. Subsequently 100 μ L of the MNP-PMMA-toluene mixture are pipetted onto a water subphase within a beaker of 10 cm in diameter. After 30 minutes, the solvent is entirely evaporated and a monolayer of MNPs separated by PMMA is formed. The MNP monolayer is then transferred onto a previously structured silicon wafer resulting in hexagonally arranged MNPs as shown in Fig. 1(a). PMMA between the individual particles can act as a negative resist when using high doses during the EBL exposure. Thus, by using a high dose of $D = 15\,000\ \mu\,\mathrm{C/cm^2}$ in a subsequent EBL process, exposed areas of the MNP monolayer remain after resist development yielding structured MNP arrangements. Figure 1(b) shows an example of a circular MNP arrangement with a diameter of ~450 nm prepared in this way. The preparation of nonstructured, layered superlattices is achieved by increasing the concentration of MNPs in the MNP-PMMA-toluene mixture by a factor of 2, which leads to arrangements consisting of multiple layers up to eight layers thick.

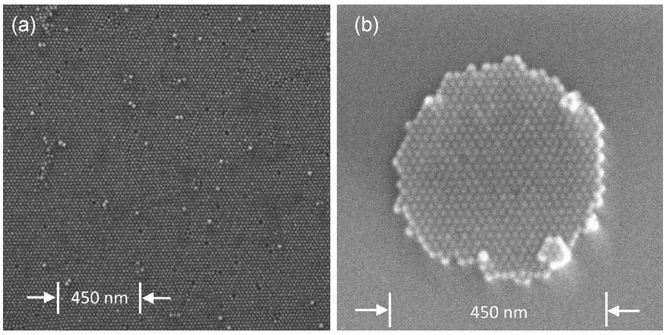

FIG. 1. (a) Using a variant of the Langmuir-Blodgett technique, a mixture of MNPs suspended in toluene and PMMA is pipetted onto a water subphase. During the evaporation of the solvent, a self-assembling process takes place leading to a hexagonal arrangement of a single layer of MNPs which can be transferred to a silicon wafer substrate. (b) After the EBL exposure with high doses and a subsequent development process, patterned MNP arrangements are synthesized.

B. Brillouin light scattering microscopy

To investigate the dynamic properties of magnetic nanostructures, several techniques have been established to excite and detect magnetic oscillations of the corresponding magnetic system. Among these, μBLS has demonstrated an excellent capability of investigating frequency and external magnetic field dependent properties [21,33–35]. In the experiment, a sample is placed on a microwave antenna structure in an external magnetic field B_{ext}, and the response of the magnetic system is analyzed by exposing the sample to photons of a wavelength (frequency) of 532 nm (56 352 THz). In order to resonantly stimulate magnetic oscillations within the sample, the same spot on the sample is also excited with an external microwave field of a defined excitation frequency f_{ext}. The impinging laser photons can then interact with the magnetic excitations, which causes a frequency shift Δf_{phot} by inelastic scattering (Brillouin process). This frequency shift Δf_{phot} represents a distinct signature of the corresponding magnetic oscillation. Thus, measuring the intensity of the inelastically scattered photons for pairs of excitation frequency f_{ext} and

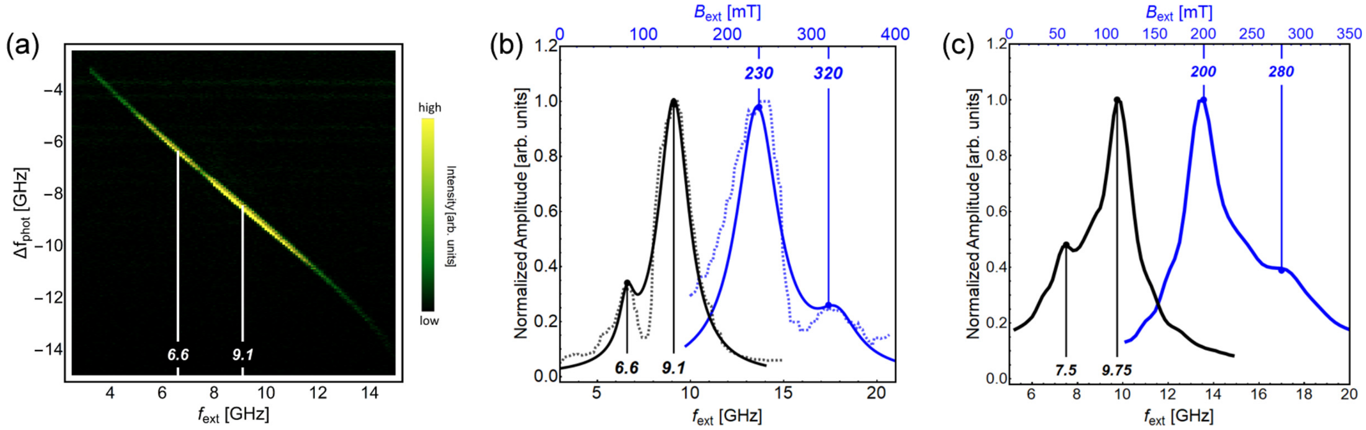

FIG. 2. (a) μBLS intensity of the circularly structured MNP arrangement shown in Fig. 1(b) detected in an microwave excitation frequency range between $f_{\text{ext}} = 0$ GHz and 15 GHz as a function of the external excitation frequency f_{ext}. The data were recorded at an external field strength of $B_{\text{ext}} = 230$ mT. Integrating the data for each f_{ext} leads to an accumulated spectrum as shown in (b) (black dashed curve). It is clearly visible that one main signal is present at $f_{\text{ext}} = 9.1$ GHz, accompanied by a satellite signal located at $f_{\text{ext}} = 6.6$ GHz. Keeping the excitation frequency constant at $f_{\text{ext}} = 9$ GHz and sweeping the external field strength yields the corresponding accumulated field-dependent spectrum which also exhibits two signals (blue dashed curve). The continuous curves represent fits with two Lorentzian curves to the corresponding data. (c) Simulated f_{ext}- (black curve) and B_{ext}-dependent spectra (blue curve) of a hexagonally arranged, circularly shaped MNP assembly. The assembly has a diameter of 300 nm. The frequency-dependent spectrum was calculated for $B_{\text{ext}} = 200$ mT, while the external field strength dependent spectrum was simulated for $f_{\text{ext}} = 9.75$ GHz. Both spectra show a main peak accompanied by a satellite peak of lower intensity in agreement with the experimental results.

frequency shift Δf_{phot} yields insight into the magnetic characteristics of the system at constant B_{ext}. Furthermore, instead of analyzing the f_{ext}-dependent response of the magnetic structure at a constant magnetic field strength B_{ext}, B_{ext}-dependent properties can also be examined for constant f_{ext} by measuring the intensity of inelastically scattered photons versus Δf_{phot} at different external field strength B_{ext}. The frequency and static magnetic field dependent μBLS experiments were performed at room temperature. All measurements were recorded in an excitation frequency range from $f_{\text{ext}} = 0$ GHz to 15 GHz and a magnetic field range from $B_{\text{ext}} = 100$ mT to 400 mT.

C. Theoretical modeling

Micromagnetic modeling of the corresponding MNP arrangements is indispensable for evaluating the results obtained from the μBLS experiments, since the origin of the occurring signals is usually not entirely intuitive. To obtain deeper insight into the dynamic properties of such arrangements, a code has been developed for elucidating the associated characteristics. For details of this code, we refer the reader to our previous publications [36,37].

Since magnetite nanoparticles of diameters of less than 50 nm can be considered as single domain particles [38,39], each MNP can be represented by a single vector $\vec{m}_i(\vec{r}, t)$ (where $\vec{r}$ denotes the position vector and t the time) in the model. It is well known that the magnetization of magnetic nanoparticles is somewhat smaller than that of the bulk material. In our simulations, we assigned a magnetic moment of $m = 2.2 \times 10^5\ \mu_B$, where μ_B is the Bohr magneton, to each MNP, which is in good agreement with previous size dependent investigations of the magnetization [31,40–42]. A magnetic moment $\vec{m}_i(\vec{r}, t)$ interacts only via dipole-dipole interaction with its neighboring moments. Solutions of the time evolution of the whole magnetic system $\vec{M}(\vec{r}, t) = \sum_i \vec{m}_i(\vec{r}, t)$ under an external exciting microwave field $\vec{B}_{\text{mw}}(t, f_{\text{ext}})$ are then obtained by numerical integration of the equation of motion described by the Landau-Lifshitz-Gilbert equation [43]. The effective magnetic field acting on each nanoparticle is then calculated as a superposition of the dipolar contributions $\vec{B}_{\text{dd}}$ of all other magnetic moments, the static external field $\vec{B}_{\text{ext}}$, and the excitation field of the microwave $\vec{B}_{\text{mw}}(t, f_{\text{ext}})$. The corresponding theoretical μBLS spectra are obtained by performing a Fourier transformation of the time-dependent magnetization of each particle $\vec{m}_i(\vec{r}, t)$ over 10 periods for each excitation frequency f_{ext} and external static field strength B_{ext} followed by the integration of the corresponding amplitude A_{FT} over the whole structure.

III. RESULTS

A. Circularly shaped MNP arrangement

Figure 2(a) shows a typical frequency dependent μBLS spectrum obtained from the circularly structured arrangement of MNPs shown in Fig. 1(b). The external static magnetic field strength was set to $B_{\text{ext}} = 230$ mT in the sample plane. The frequency of the externally applied microwave field f_{ext} is shown on the horizontal axis, and the frequency shift of the scattered light Δf_{phot} is shown on the vertical axis. A signal showing an excitation frequency dependence in the range between $f_{\text{ext}} = 4$ GHz and 12 GHz ($\Delta f_{\text{phot}} = -4$ GHz and -12 GHz, respectively, Stokes-Signal) is clearly visible, which arises due to resonant excitations within the magnetic system. Integrating the intensities of all Δf_{phot} for each f_{ext}, i.e., summing up each of the vertical lines of the color plot, leads to an integrated μBLS spectrum shown in Fig. 2(b) as the black dashed curve. The other spectrum (blue dashed curve) is obtained by a magnetic field sweep at constant f_{ext} and will be discussed in more detail below. Note that the two spectra shown in Fig. 2(b) belong to two different abscissas as indicated in the figure. In the following only integrated spectra of these two types will be considered, since they contain all the relevant information.

First, we consider the f_{ext}-dependent measurement in Fig. 2(b). It is clearly visible that in addition to the main signal a satellite resonance with lower intensity can be identified. Fitting the integrated μBLS spectrum with two Lorentzian curves (black continuous curve), the resonance frequency of the main peak located at $f^{\text{res}}_{\text{ext,M}} = 9.1$ GHz and of the satellite peak located at $f^{\text{res}}_{\text{ext,S}} = 6.6$ GHz can be extracted. The resonance condition for each MNP is given by

$$\begin{aligned}\frac{\omega^{\text{res}}_{\text{ext}}}{\gamma} &= B^{\text{res}}_{\text{eff}}\\ &= B^{\text{const}}_{\text{ext}} + B_{\text{int}}\\ &= B^{\text{const}}_{\text{ext}} + B_{\text{dd}},\end{aligned} \tag{1}$$

where $B^{\text{res}}_{\text{eff}}$ denotes the effective local magnetic field at resonance, $\omega^{\text{res}}_{\text{ext}}$ $(=2\pi f^{\text{res}}_{\text{ext}})$ the angular excitation frequency of the microwave field, $\gamma = ge/2m$ the gyromagnetic ratio, g the Landé factor, e the elementary charge, and m the mass of the electron. The effective local magnetic field at resonance is given as the sum of the constant external magnetic field $B^{\text{const}}_{\text{ext}}$ and the internal magnetic field B_{int}. Since the MNPs are not exchange coupled, B_{int} arises only due to the dipolar interaction between neighboring MNPs and therefore, $B_{\text{int}} = B_{\text{dd}}$. As the two signals occur at different resonance frequencies $f^{\text{res}}_{\text{ext,S/M}}$ at constant $B^{\text{const}}_{\text{ext}}$, the two resonances can be attributed to different internal dipole fields B_{dd} and thus to MNPs residing in different local environments within the arrangement. It can be concluded that the satellite peak arises from locations with lower dipole fields which lead to a lower resonance frequency than that of the main peak. This is a strong indication that the satellite peak originates from the edges of the MNP arrangement, while the main signal can be interpreted as a resonant excitation of the bulk of the MNP system [36], which will be discussed in more detail below.

In addition to the f_{ext}-dependent measurement, the blue curves in Fig. 2(b) show an external field dependent spectrum (blue dashed curve) recorded at a constant excitation frequency $f^{\text{const}}_{\text{ext}} = 9$ GHz. As $f^{\text{const}}_{\text{ext}}$ is kept constant and a sweep of the external static field B_{ext} is performed, the spectral features change. This can be explained by rearranging the resonance condition in Eq. (1)

$$\begin{aligned}B^{\text{res}}_{\text{ext}} + B_{\text{dd}} &= \frac{\omega^{\text{const}}_{\text{ext}}}{\gamma}\\ B^{\text{res}}_{\text{ext}} &= \frac{\omega^{\text{const}}_{\text{ext}}}{\gamma} - B_{\text{dd}},\end{aligned} \tag{2}$$

where $B^{\text{res}}_{\text{ext}}$ denotes the external magnetic field strength at which the resonance occurs. As $\omega^{\text{const}}_{\text{ext}}/\gamma$ is kept constant, areas which experience lower dipole fields such as the edges will be in resonance at higher external fields $B^{\text{res}}_{\text{ext}}$ than those with larger dipole fields such as the center of the structure. Therefore, the main peak, which is attributed to the central region of the structure, will appear at lower external field strengths in the spectrum compared to the satellite peak. Fitting the data with two Lorentzian curves (blue continuous lines), the resonance fields of the main peak of $B^{\text{res}}_{\text{ext,M}} = 230$ mT and of the satellite peak of $B^{\text{res}}_{\text{ext,S}} = 320$ mT can be extracted. Using Eq. (2) for the B_{ext}-dependent measurement, the dipole fields of the two resonances can be calculated. Inserting the corresponding values for B_{dd} into Eq. (1) for the f_{ext}-dependent measurement, the resonance frequencies of the main and the satellite peak are expected to be $f^{\text{res}}_{\text{ext,M/S}} = 9$ GHz and 6.5 GHz, respectively. Although the shape of the spectrum is slightly changed, these values are in good agreement with the results of the frequency dependent measurements.

In order to confirm the interpretation of the experimental findings, micromagnetic simulations were carried out for a model system to analyze the f_{ext} and B_{ext}-dependent properties of the circularly structured MNP arrangement shown in Fig. 1. The model system comprises one layer of MNPs, forming a circle with a diameter of 300 nm. Within the circle the MNPs are hexagonally arranged, i.e., densely packed. Figure 2(c) shows the simulated f_{ext} (black curve) and B_{ext}-dependent spectra (blue curve) of the circularly shaped model arrangement. The f_{ext}-dependent spectrum is calculated for an external field strength of $B_{\text{ext}} = 200$ mT. Similar to the μBLS measurement shown in Fig. 2(b), the calculated μBLS spectrum also exhibits two peaks. The main peak is located at a resonance frequency of $f^{\text{res}}_{\text{ext,M}} = 9.75$ GHz and the satellite peak at $f^{\text{res}}_{\text{ext,S}} = 7.5$ GHz. Furthermore, the intensity of the satellite peak is lower with respect to the main peak, which reflects the characteristics deduced from the μBLS experiments. Sweeping B_{ext} instead of f_{ext} and keeping the excitation frequency constant at 9.75 GHz, an external field dependent spectrum is calculated. As in the case of the B_{ext}-dependent experiment shown in Fig. 2(b), a slightly changed shape of the modeled spectrum can be noticed, but the resonance positions of the main and the satellite peak at $B^{\text{res}}_{\text{ext,M}} = 200$ mT and $B^{\text{res}}_{\text{ext,S}} = 280$ mT are again in good agreement with the resonance condition.

The assignment of the main and the satellite signal to the central region and the edge of a single circularly shaped MNP assembly can be confirmed by exploiting a major strength of μBLS microscopy, i.e., obtaining two-dimensional mappings of the scattered light at a given constant frequency f_{ext} and field strength B_{ext}. Such mappings have been performed at the resonance frequencies of the main and satellite signals for a circularly shaped MNP assembly with a diameter of 450 nm. The two maps are shown in the top images of Fig. 3. Note that each pixel of the 2D maps is a convolution of the laser spot with the local activity at f_{ext} at different positions within the MNP assembly. Therefore, the spatial resolution is limited to that of the laser spot prior to a deconvolution of the spatial intensity maps. Nevertheless, a broader distribution of high intensities is expected for the satellite peak in case it originates from the edge, while a more centered intensity distribution is expected for the main resonance if it originates from the center of the MNP structure. In the 2D maps each pixel has a lateral length of 20 nm. The lower two graphs of Fig. 3 depict the intensities measured along the highlighted red [1] and purple [2] lines for the satellite (black curve) and the main resonance (blue curve). It can be seen that the intensity distribution of the satellite resonance shows a broader distribution than the main resonance underlining that the satellite resonance originates from the edges of the MNP system, while the main

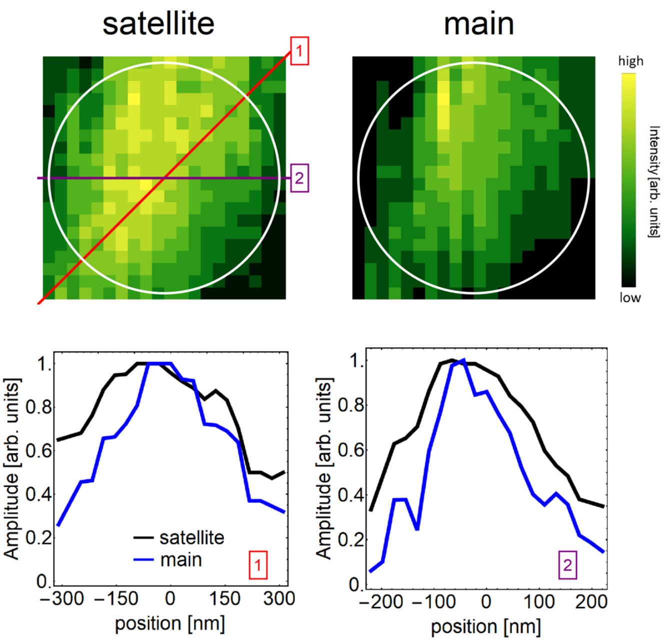

FIG. 3. Top: Spatial maps of the scattered light intensity at the frequency of the satellite peak (left) and the main peak (right) obtained at constant B_{ext} of a circular MNP assembly with a diameter of 450 nm. The white circle indicates the boundary of the MNP assembly and each pixel is 20 nm wide. Bottom: Line scans of the scattered light intensity at the two resonances along the red line [1] and the purple line [2] shown in the top image.

resonances corresponds to an oscillation of the bulk (see also Fig. S1 in the Supplemental Material and the corresponding discussion [44]).

B. Nonstructured, layered MNP arrangement

To corroborate the influence of the edges on the spectral features, we will now compare the observed characteristics of a structured MNP arrangement with those of a nonstructured one. A corresponding scanning electron microscope image of the layered structure is included in the Supplemental Material in Fig. S2 [44]. In Fig. 4(a), four f_{ext}-dependent spectra recorded at four different external field strengths of the nonstructured MNP arrangement are shown as dashed curves. The spectrum taken at $B_{\mathrm{ext}} = 110$ mT (black curve) is considered first. The two resonances are again clearly visible in this spectrum and the corresponding resonance frequencies are obtained by fitting the experimental spectra by two Lorentzian lines, resulting in $f^{\mathrm{res}}_{\mathrm{ext,S/M}} = 3.6$ GHz and 6.2 GHz. When increasing B_{ext} from 110 mT to 170 mT (red curve), the characteristics of the spectral features changes. First, the resonance positions shift to higher f_{ext}, as a result of the altered resonance condition in Eq. (1). Second, at the higher B_{ext} of 170 mT, the ratio of the intensities of the satellite peak with respect to the main peak $A_{\mathrm{S}}/A_{\mathrm{M}}$ is decreased compared to $B_{\mathrm{ext}} = 110$ mT. Furthermore, the linewidth of the satellite peak σ_{S} increases from $\sigma_{\mathrm{S}} = 0.3$ GHz to 0.8 GHz, while the linewidth of the main peak σ_{M} decreases from $\sigma_{\mathrm{M}} = 1.1$ GHz to 0.9 GHz. A further increase of B_{ext} to 230 mT and 300 mT shows that the trends for $f^{\mathrm{res}}_{\mathrm{ext,S/M}}$, $\sigma_{\mathrm{S/M}}$, and $A_{\mathrm{S}}/A_{\mathrm{M}}$ continue almost linearly up to 300 mT. The results are summarized in Fig. 4(c).

Comparing the spectrum of the circularly shaped MNP arrangement shown in Fig. 2(b) (black curve) and the spectrum of the nonstructured, layered system at an external field strength of $B_{\mathrm{ext}} = 230$ mT shown in Fig. 4(a) (blue curve), two differences can be observed. First, the resonance frequencies of the two samples are not the same and differ considerably although the same type of MNPs forming the arrangements are used in the experiment. The resonance frequencies of the circularly shaped assembly are $f^{\mathrm{res}}_{\mathrm{ext,S/M}} = 6.6$ GHz and 9.1 GHz, whereas those of the nonstructured, layered system are higher, $f^{\mathrm{res}}_{\mathrm{ext,S/M}} = 7.2$ GHz and 9.7 GHz. This shift is attributed to the different sizes of the two arrangements. Smaller structures experience smaller dipole fields and

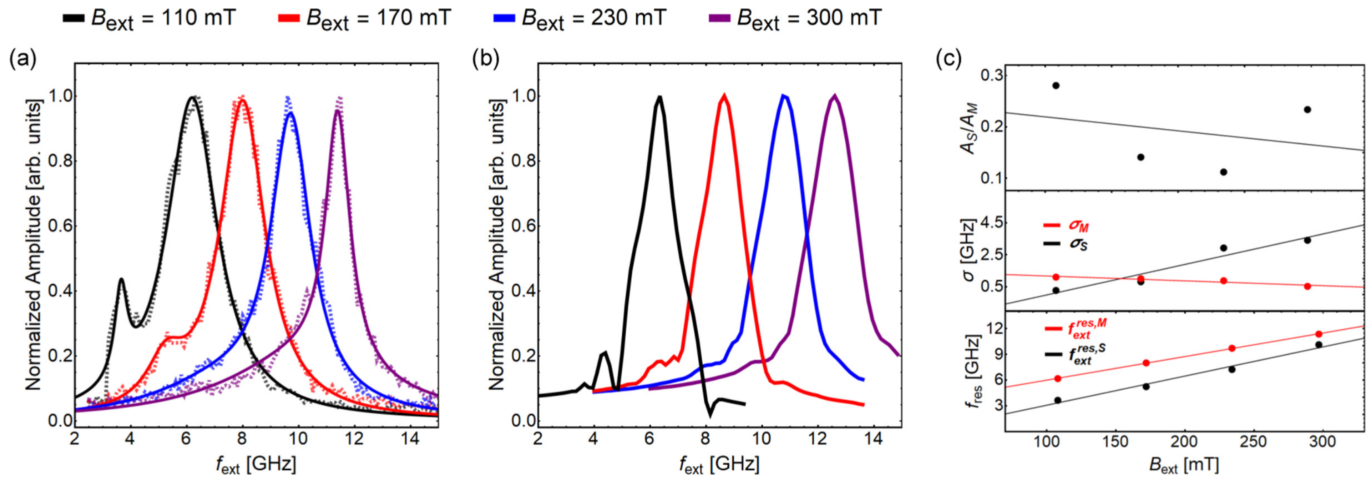

FIG. 4. (a) Integrated μBLS spectra recorded at a nonstructured, layered MNP arrangement at different external field strengths B_{ext}. As f_{ext} increases, the resonance positions are shifted according to the resonance condition [see Eq. (1)]. The linewidths $\sigma_{\mathrm{S/M}}$ of the two resonances and the ratio of their intensities $A_{\mathrm{S}}/A_{\mathrm{M}}$ show distinct field dependencies, which are shown in (c). (b) Simulated frequency dependence of nonstructured, layered MNP assemblies at different B_{ext}. While at low B_{ext} of 100 mT a satellite peak can be recognized, at large B_{ext} of 300 mT its presence is only noticeable as an asymmetry in the low frequency range of the spectrum.

thus lower resonance frequencies are required to fulfill the resonance condition. Second, the amplitude of the satellite peak A_S measured at the circularly shaped MNP assembly is much larger compared to A_S of the nonstructured system. This also results directly from the size of the assemblies. While in the larger nonstructured system only a small fraction of the MNPs are located near the edges, a much larger fraction of MNPs is located close to the edge of the smaller circularly shaped assembly. This finding further indicates that predominantly MNPs close to the edges contribute to the satellite peak resonance.

To further analyze the observed characteristics at different B_{ext} of the nonstructured layered MNP superlattice using micromagnetic simulations, a model system of sufficiently large lateral extension has been defined. This second model system consists of hexagonally arranged moments up to eight layers high and a lateral extension of the entire system of 1 μ m. To mimic the spectra more realistically, not all magnetic moments were incorporated in the Fourier transformation, since the area exposed to the photon beam during the μBLS experiments is only about 300 nm in diameter. Thus, only moments within a cylinder of 300 nm in diameter in the center of the system were included in the Fourier analyses. Figure 4(b) shows the simulated f_{ext}-dependent spectra which can be compared with the corresponding experimental data of Fig. 4(a). The spectrum simulated at $B_{\mathrm{ext}} = 110$ mT possesses a main peak at $f_{\mathrm{ext}} = 6.35$ GHz accompanied by a satellite peak of lower intensity, located at $f_{\mathrm{ext}} = 4.4$ GHz. Increasing the external field strength in the simulation leads to an increase of the resonance frequencies of both the main and satellite mode of the spectrum, until only an asymmetric signal remains in the low frequency range of the spectrum due to a merging satellite and the main peak is in good agreement with the observed characteristics from the μBLS experiments. A possible explanation for the observed merging is that, as the external field strength increases, the angle between the external field and magnetic moments decreases, since their orientation is forced to align parallel to B_{ext}. This effect is most pronounced near the edges of the structure and, thus, areas of low dipole fields located near the edges of the MNP arrangement will be reduced in their lateral extensions. As a result, the intensity of the corresponding signal will decrease accompanied with an increase of its linewidth as the coupling to the central region becomes stronger. Furthermore, as B_{ext} is increased, disorder of the magnetization orientations due to lattice imperfections and particle size deviations becomes less relevant resulting in a narrowing of the linewidth.

A line narrowing of the main peak from $\sigma_M = 1.1$ GHz at $B_{\mathrm{ext}} = 110$ mT to $\sigma_M = 0.6$ GHz at $B_{\mathrm{ext}} = 300$ mT was observed in the experiment [Fig. 4(a)]. Such a line narrowing could not be observed in the simulated spectra of the ideal model system. Instead we even observe a slight increase of the linewidth in the simulated spectra from 0.6 GHz to 0.8 GHz. The line narrowing in the experiment is very likely due to deviations of the real MNP arrangement from the ideal hexagonal arrangement of alike MNPs in terms of their positions, lattice imperfections, and particle sizes. With increasing magnetic field strength, which aligns the magnetizations, the disorder leading to line broadening becomes less significant in relation to the field effects leading to line narrowing. As a consequence, the strong line narrowing arises in the experiment with increasing external field strength. It is not present in the simulations because of the lack of disorder in the ideal MNP arrangement assumed as the model system. For this reason the linewidth of the simulated spectra hardly changes. That it is slightly larger at 300 mT is presumably due to the smaller system size than in the experiment.

C. Influence of the external field strength on the different resonances

In order to analyze in more detail which areas of the arrangement contribute to the two different resonances, the circularly shaped model system based on a MNP monolayer with a diameter of 300 nm is considered again. In Fig. 5(a) simulations of two frequency-dependent μBLS spectra are shown. The spectra were derived for two different external field strengths of $B_{\mathrm{ext}} = 200$ mT (black curve) and 500 mT (blue curve). The spectrum simulated at $B_{\mathrm{ext}} = 200$ mT is the same as in Fig. 2(c). As observed for the nonstructured layered MNP arrangement, the resonance frequencies shift to higher frequencies as the external field strength is increased. Furthermore, increasing B_{ext} results in a decrease of the ratio of the intensity of the satellite peak with respect to that of the main peak A_S/A_M. Deeper insight into the spectral features is obtained by analyzing the local activity within the magnetic structure at the corresponding resonance frequencies. Performing a two-dimensional Fourier transformation at the resonance fields of both spectra in Fig. 5(a), the excitation patterns of the resonances labeled M and S for ‘main’ and ‘satellite,’ respectively, are obtained for both fields. The four patterns are shown in Fig. 5(b). The excitation pattern of the main resonances (M-200 mT and M-500 mT) clearly shows that the main resonance originates from particles located in the center of the structure, while the satellite resonances (S-200 mT and S-500 mT) originate from MNPs located near the edge of the structure (see also Fig. S1 and the corresponding discussion of the Supplemental Material). The excitation patterns of the main resonance for the two different B_{ext} are very similar, except that the areas of highest activity are slightly larger for $B_{\mathrm{ext}} = 500$ mT than for $B_{\mathrm{ext}} = 200$ mT. In contrast, the excitation pattern of the satellite resonance (S-200 mT and S-500 mT) shows a decrease of the active area with increasing B_{ext}. This finding also explains the decrease of the ratio of the intensities A_S/A_M, since less particles near the edge of the structure contribute to the intensity of the satellite resonance with increasing B_{ext}. As the external field strength increases, the magnetic moment of each particle is forced to align with B_{ext}. As a consequence, the oscillation amplitude of each particle in the direction perpendicular to the sample plane denoted as the z axis decreases. Analyzing the dipole field caused by the mutual dipole interaction between the individual particles gives further insight into the observed characteristics. The dipole field B_{dd} acting on the particles is calculated over one period $T = 1/f_{\mathrm{ext}}$ of the microwave field for the resonances S-200 mT and S-500 mT with $f_{\mathrm{ext}} = 7.5$ GHz and 15.6 GHz, respectively. Subsequently, the dipole fields of particles with the same r_x value (meaning particles of the same column) are averaged and normalized to the amplitude of the microwave field $B_{\mathrm{mw}} = 2$ mT. Figure 5(c)

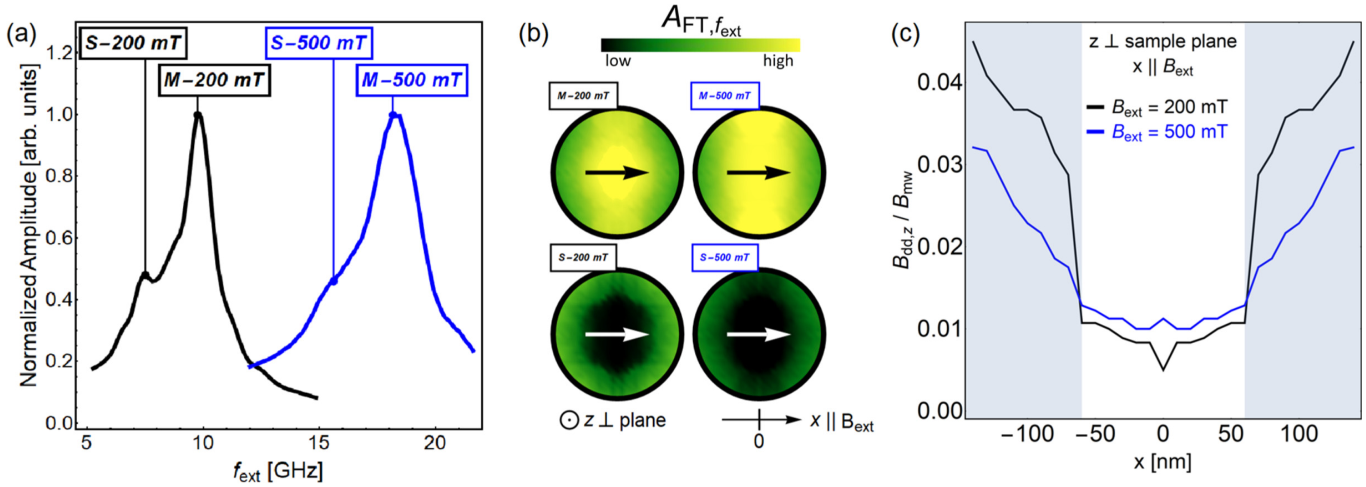

FIG. 5. (a) Simulated f_{ext}-dependent μBLS spectra of a circularly shaped monolayer of MNPs with a radius of 150 nm. The spectra were calculated at $B_{\mathrm{ext}} = 200$ mT (black curve) and 500 mT (blue curve). Increasing B_{ext} results in a shift of the resonance position according to the resonance condition [Eq. (1)]. In addition, a decrease of the intensity of the satellite peak with increasing B_{ext} is visible. (b) Performing 2D-Fourier analyses unveils the active regions of the two resonances. As B_{ext} increases, the active areas of the satellite resonance decrease resulting in a reduction of its relative intensity, compared with the main resonance. The arrows indicate the direction of the external field pointing in the plane of the structure in the x direction. (c) Averaged dipole field $\vec{B}_{\mathrm{dd,z}}$ in the direction perpendicular to the sample plane (z axis) over one period $T = 1/f_{\mathrm{ext}}$ with $f_{\mathrm{ext}} = 7.5$ GHz and 15.6 GHz (S-200 mT and S-500 mT). The vertical axis is normalized to the strength of the microwave field $B_{\mathrm{mw}} = 2$ mT.

shows the averaged z component of the dynamic dipole field B_{dd} of each column of the model system as a function of the x position of the column as indicated in the lower panel of Fig. 5(b). As $B_{\mathrm{ext}} \parallel x$ increases from 200 mT (black curve) to 500 mT (blue curve), the averaged $B_{\mathrm{dd}} \parallel z$ near the edges of the structure decreases, whereas only slight variations in the center of the structure are observable. It follows that, as the external field strength increases, the difference of the averaged dipole field diminishes with respect to those of the center. Thus, the capability to respond to the microwave field of MNPs near the edge of the structure decreases, which results in the observed merging of the satellite resonance and the main resonance at high external field strengths.

IV. CONCLUSIONS

We investigated the dynamic response of hexagonally ordered, circularly structured MNP arrangements utilizing μBLS microscopy. Depending on the external conditions, two resonances appear in the spectra, which can be attributed to different areas within the magnetic system. While the main resonance originates from the central region of the MNP arrangement, the observed satellite resonance is assigned to magnetic particles near the edges of the system. Frequency dependent measurements were carried out at various external fields, revealing a distinct dependence on the external magnetic field strength. Micromagnetic simulations unveiled the different characteristics of the dipolar coupling between the MNPs within the different locations of the arrangement. The dipolar coupling between the MNPs has a major impact on the lineshape of the μBLS spectra. Increasing the external field strength leads to a reduction of the effective areas of lower internal magnetic fields accompanied with a reduction of the intensity of the corresponding satellite resonance compared to the main resonance. Thus, it has been demonstrated that the response of the MNP arrangement is very sensitive to an external magnetic field and the frequency of the microwave excitation. A full understanding of these dependencies is essential for successfully incorporating such magnetic structures into devices. In the future, we plan to extend our studies to higher frequency shifts of the scattered light. Such studies may then yield information about excitations of the exchange-coupled atomic magnetic moments within the individual MNPs.

ACKNOWLEDGMENTS

We acknowledge computational resources provided by the HPC Core Facility and the HRZ of the Justus-Liebig-University Giessen. In addition, the authors thank Marcel Giar and Philipp Risius (HPC Core Facility, Justus Liebig University Giessen) for their administrative support.

---

[1] J.-H. Choi, H. Wang, S. J. Oh, T. Paik, P. S. Jo, J. Sung, X. Ye, T. Zhao, B. T. Diroll, C. B. Murray, and C. R. Kagan, Exploiting the colloidal nanocrystal library to construct electronic devices, Science **352**, 205 (2016).

[2] C. R. Kagan, E. Lifshitz, E. H. Sargent, and T. V. Talapin, Building devices from colloidal quantum dots, Science **353**, aac5523 (2016).

[3] H. Zeng, C. T. Black, R. L. Sandstrom, P. M. Rice, C. B. Murray, and S. Sun, Magnetotransport of magnetite nanoparticle arrays, Phys. Rev. B **73**, 020402(R) (2006).

[4] C. Jiang, S. M. Ng, C. W. Leung, and P. W. T. Pong, Magnetically assembled iron oxide nanoparticle coatings and their integration with pseudo-spin-valve thin films, J. Mater. Chem. C **5**, 252 (2017).

[5] T. Paik, H. Yun, B. Fleury, S.-H. Hong, P. S. Jo, Y. Wu, S.-J. Oh, M. Cargnello, H. Yang, C. B. Murray, and C. R. Kagan, Hierarchical materials design by pattern transfer printing of self-assembled binary nanocrystal superlattices, Nano Lett. **17**, 1387 (2017).

[6] B. H. Zhou and J. D. Rinehart, Pseudo spin valve behavior in colloidally prepared nanoparticle films, ACS Appl. Electron. Mater. **1**, 1065 (2019).

[7] M. Fischer, M. T. Elm, S. Sakita, S. Hara, and P. J. Klar, Magnetoresistance effects and spin-valve like behavior of an arrangementof two MnAs nanoclusters, Appl. Phys. Lett. **106**, 032401 (2015).

[8] M. T. Elm, S. Hara, Transport properties of hybrids with ferromagnetic MnAs nanoclusters and their potential for new magnetoelectronic devices, Adv. Mater. **26**, 8079 (2014).

[9] K. Yakushiji, F. Ernult, H. Imamura, K. Yamane, S. Mitani, K. Takanashi, S. Takahashi, S. Maekawa, and H. Fujimori, Enhanced spin accumulation and novel magnetotransport in nanoparticles, Nat. Mater. **4**, 57 (2005).

[10] G. Song, M. Ranjbar, D. R. Daughton, and R. A. Kiehl, Nanoparticle-induced anomalous Hall effect in graphene, Nano Lett. **19**, 7112 (2019).

[11] A. Dong, J. Chen, P. M. Vora, J. M. Kikkawa, and C. B. Murray, Binary nanocrystal superlattice membranes self-assembled at the liquid-air interface, Nature (London) **466**, 474 (2010).

[12] L. Giovannini, F. Montoncello, and F. Nizzoli, Effect of interdot coupling on spin-wave modes in nanoparticle arrays, Phys. Rev. B **75**, 024416 (2007).

[13] C. Michel, M. T. Elm, B. Goldlücke, S. D. Baranovskii, P. Thomas, W. Heimbrodt, and P. J. Klar, Tailoring the magnetoresistance of MnAs/GaAs:Mn granular hybrid nanostructures, Appl. Phys. Lett. **92**, 223119 (2008).

[14] M. A. Boles, M. Engel, and D. V. Talapin, Self-assembly of colloidal nanocrystals: From intricate structures to functional materials, Chem. Rev. **116**, 11220 (2016).

[15] A. Dong, J. Chen, S. J. Oh, W. K. Koh, F. Xiu, X. Ye, D. K. Ko, K. L. Wang, C. R. Kagan, and C. B. Murray, Multiscale periodic assembly of striped nanocrystal superlattice films on a liquid surface, Nano Lett. **11**, 841 (2011).

[16] E. Shevchenko, D. V. Talapin, N. A. Kotov, S. O'Brien, and C. B. Murray, Structural diversity in binary nanoparticle superlattices, Nature (London) **439**, 55 (2006).

[17] X. Ye, C. Zhu, P. Ercius, S. N. Raja, B. He, M. R. Jones, M. R. Hauwiller, Y. Liu, T. Xu, and P. A. Alivisatos, Structural diversity in binary superlattices self-assembled from polymer-grafted nanocrystals, Nat. Commun. **6**, 10052 (2015).

[18] S. Mamica, M. Krawczyk, M. L. Sokolovskyy, and J. Romero-Vivas, Large magnonic band gaps and spectra evolution in three-dimensional magnonic crystals based on magnetoferritin nanoparticles, Phys. Rev. B **86**, 144402 (2012).

[19] F. Vernay and H. Kachkachi, Single-particle versus collective effects in assemblies of nanomagnets: Screening, J. Magn. Magn. Mater. **500**, 166286 (2020).

[20] B. W. Zingsem, T. Feggeler, A. Terwey, S. Ghaisari, D. Spoddig, D. Faivre, R. Meckenstock, M. Farle, and M. Winklhofer, Biologically encoded magnonics, Nat. Commun. **10**, 4345 (2019).

[21] S. Tacchi, G. Gubbiotti, M. Madami, and G. Carlotti, Brillouin light scattering studies of 2D magnonic crystals, J. Phys.: Condens. Matter **29**, 073001 (2017)

[22] J. Chen, A. Dong, J. Cai, X. Ye, Y. Kang, J. M. Kikkawa, and C. B. Murray, Collective dipolar interactions in self-assembled magnetic binary nanocrystal superlattice membranes, Nano Lett. **10**, 5103 (2010).

[23] Z. Yang, J. Wei, P. Bonville, and M. P. Pileni, Engineering the magnetic dipolar interactions in 3D binary supracrystals via mesoscale alloying, Adv. Funct. Mat. **25**, 4908 (2015).

[24] M. Anand, J. Carrey, and V. Banerjee, Role of dipolar interactions on morphologies and tunnel magnetoresistance in assemblies of magnetic nanoparticles, J. Magn. Magn. Mater. **454**, 23 (2018).

[25] H. T. Nguyen, and M. G. Cottam, Dipole-exchange spin waves in ferromagnetic nanostructures with spherical geometries, Surf. Rev. Lett. **15**, 727 (2008).

[26] P. Poddar, T. Telem-Shafir, T. Fried, and G. Markovich, Dipolar interactions in two- and three-dimensional magnetic nanoparticle arrays, Phys. Rev. B **66**, 060403(R) (2002).

[27] P. Bender, E. Wetterskog, D. Honecker, J. Fock, C. Frandsen, C. Moerland, L. K. Bogart, O. Posth, W. Szczerba, H. Gavilan, R. Costo, M. T. Fernandez-Diaz, D. González-Alonso, L. Fernandez Barquin, and C. Johansson, Dipolar-coupled moment correlations in clusters of magnetic nanoparticles, Phys. Rev. B **98**, 224420 (2018).

[28] K. L. Krycka, J. J. Rhyne, S. D. Oberdick, A. M. Abdelgawad, J. A. Borchers, Y. Ijiri, S. A. Majetich, and J. W. Lynn, Spin waves across three-dimensional, close-packed nanoparticles, New J. Phys. **20**, 123020 (2018).

[29] G. Singh, H. Chan, A. Baskin, E. Gelman, N. Repnin, P. Kral, and R. Klajn, Self-assembly of magnetite nanocubes into helical superstructures, Science **345**, 1149 (2014).

[30] R. Moreno, S. Poyser, D. Meilak, A. Meo, S. Jenkins, V. K. Lazarov, G. Vallejo-Fernandez, S. Majetich, and R. F. L. Evans, The role of faceting and elongation on the magnetic anisotropy of magnetite Fe_3O_4 nanocrystals, Sci. Rep. **10**, 2722 (2020).

[31] S. D. Oberdick, A. Abdelgawad, C. Moya, S. Mesbahi-Casey, D. Kepaptsoglou, V. K. Lazarov, R. F. L. Evans, D. Meilak, E. Skoropata, J. van Lierop, I. Hunt-Isaak, H. Pan, Y. Ijiri, K. L. Krycka, J. A. Borchers, and S. A. Majetich, Spin canting across core/shell $Fe_3O_4/Mn_xFe_{3-x}O_4$ nanoparticles, Sci. Rep. **8**, 3425 (2018).

[32] J. Pang, S. Xiong, F. Jaeckel, Z. Sun, D. Dunphy, and C. J. Brinker, Free-standing, patternable nanoparticle/polymer monolayer arrays formed by evaporation induced self-assembly at a fluid interface, J. Am. Chem. Soc. **130**, 3284 (2008).

[33] A. V. Chumak, V. I. Vasyuchka, A. A. Serga, and B. Hillebrand, Magnon spintronics, Nat. Phys. **11**, 453 (2015).

[34] Q. Wang, P. Pirro, R. Verba, A. Slavin, B. Hillebrand, and A. V. Chunmak, Reconfigurable nanoscale spin-wave directional coupler, Science Adv. **4**, e1701517 (2018).

[35] T. Sebastian, K. Schultheiss, B. Obry, B. Hillebrands, and H. Schultheiss, Micro-focused Brillouin light scattering: imaging spin waves at the nanoscale, Frontiers in Physics **3**, 35 (2015).

[36] N. Neugebauer, A. Fabian, M. T. Elm, D. M. Hofmann, M. Czerner, C. Heiliger, and P. J. Klar, Investigation of the dipole interaction in and between ordered arrangements of magnetic nanoparticles, Phys. Rev. B **101**, 104409 (2020).

[37] A. Fabian, M. Czerner, C. Heiliger, M. T. Elm, D. M. Hofmann, and P. J. Klar, Domain formation in rectangular-magnetic nanoparticle assemblies, Phys. Rev. B **98**, 054401 (2018).

[38] K. M. Krishnan, A. B. Pakhomov, Y. Bao, P. Blomqvist, Y. Chun, M. Gonzales, K. Griffin, X. Ji, and B. K. Roberts, Nanomagnetism and spin electronics: Materials, microstructure and novel properties, J. Mater. Sci. **41**, 793 (2006).

[39] S. Singamaneni, V. Bliznyuk, C. Binek, and E. Y. Tsymbal, Magnetic nanoparticles : Recent advances in synthesis, self-assembly and applications, J. Mater. Chem. **21**, 16819 (2011).

[40] Z. Nedelkoski, D. Kepaptsoglou, L. Lari, T. Wen, R. A. Booth, S. D. Oberdick, P. L. Galindo, Q. M. Ramasse, R. F. L. Evans, S. Majetich, and V. K. Lazarov, Origin of reduced magnetization and domain formation in small magnetite nanoparticles, Sci. Rep. **7**, 45997 (2017).

[41] S. Sun, H. Zeng, D. B. Robinson, S. Raoux, P. M. Rice, S. X. Wang, and G. Li, Monodisperse MFe_2O_4 (M = Fe, Co, Mn) Nanoparticles, J. Am. Chem. Soc. **126**, 273 (2004).

[42] X. Batlle, N. Perez, P. Guardia, O. Iglesias, A. Labarta, F. Bartolome, L. M. Garcia, J. Bartolome, A. G. Roca, M. P. Morales, and C. J. Serna, Magnetic nanoparticles with bulklike properties, J. Appl. Phys. **109**, 07B524 (2011).

[43] R. F. L. Evans, W. J. Fan, P. Chureemat, T. A. Ostler, and R. W. Chantrell, Atomistic spin model simulations of magnetic nanomaterials, J. Phys.: Condens. Matter **26**, 103202 (2014).

[44] See Supplemental Material at http://link.aps.org/supplemental/10.1103/PhysRevB.103.094438 for a more detailed analysis of the 2D-BLS maps of the main and the satellite resonance and a discussion of the lattice defects of the nonstructured, layered MNP arrangement.

Supplementary Material

Figure S1 shows results of BLS mapping of a circularly shaped MNP arrangement, in order to assign spatial locations to the two observed resonances. Figure S1 (a) shows an integrated BLS spectrum of a circularly-shaped MNP assembly with a diameter of 450 nm at an external field strength of $B_{\text{ext}} = 230$ mT. The two resonances (a satellite and a main resonance) can be identified at $f_{\text{ext,S}} = 6.6$ GHz and $f_{\text{ext,M}} = 9.1$ GHz. Measuring the intensity of the signals at the resonance frequencies (whilst keeping B_{ext} constant at 230 mT) at different positions on the sample yields spatial mapping of the active regions. Note that the 2D-maps are a convolution of the laser spot with the actual oscillation of the active regions. Therefore, the spatial resolution is limited to that of the laser spot prior to a deconvolution of the spatial intensity maps. Nevertheless, a broader distribution of high intensities is expected for the satellite peak, while a more centered intensity distribution is expected for the main resonance. The top row of images in figure S1 (b) shows the mapping for each resonance (compare with Fig. 3 of the manuscript), where each pixel has a lateral length of 20 nm. The second row depicts linescans of the intensity measured along the highlighted red [1] and purple [2] lines for the satellite (black curve) and the main resonance (blue curve). It can be seen that the intensity distribution of the satellite resonance shows a broader distribution than the main resonance. This can be understood by considering the corresponding simulated 2D-BLS-maps shown in the top row of figure S1 (c), which depict the convolution of the spatial locations of the active regions of each mode (compare with Fig. 5 (b) of the manuscript) with the Gaussian intensity profile of the laser with a line width of 300 nm. In addition to the 2D-maps, the intensities measured along the highlighted red [1] and purple [2] lines are also shown in the bottom row of figure S1 (c). The intensity linescans clearly reveal a broader intensity distribution for the satellite resonance than for the main resonance confirming that the latter signal originates from the center of the MNP assembly whereas the satellite signal originates from its edges.

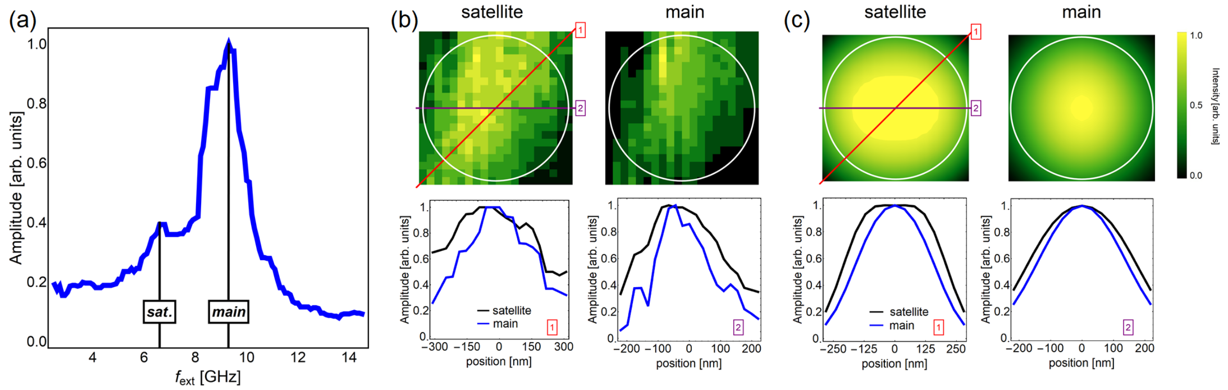

Figure S1: (a) Integrated BLS spectrum of a circularly-shaped MNP assembly at an external field strength of $B_{\text{ext}} = 230$ mT. The satellite resonance is observed at $f_{\text{ext,S}} = 6.6$ GHz, while the main resonance appears at $f_{\text{ext,M}} = 9.1$ GHz. (b) The top row shows 2D-maps of the two observed modes of a circular shaped MNP arrangement at the corresponding resonance frequencies $f_{\text{ext,S/M}} = 6.6$ GHz and 9.1 GHz (compare with Fig. 3 of the manuscript). The second row shows the intensity distributions measured along the highlighted red [1] and purple [2] lines. (c) The top row shows simulated 2D-BLS-maps of the circularly-shaped MNP assembly for the satellite and the main resonance. These are obtained as a convolution (compare with Fig. 5 (b) of the manuscript). The bottom row depicts the simulated intensity along the highlighted red [1] and purple [2] lines.

Figure S2 (a) shows a low magnification SEM image of the non-structured, layered MNP assembly investigated in section III. Results - B. Non-structured, layered MNP arrangement. The green spot within the marked cross depicts the laser spot during the measurement. Contours of the MNP-assembly are indicated by white lines. Figure S2 (b) shows an high magnification SEM image of the white rectangle in figure S2 (a). Several defects on various length scales can be identified, such as cracks, different lattices orientations, different stack heights, vacancies, and isolated MNP-islands. All these defects constitute disorder which at low external field strengths leads to a linewidth broadening in the BLS spectra, as the influence on the dynamic properties of the local environment is more pronounced at lower external field strengths than at high fields.

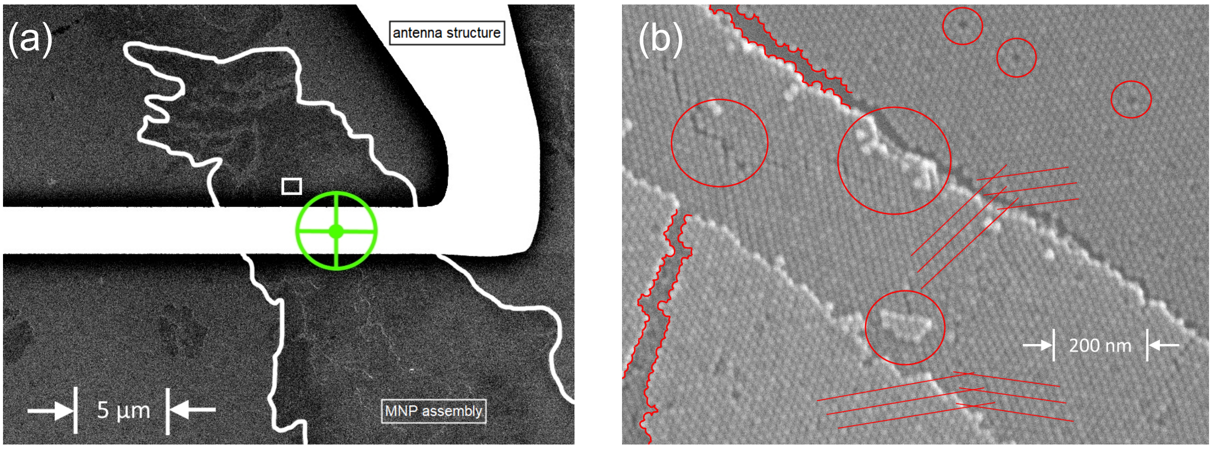

Figure S2: (a) Low magnification SEM image of the nonstructured, layered MNP arrangement. Contours indicated by white lines. (b) High magnification SEM image of the highlighted rectangle in figure (a). Several defects on different length scales of a perfectly, hexagonally arranged MNP system can be observed, such as cracks, different lattices orientations, different stack heights, vacancies, and isolated MNP-islands.

4.3 Publication 3: Distance- and size-dependence of the interactions within highly ordered magnetic nanoparticle mesocrystals

The previous two publications reported on dipolar coupling phenomena at the level of the whole MNP assembly/ensemble, where the size of the individual assemblies/ensemble and the spacing between them has been investigated, focusing on the scale of some hundreds of nanometers. Thus, these structures may be conceived in the range on length scales at the border between the mesoscale and the macroscale as illustrated in fig. 1.1. As the employment of MNPs introduces additional degrees of freedom on even lower length scales, investigations concerning the characteristics at the border between mesoscale and atomic scale have been performed in Publication 3.

In Publication 3, an investigation of MNPs of different diameters ranging from $d_{\mathrm{MNP}} = 9\,\mathrm{nm}$ to $d_{\mathrm{MNP}} = 18\,\mathrm{nm}$ has been published in collaboration with the research group of X. Ye. The MNPs have been coated with polystyrene of different molecular weight, which facilitates a precise manipulation of the spacing between the MNPs ranging from $d_{\mathrm{spacer}} = 6\,\mathrm{nm}$ to $d_{\mathrm{spacer}} = 15\,\mathrm{nm}$. The samples have then been characterized performing FMR experiments which reveal a distinct dependence of the spectral features on both, d_{MNP} and d_{spacer}. On the one hand, increasing d_{spacer} at fixed d_{MNP} yields an increase of the field strength B_{res} at which the resonance occurs, while the line width remains unchanged. On the other hand, increasing d_{MNP} at fixed d_{spacer} results in a decrease of B_{res}, which is well explained in regard to the dipolar coupling between the MNPs. Furthermore, an enlarged linewidth for particles with $d_{\mathrm{MNP}} = 18$ nm is observed compared to the two smaller nanoparticle sizes of $d_{\mathrm{MNP}} = 14$ nm and $d_{\mathrm{MNP}} = 9$ nm, which show approximately the same linewidth. In order to interpret these findings, theoretical simulations are performed highlighting distinct discrepancies between the theoretical modeling and the experimental findings when assuming the bulk material parameters for the MNPs. A systematic variation of the magnetization and magnetocrystalline anisotropy constant in the simulations and a subsequent comparison with the experiments indicate that the associated material parameters of the MNPs are effectively reduced with respect to their bulk counterpart, which is in good agreement with previous investigation found in the literature [54, 115].

The samples for this publication have been fabricated by Y. Wang. The experimental characterization and the theoretical modelings have been performed by N. Neugebauer. In addition, the contribution of all other authors must be emphasized, without whose commitment to the interpretation of the experimental spectra against the background of the theoretical findings would not have been possible.

PHYSICAL REVIEW B **107**, 184410 (2023)

Distance and size dependence of the interactions within highly ordered magnetic nanoparticle mesocrystals

Nils Neugebauer,[1,2,*] Yi Wang,[3] Matthias T. Elm,[1,2,4] Detlev M. Hofmann,[1,2] Christian Heiliger,[2,5]
Xingchen Ye,[3] and Peter J. Klar[1,2]
[1]*Institute of Experimental Physics I, Justus Liebig University, Heinrich-Buff-Ring 16, 35392 Giessen, Germany*
[2]*Center for Materials Research (ZfM/LaMa), Justus Liebig University, Heinrich-Buff-Ring 16, 35392 Giessen, Germany*
[3]*Department of Chemistry, Indiana University, Bloomington, Indiana 47405, USA*
[4]*Institute of Physical Chemistry, Justus Liebig University, Heinrich-Buff-Ring 17, 35392 Giessen, Germany*
[5]*Institute for Theoretical Physics, Justus Liebig University, Heinrich-Buff-Ring 16, 35392 Giessen, Germany*

(Received 12 April 2022; revised 9 January 2023; accepted 17 April 2023; published 5 May 2023)

Arranging magnetic nanoparticles (MNPs) into highly ordered structures, so-called superlattices or mesocrystals, is of great interest from a fundamental point of view, as the employment of the corresponding coupled nanoentities introduces additional degrees of freedom to manipulate the overall magnetic characteristics of such hierarchical materials. Characterizing the associated magnetic interactions on the mesoscopic scale is indispensable for obtaining a profound understanding of the relative strengths of the types of interactions involved, such as dipole-dipole interactions, which affect the collective response of a corresponding mesocrystal. In this paper, nanoparticles are deposited onto silicon substrates by spin coating, leading to two-dimensional monolayered structures showing a close-packed hexagonal arrangement. The MNPs consist of iron oxide (magnetite Fe_3O_4) and are coated with a nonmagnetic polymer (polystyrene). The MNPs are synthesized such that their diameters d_{MNP} are tuned in a range between 9 and 18 nm. A precise manipulation of the shell thickness d_{shell} is achieved by coating the MNPs with polystyrene of different molecular weights. In this fashion, the spacing between the MNPs, $d_{\mathrm{spacer}} = 2d_{\mathrm{shell}}$, is varied in a range between 6 and 14 nm. Within the investigated d_{spacer} range, dipolar interactions govern the collective properties showing distinct distance-dependent characteristics. As d_{spacer} increases, the dipolar coupling strength between the MNPs decreases, as deduced from the spectral features of ferromagnetic resonance experiments. These observations are further corroborated by numerical simulations of the dynamic properties of appropriate model systems. A comparison of the experimental and theoretical findings shows that material parameters, such as the magnetization M_{MNP} and the magnetocrystalline anisotropy C_{MNP} of the MNPs, are reduced compared to their bulk values.

DOI: 10.1103/PhysRevB.107.184410

I. INTRODUCTION

When arranging nanometer-sized entities of a material of well-defined shape, size, geometry, and orientation into highly ordered, periodic structures, novel macroscopic properties may arise [1–8]. These properties are not present in the bulk material, since such nanoparticle arrangements not only exhibit high order on the atomic scale, but also on the next higher hierarchical level at the mesoscopic scale [9]. One class of these hierarchical structures are the so-called mesocrystals, which are composed of nanoparticles (NPs) arranged on a superlattice [10]. Thus, the properties of the whole NP arrangement are essentially governed by the NP's characteristics, their spatial arrangement on a lattice, and the interaction between the NPs. By arranging NPs into mesocrystals that extend over macroscopic scales, it is possible to fabricate materials whose properties are determined by atomic interactions tuned by confinement on the nanoscale and the interparticle coupling between them on the mesoscale. From a scientific point of view, such structures are of great interest as they offer knobs on different length scales for a precise tuning of the interactions in order to adjust the overall magnetic response according to the needs of an application. As the volume of the nanometer-sized entities that form the mesocrystal decreases, surface effects and exchange interactions become increasingly important, while the influence of dipole interactions decreases [11]. Furthermore, at sizes, which are comparable to or smaller than the typical interaction lengths in corresponding bulk materials, deviations of the associated material parameters may arise.

Magnetic mesocrystals are often called magnonic crystals, when the wavelength of a magnon (the quantized spin wave) is comparable to the periodicity of the mesocrystal. A variety of phenomena has been observed in one- [12–14] and two-dimensional magnonic crystals [13–19], such as the formation of magnonic bands with tunable band gaps that depend on the specific materials and geometries used [20]. Magnetic mesocrystals composed of magnetic nanoparticles (MNPs) are recently in the focus of interest for several reasons. First, the synthesis of MNPs has reached a level of precision which enables fabricating ensembles of well-defined MNPs with

---

[*] nils.neugebauer@physik.uni-giessen.de

narrow size distributions. Second, the employment of MNPs may offer the opportunity to extend the investigation of confined magnons to the third spatial dimension [13,20,21].

The dynamic magnetic properties of magnonic crystals are very sensitive to the underlying periodicity, because the properties of the nanoentities vary with their size on the nanoscale, while the interaction between them depends on their spacing. Experimental investigations concerning the size-dependent properties of MNPs in nonordered systems have been performed in the past, indicating that the interaction inside MNPs of a certain size is indeed dominated by exchange interactions [22,23]. Those authors interpreted their findings on the basis of excited spin waves inside the MNPs, which are very sensitive to the size of the MNPs. The impact of the MNP size on the spin waves has been investigated theoretically by a number of researchers [11,24,25].

As the collective properties of the mesocrystal arise from the mutual interaction between neighboring MNPs, the spacing between them also has a significant impact on the macroscopic properties [26–28]. A systematic characterization of distance-dependent interactions between MNPs, such as dipolar coupling, can be performed by varying the spacing between the MNPs in a controlled way and investigating the magnetic response associated with the collective dynamic properties of the mesocrystal as a whole. Most investigations of distance-dependent properties are performed by (zero-) field-cooled magnetization measurements on both ordered and randomly arranged MNP structures investigating the real part [direct current (dc)] of the susceptibility [29–33] or the very low imaginary part [alternating current (ac)] of the susceptibility [34]. Such studies only allow a characterization of the predominantly static properties of MNPs, e.g., of the saturation magnetization M_{MNP} of the MNPs, but dynamic properties such as the propagation of spin waves and the magnetocrystalline anisotropy C_{MNP} cannot be assessed. Dynamic properties are accessible, e.g., by ferromagnetic resonance (FMR) experiments where the excitation of the magnetic material by microwaves is tuned by an external magnetic field. So far, only a few studies have used FMR for analyzing the size- and spacing-dependent properties of MNPs and MNP ensembles [28,35,36].

The investigation presented in this paper contributes to a more profound understanding of the collective dynamic properties of magnetic mesocrystals focusing on the dipolar coupling between the MNPs. Mesocrystals of defined lattice constants $a_{\mathrm{meso}} = d_{\mathrm{MNP}} + d_{\mathrm{spacer}} = d_{\mathrm{MNP}} + 2d_{\mathrm{shell}}$ are investigated. For this purpose, MNPs with different MNP diameters d_{MNP} and shell thicknesses $d_{\mathrm{shell}} = d_{\mathrm{spacer}}/2$ are synthesized and arranged in close hexagonal monolayer packings. The dipolar interactions within such mesocrystals can be characterized by performing FMR experiments on a series of such samples where d_{MNP} and d_{spacer} are varied systematically. The experimental findings reveal a distinct dependence on both d_{MNP} and d_{spacer}. By comparing the spectral characteristics of the MNP mesocrystals with theoretical results obtained from appropriate model systems, it can be concluded that the magnetization M_{MNP} as well as the effective magnetocrystalline anisotropy C_{MNP} of the MNPs are significantly reduced compared with their bulk counterpart M_{bulk} and C_{bulk}. These effects are reflected in the values of the external magnetic field $B_{\mathrm{ext}}^{\mathrm{res}}$ at which the resonance occurs in the FMR spectrum and its linewidth σ. The systematic changes of the FMR spectrum on varying d_{MNP} and d_{spacer} can be correlated with the interparticle interactions by simulating the FMR spectrum based on an idealized model system of the mesocrystals.

TABLE I. Overview of the sample sets investigated. Each set has been synthesized with defined MNP diameter d_{MNP} and shell thicknesses d_{shell} yielding hexagonal mesocrystals with different lattice constants of the mesocrystal $a_{\mathrm{meso}} = d_{\mathrm{MNP}} + d_{\mathrm{spacer}} = d_{\mathrm{MNP}} + 2d_{\mathrm{shell}}$.

Sample set	No.	d_{MNP} (nm)	a_{meso} (nm)	d_{spacer} (nm)
1	1-1	9.0 ± 0.5	15.1 ± 0.9	6.1 ± 0.5
	1-2		16.1 ± 0.8	7.1 ± 0.4
	1-3		16.9 ± 1.8	7.9 ± 0.6
	1-4		19.9 ± 1.2	10.9 ± 0.6
	1-5		21.7 ± 1.0	12.7 ± 0.5
2	2-1	14.2 ± 0.9	20.3 ± 1.6	6.1 ± 0.8
	2-2		21.8 ± 1.6	7.6 ± 0.8
	2-3		22.7 ± 1.8	8.5 ± 0.9
	2-4		23.9 ± 2.4	9.7 ± 1.2
	2-5		25.7 ± 1.7	11.5 ± 0.9
3	3-1	18.2 ± 1.2	24.3 ± 1.3	6.1 ± 0.7
	3-2		27.5 ± 1.8	9.3 ± 0.9
	3-3		28.5 ± 2.2	10.3 ± 1.1
	3-4		29.9 ± 2.4	11.7 ± 1.2
	3-5		33.1 ± 2.8	14.9 ± 1.4

II. METHODS

A. Sample preparation

The magnetic nanoparticles that form the mesocrystal consist of magnetite (Fe_3O_4) synthesized according to the method reported previously [37,38]. Three sample sets with MNP diameters of $d_{\mathrm{MNP}} = 9.0$, 14.2, and 18.2 nm have been synthesized. Polystyrene of different molecular weight was used as a surface surfactant. The molecular weight determines the thickness of the surface surfactant shell d_{shell} and thus the spacing between the surfaces of adjacent MNPs, i.e., $d_{\mathrm{spacer}} = 2d_{\mathrm{shell}}$, in ordered hexagonal monolayer mesocrystals [37–40]. The particles have been dispersed in toluene with an appropriate particle concentration in order to ensure a homogeneous monolayer coverage of the high-resistivity (100) Si substrate after deposition by spin coating at 1500 rpm for 45 s. The labeling of the individual samples consists of two digits, where the first digit (1–3) represents the sample set and the second (1–5) is associated with the spacer thickness as given in Table I.

Figure 1 shows a scanning electron microscope (SEM) image of MNPs of sample 3-2 together with its two-dimensional (2D) Fourier transform as inset underlining the high degree of order of the mesocrystal's nanoentities. The lattice constant of the mesocrystal a_{meso} as well as the distance between the MNPs d_{spacer} is extracted from the 2D Fourier transform by measuring the distance of the reflexes associated with the superlattice with respect to the central reflex. The extracted parameters as well as the diameter of the MNPs of each sample are summarized in Table I. All samples show a close-packed arrangement of MNPs extending up to the edges of

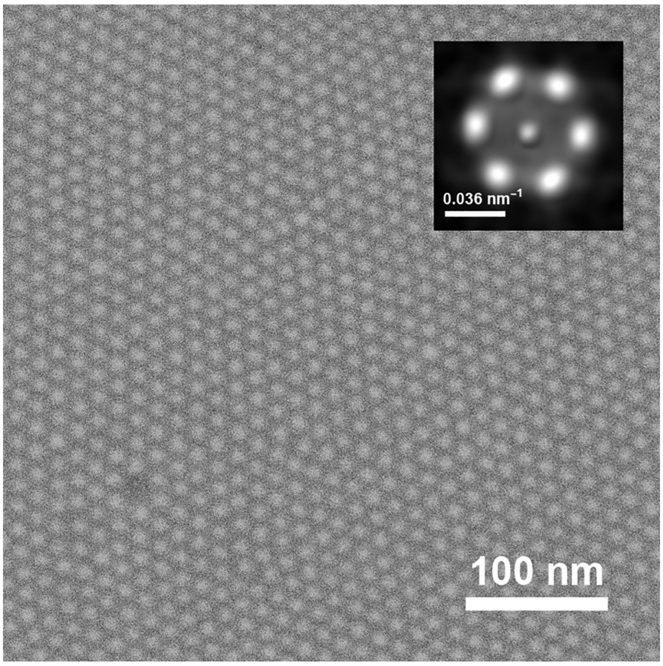

FIG. 1. SEM image of a MNP monolayer deposited by spin coating with appropriate particle concentrations and rotation speed. Inset: Corresponding Fourier transform of the SEM image, confirming the high quality of the mesocrystal and its hexagonal order.

the substrate and showing homogeneous monolayer coverage throughout, except for individually displaced MNPs. No bilayers are observed. The typical domain size of hexagonal close-packings of MNPs is 1–2 μm for all samples.

B. Ferromagnetic resonance setup

FMR experiments have been performed at room temperature using a Bruker ESP 300E spectrometer at X-band frequencies (≈9.8 GHz). Good signal intensities are achieved by mounting the samples such that both the vector of the external static magnetic field $\vec{B}_{\rm ext}$ (pointing in the x direction) and the vector of the external excitation field caused by the microwave $\vec{B}_\omega$ (pointing in the z direction) lie in the sample plane. This configuration yields optimal coupling of the microwave field with the sample, since the collective oscillations are excited in the direction of the magnetic easy axis of the thin film [41].

C. Theoretical modeling approach

Simulations of the magnetic response of the sample structures using an appropriate model system are a powerful tool for evaluating and interpreting the experimental findings. We use software based on a numerical integration of the equation of motion of each magnetic moment to simulate the associated absorption spectra (corresponding to an integrated ferromagnetic resonance spectrum) of different mesocrystals. For details of the employed program code, we refer the reader to our previous publications [42,43]. Here, we consider the dipole interaction and the magnetocrystalline anisotropy only, as the collective properties of MNP mesocrystals are predominantly determined by these interactions [44–46]. In principle, surface anisotropy effects may also have an impact on the overall characteristics. However, they play only a minor role in our samples due to the following reasons. (1) Its net contribution to the total anisotropy vanishes due to the highly spherical shape of the MNPs [47,48]. (2) The surface anisotropy only affects exchange resonance modes, but not the uniform Kittel mode, which is probed in this work [11]. (3) The strong exchange interaction across misfit dislocations within the MNPs superimposes potential surface effects [49].

Using the following simulation parameters as a starting point to describe magnetite (Fe_3O_4), the magnetization is $M_{\rm MNP} = M_{\rm bulk} = 4.8 \times 10^5$ A/m, the magnetocrystalline anisotropy constant $C_{\rm MNP} = C_{\rm bulk} = -1.1 \times 10^4$ J/m^3, and the empirical intrinsic damping parameter $\alpha = 0.01$ are set to those reported for the bulk material [50]. Calculating the corresponding energies for the dipole-dipole interaction $E_{\rm dd}$ and magnetocrystalline anisotropy $E_{\rm aniso}$, it follows that $E_{\rm aniso}/E_{\rm dd}$ ranges between 0.4 and 2.5 for the investigated samples. These values are well below the critical value of ≈100 for collective behavior to occur [44,46]. Thus, in conjunction with previous investigations [45], the properties of the investigated MNP assembly are essentially collective and of a dipolar nature. A discussion of the above-mentioned simplification about the simulation approach and additional considerations about the collective behavior are given in the Supplemental Material [51]. Since we observe deviations between the theoretical modeling using the bulk material parameters and the experimental findings, the magnetization and anisotropy constant for the MNPs $M_{\rm MNP}$ and $C_{\rm MNP}$ are varied systematically between 1/8 and 1 of the bulk value in order to obtain the best agreement with the experimental FMR spectra.

To model 2D MNP monolayers, each MNP is represented by an individual point dipole. These point dipoles with a magnetic moment proportional to the MNP volume are arranged in an infinitely extended monolayer of hexagonal order with the lattice constant $a_{\rm meso}$ reflecting the periodicity of the mesocrystal. Assuming an infinitely extended thin film, the force resulting from the external magnetic field and the dipolar interactions between MNPs acting on an individual dipole is the same for all dipoles. Thus, also the time evolution of a magnetic moment $\vec{m}(\vec{r}, t)$ (where $\vec{r}$ denotes the position vector and t the time) is the same for all dipoles (i.e., MNPs). Therefore, it is sufficient to simulate the oscillation of a single point dipole at the origin and to extrapolate its precessional motion $\vec{m}_0(\vec{r}_0, t)$ to the surrounding point dipoles $\vec{m}_i(\vec{r}_i, t)$. The dipole field caused by the surrounding magnetic moments $\vec{m}_i(\vec{r}_i, t)$ acting on the magnetic moment at the origin $\vec{m}_0(\vec{r}_0, t)$ is then calculated in each time step using the corresponding position vectors $\vec{r}_i$ of all surrounding magnetic moments and their extrapolated orientations $\vec{m}_i(\vec{r}_i, t) = \vec{m}_0(\vec{r}_0, t)$. As the dipole-dipole interaction decays with $1/r^3$ (where r denotes the distance between two dipoles), the associated magnetic dipole field $B_{\rm dd}$ caused by the surrounding MNPs converges for $r \rightarrow \infty$ in a 2D system, which allows a truncation of the interaction at a radius $R_{\rm max}$. The corresponding radius used for the simulations presented here is $R_{\rm max} = 10a_{\rm meso}$. A validation of this estimation along with an explanation of deriving the behavior of the surrounding point dipoles $\vec{m}_i(\vec{r}_i, t)$ from the time dependence of a central dipole $\vec{m}_0(\vec{r}_0, t)$ is given in the Supplemental Material [51]. Varying the spacing between the

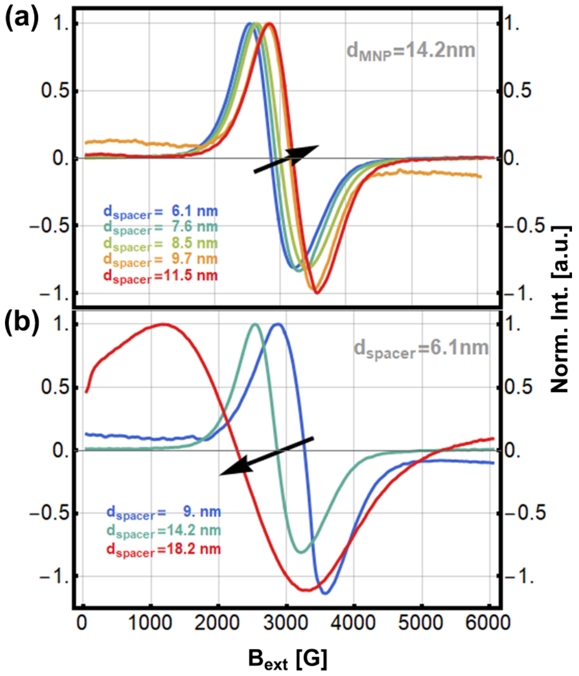

FIG. 2. (a) Measured FMR spectra of sample set 2 with MNP diameters d_{MNP} of 14.2 nm and spacing between the MNPs ranging from 6.1 to 11.5 nm. (b) Measured FMR spectra of sample S1-1, S2-1, and S3-1 with constant d_{spacer} of 6.1 nm and a variation of d_{MNP} of 9, 14.2, and 18.2 nm. The arrows indicate the changes of the resonance position $B_{\mathrm{ext}}^{\mathrm{res}}$ with increasing d_{spacer} and d_{MNP} in the top and bottom graph, respectively.

point dipoles and analyzing its impact on the spectral features provides insight into the distance-dependent collective properties of the mesocrystal.

III. RESULTS

A. FMR experimental results

Figure 2(a) shows five typical FMR spectra obtained from sample set 2. All mesocrystals consist of MNPs with a diameter d_{MNP} of 14.2 nm. The spacing d_{spacer} between the MNPs varies from 6.1 to 11.5 nm throughout the series. Figure 2(b) depicts FMR spectra of three MNP arrangements with particle sizes d_{MNP} ranging from 9 to 18.2 nm, while keeping d_{spacer} constant at 6.1 nm. The arrows indicate the spectral changes that occur with increasing d_{spacer} and increasing d_{MNP} in Figs. 2(a) and 2(b), respectively. It is clearly visible that the spectral features depend on both d_{spacer} and d_{MNP}. Increasing d_{spacer} at constant d_{MNP} causes a shift to higher-field strengths of the external field $B_{\mathrm{ext}}^{\mathrm{res}}$, at which the resonance occurs. Keeping the spacing between the MNPs constant and increasing their size, a shift of $B_{\mathrm{ext}}^{\mathrm{res}}$ to lower-field strengths is observed. In addition, samples of set 3 with $d_{\mathrm{MNP}} = 18$ nm show a significantly larger linewidth σ of their FMR spectra compared to those of the samples with smaller MNP sizes of set 1 ($d_{\mathrm{MNP}} = 9$ nm) and 2 ($d_{\mathrm{MNP}} = 14$ nm), whose linewidths are approximately the same. In order to analyze the impact of d_{spacer} and d_{MNP} on the spectral features in more detail, all spectra are fitted with the derivative of a single Lorentzian curve, since only a single resonance is observed. Here we chose the following form,

$$L(B_{\mathrm{ext}}) = \frac{A_0}{\sqrt{4\sigma^2 B_{\mathrm{ext}}^2 + \left(B_{\mathrm{ext}}^{\mathrm{res}\,2} - B_{\mathrm{ext}}^2\right)^2}} \tag{1}$$

and thus

$$\frac{dL}{dB_{\mathrm{ext}}} = A_0 \frac{2B_{\mathrm{ext}}\left(B_{\mathrm{ext}}^{\mathrm{res}\,2} - B_{\mathrm{ext}}^2 - 2\sigma^2\right)}{\left[\left(B_{\mathrm{ext}}^2 - B_{\mathrm{ext}}^{\mathrm{res}\,2}\right)^2 + 4B_{\mathrm{ext}}^2\sigma^2\right]^{3/2}}, \tag{2}$$

where A_0 is the signal intensity, σ the linewidth, $B_{\mathrm{ext}}^{\mathrm{res}}$ the field strength at which the resonance occurs, and B_{ext} the external field strength.

The extracted spectral parameters for each sample, i.e., the intensity A_0, the linewidth σ^{expt}, and the resonance field $B_{\mathrm{ext}}^{\mathrm{res,expt}}$, are summarized in Fig. 3. The lattice constant of the mesocrystal, a_{meso}, is shown on the bottom abscissa and the corresponding distance between the MNPs, d_{spacer}, on the upper abscissa. The upper panels depict the dependence of the resonance fields $B_{\mathrm{ext}}^{\mathrm{res,expt}}$ on d_{spacer} for all three sample sets, while the lower panels show the dependence of the signal

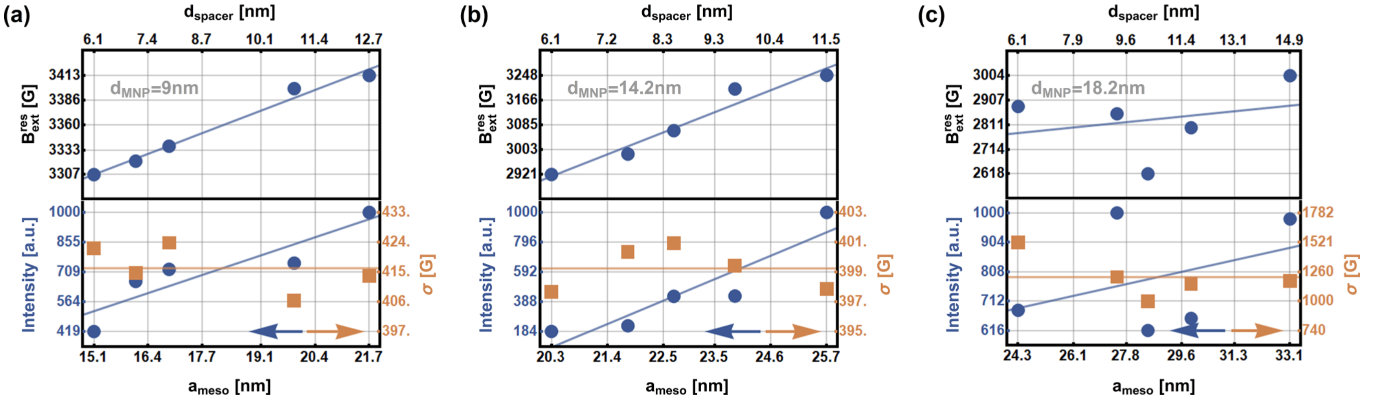

FIG. 3. Dependence of the experimentally observed resonance field $B_{\mathrm{ext}}^{\mathrm{res,expt}}$, the spectral linewidth σ^{expt}, and the FMR intensity on the spacing between the MNPs d_{spacer} for all three sample sets. Results from sample sets 1–3 are shown in (a)–(c), respectively. While the signal intensity and $B_{\mathrm{ext}}^{\mathrm{res,expt}}$ increase with increasing d_{spacer}, σ^{expt} decreases with increasing d_{spacer} for all sample sets. Colored arrows indicate the ordinate corresponding to data points of the same color. The colored straight lines are guides to the eye.

intensity (left ordinate) and the linewidth (right ordinate) on the spacing between the MNPs. The fitting confirms quantitatively the observation by visual analysis of Fig. 2 concerning the dependence on d_{spacer} for fixed d_{MNP}: (1) The experimentally observed resonance field $B_{\text{ext}}^{\text{res,expt}}$ increases with increasing d_{spacer}, (2) the signal intensity increases with increasing d_{spacer}, and (3) the linewidth σ^{expt} remains unchanged with increasing d_{spacer}. Furthermore, comparing the spectral features between the different sample sets, i.e., different d_{MNP}, two more characteristics are observed: (4) The linewidths of the FMR spectra of sample set 3 are significantly larger than those of the FMR spectra of sample sets 1 and 2 and (5) the resonance field $B_{\text{ext}}^{\text{res,expt}}$ decreases with increasing d_{MNP}.

First, we discuss the dependence of $B_{\text{ext}}^{\text{res,expt}}$ on d_{spacer}. $B_{\text{ext}}^{\text{res,expt}}$ is determined by the resonance condition following from the equation of motion, the Landau-Lifshitz-Gilbert equation [55]. Neglecting the damping term, Kittel has derived the resonance condition for a thin film [41]. As the demagnetizing tensor for a mesocrystal may be quite complex [56,57], but is very similar for all monolayer samples, we simplify the resonance condition as follows:

$$\begin{aligned}\frac{\omega_{\text{ext}}}{\gamma} &= \sqrt{B_{\text{tot}}(B_{\text{tot}} + \mu_0 M_{\text{film}})}\\ &= \sqrt{\left(B_{\text{ext}}^{\text{res}} + B_{\text{int}}\right)\left(B_{\text{ext}}^{\text{res}} + B_{\text{int}} + \mu_0 M_{\text{film}}\right)}\\ &\approx B_{\text{ext}}^{\text{res}} + B_{\text{dd}}. \end{aligned} \tag{3}$$

ω_{ext} is the angular excitation frequency of the external microwave source, γ is the gyromagnetic ratio of the MNPs, μ_0 the magnetic constant, $B_{\text{ext}}^{\text{res}}$ the external magnetic field at which the resonance occurs, B_{int} accounts for additional magnetic field contributions arising internally due to local magnetic interactions between the MNPs, and M_{film} the magnetization averaged over the entire film volume. Neglecting M_{film} is justified, since in the case of MNP monolayers, it is much smaller than the magnetization M_{MNP} of spherical particles comprising it. It scales with the ratio $d_{\text{MNP}}/d_{\text{spacer}}$ and the packing density of the MNPs. Thus, M_{film} is only ≈13% of M_{MNP} for sample 1-1 with $d_{\text{MNP}} = 9$ nm and $d_{\text{spacer}} = 6$ nm and $M_{\text{film}} \approx 4\%$ of M_{MNP} for sample 1-5 with the same MNP diameter but a larger spacing of $d_{\text{spacer}} = 12.7$ nm. B_{tot} is the magnetic field acting on the magnetic moment at resonance, which is a superposition of the external static field $B_{\text{ext}}^{\text{res}}$ and the local internal field B_{int}. This internal field contribution results mainly from the dominant dipolar interaction B_{dd} between neighboring MNPs and has a minor contribution of the magnetocrystalline anisotropy field within the individual MNPs. Due to the fixed excitation frequency ω_{ext} of the microwave, B_{tot} and thus also $B_{\text{ext}}^{\text{res}}$ are constant. Thus, d_{spacer}-dependent properties are predominantly governed by the characteristic $1/r^3$ dependence of B_{dd}, where r is the distance between the two dipoles. This implies that B_{dd} decreases with increasing spacer distance d_{spacer}. Consequently, the resonance fields deduced from the experiments $B_{\text{ext}}^{\text{res,expt}}$ must increase to fulfill the resonance condition [Eq. (3)]. From the upper panels of Fig. 3, it can be concluded that $B_{\text{ext}}^{\text{res,expt}}$ indeed increases with increasing d_{spacer} as this behavior is observed for all three sample sets.

Second, as the dipolar coupling decreases with increasing spacing d_{spacer}, demagnetization effects forcing the magnetic moments of the MNPs into the film plane become less significant, allowing them to oscillate with larger amplitudes and thus absorb more energy of the microwave field driving them externally. As a result, the intensity of the signal increases with increasing d_{spacer}.

Third, the internal damping of the precessional motion of the MNPs magnetization reflected by the linewidth parameter σ^{expt} does not depend on the spacing d_{spacer} between the MNPs. This suggests that the internal damping is primarily determined by the internal structure of the MNPs rather than by their mutual dipolar interaction.

Prior to analyzing the findings (4) and (5), it is necessary to discuss some general aspects of the particle synthesis. As the synthesis protocols of samples with different MNP diameters vary in terms of the reaction time and temperature [37,38], differences in the internal structure of the particles between the sample sets may occur due to different synthesis conditions. Previous investigations indicate that the magnetization of the MNPs is crucially affected by lattice imperfections within the MNPs [49]. In addition, as the size of the MNPs increases, different oxidation states of the iron ions may be observed [37], resulting in increased inhomogeneities that affect the internal damping of the magnetization oscillation.

Thus, fourth, when comparing the linewidths σ^{expt} of sample sets 1 and 2 with MNP diameters of $d_{\text{MNP}} = 9$ and 14 nm, it can be seen that σ^{expt} is approximately constant, suggesting that the degree of internal disorder within the MNPs of diameters ranging from $d_{\text{MNP}} = 9$ to 14 nm is quite similar. This is in good agreement with the only slightly higher synthesis temperature of 330 °C for $d_{\text{MNP}} = 14$ nm compared with 320 °C for $d_{\text{MNP}} = 9$ nm. Sample set 3 shows significantly wider lines, suggesting an increased internal damping. Taking into account that the degree of the MNP ordering is similar for all three sample sets, the significantly increased damping associated with a broader linewidth σ^{expt} for sample set 3 indicates that there is an increased internal disorder present within the MNPs of sample set 3 compared to those of sets 1 and 2. Whether the larger internal disorder of the MNPs with $d_{\text{MNP}} = 18$ nm is due to the even higher synthesis temperature of 350 °C is not clear.

Fifth, as the diameter d_{MNP} of the MNP increases, its total magnetic moment also increases as it is proportional to the MNP volume. Thus, the dipole field B_{dd} increases with increasing d_{MNP}, resulting in a decrease of $B_{\text{ext}}^{\text{res}}$ to fulfill the resonance condition [Eq. (3)] and the damping of the oscillation is expected to increase with increasing dipolar coupling [58].

B. Theoretical modeling results

The results of the theoretical simulations based on the bulk magnetization of magnetite and neglecting the magnetocrystalline anisotropy are shown in Fig. 4. The simulations are performed to obtain a better understanding of the impact of dipolar interaction on the spectral features of the FMR experiments of the mesocrystals. Figure 4(a) shows modeled absorption spectra (corresponding to an integrated FMR spectrum). The magnetic moment of each MNP corresponds to a

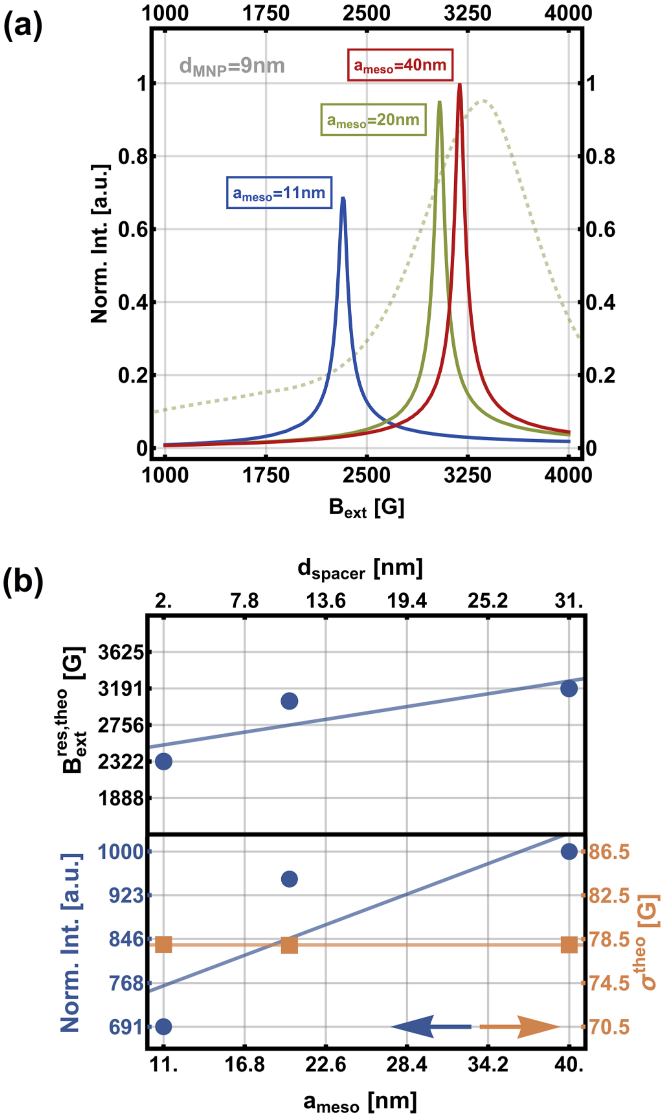

FIG. 4. (a) Measured absorption spectra (corresponding to an integrated FMR spectrum) of sample 1-4 (dashed green curve) and simulated absorption spectra (shown by continuous curves) of mesocrystals consisting of MNPs with a diameter of $d_{\mathrm{MNP}} = 9$ nm. Three different lattice constants are simulated ranging from $a_{\mathrm{meso}} = 11$ to 40 nm. (b) Corresponding line-shape parameters of the simulated spectra, such as the resonance field $B_{\mathrm{ext}}^{\mathrm{res,theo}}$, the linewidth σ^{theo}, and the intensity in dependence on the spacer distance d_{spacer}.

volume with a diameter of $d_{\mathrm{MNP}} = 9$ nm. The lattice constant of the mesocrystal is varied between $a_{\mathrm{meso}} = 11$ and 40 nm. The spectral parameters are extracted by fitting the calculated absorption spectra by single Lorentzian line shapes. In qualitative agreement with the experimental findings shown in Fig. 3, the extracted spectral parameters from the simulations depicted in Fig. 4(b) show that $B_{\mathrm{ext}}^{\mathrm{res,theo}}$ and the signal intensity increase with increasing d_{spacer}, while the linewidth σ^{theo} remains almost unchanged.

However, despite good qualitative agreement of the simulations with the experiments, quantitative deviations occur. For example, the comparison of the resonance field and linewidth obtained by experiment and theory for a 2D mesocrystal of MNPs with $d_{\mathrm{MNP}} = 9$ nm and $a_{\mathrm{meso}} = 20$ nm in Fig. 4(a) shows that the experimental spectrum (dashed green curve) is much broader than the simulated one (continuous green curve). In addition, the calculated resonance field is significantly lower than that deduced from the experiments. The same holds for all other samples. At first sight, a likely reason is the neglect of the magnetocrystalline anisotropy. However, as we will show in what follows this is not sufficient. In fact, it turns out that the material parameters, in particular of the values of the magnetization M_{MNP} and the magnetocrystalline anisotropy constant C_{MNP} of the MNPs, must be reduced with respect to the corresponding bulk values of magnetite in order to obtaining a satisfactory description of the experimental data. In order to adequately account for the magnetocrystalline anisotropy in the simulations, the random distribution of the crystal orientations of the MNPs with respect to the direction of the magnetic field has to be taken into account. For this purpose, a set of simulations with different orientations of B_{ext} with respect to the principal axis of the MNPs has been performed. In each simulation, all MNPs exhibit the same orientation of their principal axes. The resonance field $B_{\mathrm{ext}}^{\mathrm{res,theo}}$ and the linewidth σ^{theo} in the presence of a random distribution of orientations of the MNPs can be estimated by the mean value of all resonance fields and the corresponding standard deviation of such a set of calculations. Furthermore, the calculations were not only performed for the bulk values for the magnetization M_{bulk} and magnetocrystalline anisotropy C_{bulk}, but also varied systematically assuming pairs of parameters M_{MNP} and C_{MNP}.

Figure 5(a) shows the effective resonance fields $B_{\mathrm{ext}}^{\mathrm{res,theo}}$ and Fig. 5(b) the simulated effective linewidths σ^{theo} for a 2D mesocrystal of MNPs with $d_{\mathrm{MNP}} = 9$ nm and $d_{\mathrm{spacer}} = 11$ nm obtained by the simulations. The ratios $M_{\mathrm{MNP}}/M_{\mathrm{bulk}}$ and $C_{\mathrm{MNP}}/C_{\mathrm{bulk}}$ are both varied between 1/8 and 1. The values of $B_{\mathrm{ext}}^{\mathrm{res,theo}}$ and σ^{theo} are plotted in dependence on $M_{\mathrm{MNP}}/M_{\mathrm{bulk}}$ and $C_{\mathrm{MNP}}/C_{\mathrm{bulk}}$ in the form of relief plots in Figs. 5(a) and 5(b). Both $B_{\mathrm{ext}}^{\mathrm{res,theo}}$ and σ^{theo} vary in a wide range as a function of $M_{\mathrm{MNP}}/M_{\mathrm{bulk}}$ and $C_{\mathrm{MNP}}/C_{\mathrm{bulk}}$. The hatched regions in both relief plots indicate where the theoretical values are in agreement with typical experimental values, i.e., those of sample 1-4 [shown in Fig. 3(a)]. The widths of the hatched regions in Figs. 5(a) and 5(b) are defined by the uncertainties of the line-shape fitting of the experimental spectrum of sample 1-4. For both quantities, $B_{\mathrm{ext}}^{\mathrm{res,theo}}$ and σ^{theo}, there is a range of value pairs ($M_{\mathrm{MNP}}/M_{\mathrm{bulk}}$ and $C_{\mathrm{MNP}}/C_{\mathrm{bulk}}$) where the simulated values match the experiment, i.e., no decisive conclusion can be drawn from the individual relief plots. However, there is a much narrower parameter window of value pairs ($M_{\mathrm{MNP}}/M_{\mathrm{bulk}}$ and $C_{\mathrm{MNP}}/C_{\mathrm{bulk}}$) where agreement with both experimental values $B_{\mathrm{ext}}^{\mathrm{res,expt}}$ and σ^{expt} is achieved within the experimental uncertainties. This parameter window is depicted in Fig. 5(c) as the intersection of the two hatched regions of Figs. 5(a) and 5(b). It can be concluded that a good agreement with experiment is obtained when the magnetization M_{MNP} of the MNPs is reduced to approximately 40%–60% and the anisotropy constant C_{MNP} to approximately 30%–65% with respect to their bulk values.

Similar comparisons between experiment and simulations have been carried out for a sample of set 2 with $d_{\mathrm{MNP}} = 14$ nm and $d_{\mathrm{spacer}} = 11$ nm and for a sample of set 3 with $d_{\mathrm{MNP}} = 18$

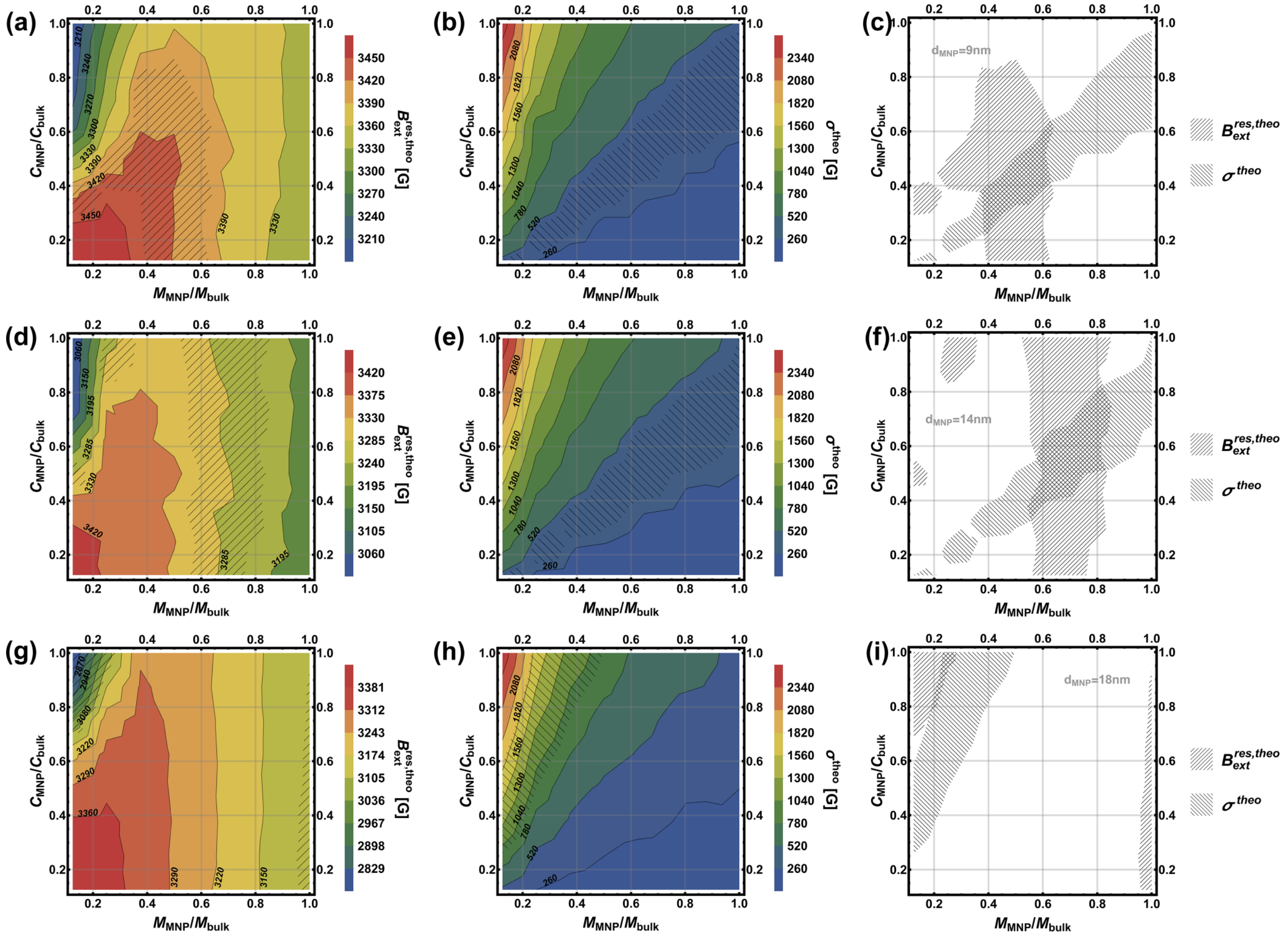

FIG. 5. (a) Effective resonance field $B_{\text{ext}}^{\text{res,theo}}$ for different pairs ($M_{\text{MNP}}, C_{\text{MNP}}$) of parameters for $d_{\text{MNP}} = 9$ nm. The magnetization $M_{\text{MNP}}/M_{\text{bulk}}$ is ranging from 1/8 to 1 and the anisotropy constant $C_{\text{MNP}}/C_{\text{bulk}}$ is ranging from 1/8 to 1. The hatched area corresponds to pairs ($M_{\text{MNP}}, C_{\text{MNP}}$), which are in concordance with the experimental findings shown in Fig. 3(a) for $d_{\text{MNP}} = 9$ nm. (b) Corresponding parameters for σ^{theo}. Again, the hatched area corresponds to pairs ($M_{\text{MNP}}, C_{\text{MNP}}$), which are in concordance with the experimental findings. (c) The intersection of the hatched areas of (a) and (b) enables an estimation of the reduced material parameters for the investigated MNPs of approximately 40%–60% for M_{MNP} and 30%–65% for C_{MNP} with respect to their bulk values. (d)–(f) depict the corresponding parameter variation of M_{MNP} and C_{MNP} for $d_{\text{MNP}} = 14$ nm, indicating a reduction of approximately 55%–85% for M_{MNP} and 35%–80% for C_{MNP} with respect to the bulk. (g)–(i) depict the parameter variation for particles with $d_{\text{MNP}} = 18$ nm.

nm and $d_{\text{spacer}} = 11$ nm. The results of the former comparison are given in Figs. 5(d)–5(f) and those of the latter in Figs. 5(g)–5(i).

In the case of the sample of set 2 with $d_{\text{MNP}} = 14$ nm, we also find a reduction of M_{MNP} and C_{MNP}, but not as pronounced as observed for the sample of set 1 with $d_{\text{MNP}} = 9$ nm. Best agreement is obtained for a magnetization ratio $M_{\text{MNP}}/M_{\text{bulk}}$ of approximately 55%–85% and of $C_{\text{MNP}}/C_{\text{bulk}}$ of about 35%–80%.

In the case of the sample of set 3 with $d_{\text{MNP}} = 18$ nm, the best agreement is obtained for a magnetization ratio $M_{\text{MNP}}/M_{\text{bulk}}$ of approximately 20%–30% and of $C_{\text{MNP}}/C_{\text{bulk}}$ of about 80%–100%. Although a reduction of both $M_{\text{MNP}}/M_{\text{bulk}}$ and $C_{\text{MNP}}/C_{\text{bulk}}$ is somewhat expected even in ideal structures, since atoms close to the surface of the MNPs are expected to behave differently than atoms close to the center of the MNP as the surface-to-volume ratio is size dependent, the results are at first sight surprising. In ideal structures, both parameters M_{MNP} and C_{MNP} must approach the corresponding bulk values with increasing d_{MNP} and the ratios $M_{\text{MNP}}/M_{\text{bulk}}$ and $C_{\text{MNP}}/C_{\text{bulk}}$ should approach 1 and not decrease again as observed for the 18 nm MNPs. Thus, the observed behavior of $M_{\text{MNP}}/M_{\text{bulk}}$ and $C_{\text{MNP}}/C_{\text{bulk}}$ must reflect structural defects. For example, it is suggested in Ref. [49] that misfit dislocations within the individual MNPs may cause a reduction of M_{MNP} with respect to M_{bulk}.

The investigations presented here not only reproduce the findings of Ref. [49] for $d_{\text{MNP}} = 9$ nm, but also provide additional insight into the dependence of the parameters M_{MNP} and C_{MNP} on the particle diameter d_{MNP} and deviations from structural ideality. A detailed consideration of the effect of the variation of the surface-to-volume ratio as a function of particle diameter d_{MNP} in ideal structures is given in the Supplemental Material [51]. The results for M_{MNP} and C_{MNP} for the samples with $d_{\text{MNP}} = 9$ nm (set 1) and $d_{\text{MNP}} = 14$ nm (set 2) are in good agreement with the anticipated dependence on the surface-to-volume ratio, whereas the values for the MNPs with $d_{\mathrm{MNP}} = 18$ nm (set 3) strongly deviate from the expectation. The observed deviations for MNPs with $d_{\mathrm{MNP}} = 18$ nm strongly suggest increased structural differences compared with MNPs of a smaller diameter. Unfortunately, we cannot clarify the origin of the lower structural quality of the samples prepared from MNPs with diameters $d_{\mathrm{MNP}} > 14$ nm. Possible reasons are a higher fraction of MNPs with misfit dislocations, more point defects, i.e., iron ions of other oxidation states [37], or the onset of magnetic domain formation within the MNPs. However, we can state that accounting for dipolar interactions between the MNPs, magnetocrystalline anisotropy, and surface-to-volume ratio effects in the modeling gives a good description of ordered MNP monolayers for $d_{\mathrm{MNP}} \leqslant 14$ nm, but is not sufficient for MNP monolayers with $d_{\mathrm{MNP}} \geqslant 18$ nm.

IV. CONCLUSION

In summary, our results show that magnetic nanoparticles deposited into highly ordered mesocrystals exhibit a distinct dependence of their collective magnetic properties on the size of the magnetic nanoparticles and the spacing between them. This confirms that the dipolar coupling between the nanoentities on the mesoscopic scale has an impact on the macroscopic dynamic properties of the whole mesocrystalline film. Performing simulations, in which point dipoles represent the MNPs, confirm the experimental findings. Such studies carefully conducted, from both the experimental and theoretical points of view, provide insight into deviations from the material parameters in nanoparticles with respect to the corresponding bulk material. Such studies are helpful for evaluating the internal structural quality of the employed magnetic nanoparticles and their spacing-dependent interactions and constitute important steps towards the fabrication of 3D mesocrystals out of MNPs. In particular, this holds for MNPs with $d_{\mathrm{MNP}} \leqslant 14$ nm, which only exhibit moderate effects of disorder induced by dislocations and grain boundaries. Thus, FMR in conjunction with micromagnetic simulations proves to be a powerful tool for the evaluation of MNP mesocrystals and shows distinct advantages compared to other (dc) techniques.

ACKNOWLEDGMENTS

We are grateful for funding in the frame of the ERDF innovation laboratory “High performance materials.” We acknowledge computational resources provided by the HPC Core Facility and the HRZ of the Justus-Liebig-University Giessen. Y.W. and X.Y. were supported by the U.S. National Science Foundation (NSF DMR-2102526). In addition, the authors thank Marcel Giar and Philipp Risius (HPC Core Facility, Justus Liebig University Giessen) for their administrative support.

---

[1] D. V. Talapin, E. V. Shevchenko, M. I. Bodnarchuk, X. Ye, J. Chen, and C. B. Murray, Quasicrystalline order in self-assembled binary nanoparticle superlattices, Nature (London) **461**, 964 (2009).

[2] J. Chen, X. Ye, S. J. Oh, J. M. Kikkawa, C. R. Kagan, and C. B. Murray, Bistable magnetoresistance switching binary nanocrystal superlattices by in exchange-coupled $CoFe_2O_4$-Fe_3O_4 self-assembly and thermal annealing, ACS Nano **7**, 1478 (2013).

[3] J. Chen, A. Dong, J. Cai, X. Ye, Y. Kang, J. M. Kikkawa, and C. B. Murray, Collective dipolar interactions in self-assembled magnetic binary nanocrystal superlattice membranes, Nano Lett. **10**, 5103 (2010).

[4] D. C. Reifsnyder, X. Ye, T. R. Gordon, C. Song, and C. B. Murray, Three-dimensional self-assembly of chalcopyrite copper indium diselenide nanocrystals into ordered films, ACS Nano **7**, 4307 (2013).

[5] S. Jeong, Y. Liu, Y. Zhong, X. Zhan, Y. Li, Y. Wang, P. M. Cha, J. Chen, and X. Ye, Heterometallic seed-mediated growth of monodisperse colloidal copper nanorods with widely tunable plasmonic resonances, Nano Lett. **20**, 7263 (2020).

[6] X. Ye, J. Chen, B. T. Diroll, and C. B. Murray, Tunable plasmonic coupling in self-assembled binary nanocrystal superlattices studied by correlated optical microspectrophotometry and electron microscopy, Nano Lett. **13**, 1291 (2013).

[7] Y. Liu, Y. Li, S. Jeong, Y. Wang, and X. Ye, Colloidal synthesis of nanohelices via bilayer lattice misfit, J. Am. Chem. Soc. **142**, 12777 (2020).

[8] Y. Wang, J. Chen, Y. Zhong, S. Jeong, R. Li, and X. Ye, Structural diversity in dimension-controlled assemblies of tetrahedral gold nanocrystals, J. Am. Chem. Soc. **144**, 13538 (2022).

[9] A. Fabian, M. T. Elm, D. M. Hofmann, and P. J. Klar, Hierarchical structures of magnetic nanoparticles for controlling magnetic interactions on three different length scales, J. Appl. Phys. **121**, 224303 (2017).

[10] R.-Q. Song and H. Coelfen, Mesocrystals-ordered nanoparticle superstructures, Adv. Mater. **22**, 1301 (2010).

[11] A. Aharoni, Effect of surface anisotropy on the exchange resonance modes, J. Appl. Phys. **81**, 830 (1997).

[12] Z. K. Wang, V. L. Zhang, H. S. Lim, S. C. Ng, M. H. Kuok, S. Jain, and A. O. Adeyeye, Observation of frequency band gaps in a one-dimensional nanostructured magnonic crystal, Appl. Phys. Lett. **94**, 083112 (2009).

[13] M. Krawczyk and D. Grundler, Review and prospects of magnonic crystals and devices with reprogrammable band structure, J. Phys.: Condens. Matter **26**, 123202 (2014).

[14] G. Gubbiotti, S. Tacchi, M. Madami, G. Carlotti, A. O. Adeyeye, and M. Kostylev, Brillouin light scattering studies of planar metallic magnonic crystals, J. Phys. D: Appl. Phys. **43**, 264003 (2010).

[15] S. Tacchi, G. Gubbinotti, M. Madami, and G. Carlotti, Brillouin light scattering studies of 2D magnonic crystals, J. Phys.: Condens. Matter **29**, 073001 (2017).

[16] S. Tacchi, G. Duerr, J. W. Klos, M. Madami, S. Neusser, G. Gubbiotti, M. Krawczyk, and D. Grundler, Forbidden Band Gaps in the Spin-Wave Spectrum of a Two-Dimensional Bicomponent Magnonic Crystal, Phys. Rev. Lett. **109**, 137202 (2012).

[17] F. Montoncello, S. Tacchi, L. Giovannini, M. Madami, G. Gubbiotti, G. Carlotti, E. Sirotkin, E. Ahmad, F. Y. Ogrin, and V. V. Kruglyak, Asymmetry of spin wave dispersions in

a hexagonal magnonic crystal, Appl. Phys. Lett. **102**, 202411 (2013).

[18] C. Van Opdenbosch, G. Hukic-Markosian, S. Ott, C. Abert, and M. H. Bartl, An experiment-based numerical treatment of spin wave modes in periodically porous materials, Phys. Status Solidi B **257**, 1900296 (2020).

[19] N. Ross, M. Kostylev, and R. L. Stamps, Standing spin-wave mode structure and linewidth in partially disordered hexagonal arrays of perpendicularly magnetized sub-micron permalloy discs, J. Appl. Phys. **116**, 113909 (2014).

[20] M. Krawczyk and H. Puszkarski, Plane-wave theory of three-dimensional magnonic crystals, Phys. Rev. B **77**, 054437 (2008).

[21] S. Mamica, M. Krawczyk, M. L. Sokolovskyy, and J. Romero-Vivas, Large magnonic band gaps and spectra evolution in three-dimensional magnonic crystals based on magnetoferritin nanoparticles, Phys. Rev. B **86**, 144402 (2012).

[22] P. Toneguzzo, O. Acher, G. Viau, F. Fievet-Vincent, and F. Fievet, Observations of exchange resonance modes on submicrometer sized ferromagnetic particles, J. Appl. Phys. **81**, 5546 (1997).

[23] P. Toneguzzo, G. Viau, O. Acher, F. Fievet-Vincent, and F. Fievet, Monodisperse ferromagnetic particles for microwave applications, Adv. Mater. **10**, 1032 (1998).

[24] P. A. Voltairas and C. V. Massalas, Size-dependent resonance modes in ferromagnetic spheres, J. Magn. Magn. Mater. **124**, 20 (1993).

[25] R. Arias, P. Chu, and D. L. Mills, Dipole exchange spin waves and microwave response of ferromagnetic spheres, Phys. Rev. B **71**, 224410 (2005).

[26] R. Arias and D. L. Mills, Theory of collective spin-wave modes of interacting ferromagnetic spheres, Phys. Rev. B **70**, 104425 (2004).

[27] L. Giovannini, F. Montoncello, and F. Nizzoli, Effect of interdot coupling on spin-wave modes in nanoparticle arrays, Phys. Rev. B **75**, 024416 (2007).

[28] C. Mitsumata, S. Tomita, M. Hagiwara, and K. Akamatsu, Electron magnetic resonance in interacting ferromagnetic-metal nanoparticle systems: Experiment and numerical simulation, J. Phys.: Condens. Matter **22**, 016005 (2010).

[29] P. C. Rivas Rojas, P. Tancredi, O. Moscoso Londono, M. Knobel, and L. M. Socolovsky, Tuning dipolar magnetic interactions by controlling individual silicacoating of iron oxide nanoparticles, J. Magn. Magn. Mater. **451**, 688 (2018).

[30] R. Voggu, N. Kumar, and C. N. R. Rao, Dependence of the properties of magnetic nanoparticles on the interparticle separation, J. Phys. Chem. C **112**, 17775 (2008).

[31] C. Moya, O. Iglesias, X. Battle, and A. Labarta, Quantification of Dipolar Interactions in $Fe_{3-x}O_4$ Nanoparticles, J. Phys. Chem. C **119**, 24142 (2015).

[32] B. L. Frankamp, A. K. Boal, M. T. Tuominen, and V. M. Rotello, Direct control of the magnetic interaction between iron oxide nanoparticles through dendrimer-mediated self-assembly, J. Am. Chem. Soc. **127**, 9731 (2005).

[33] G. C. Papaefthymiou, E. Devlin, A. Simopoulos, D. K. Yi, S. N. Riduan, S. S. Lee, and J. Y. Ying, Interparticle interactions in magnetic core/shell nanoarchitectures, Phys. Rev. B **80**, 024406 (2009).

[34] S. Fleutot, G. L. Nealon, M. Pauly, B. P. Pichon, C. Leuvrey, M. Dillon, J. L. Gallani, D. Guillon, B. Donnio, and S. Begin-Colin, Spacing-dependent dipolar interactions in dendronized magnetic iron oxide nanoparticle 2D arrays and powders, Nanoscale **5**, 1507 (2013).

[35] S. Jung, L. DeLong, J. B. Ketterson, and V. Chandrasekhar, Ferromagnetic resonance in periodic particle arrays, Phys. Rev. B **66**, 132401 (2002).

[36] O. N. Martyanov, D. A. Balaev, O. V. Pylypenko, L. V. Odnodvorets, S. V. Chernov, S. A. Nepijko, H. J. Elmers, C. M. Schneider, and G. Schönhense, FMR investigations of two-dimensional periodic arrays of disc-shaped Co particles at different temperatures, J. Supercond. Novel Magn. **28**, 3587 (2015).

[37] J. Park, K. An, Y. Hwang, J. G. Park, H. J. Noh, J. Y. Kim, J. H. Park, N. M. Hwang, and T. Hyeon, Ultra-large-scale syntheses of monodisperse nanocrystal, Nat. Mater. **3**, 891 (2004).

[38] Y. Wang, J. Chen, C. Zhu, B. Zhu, S. Jeong, Y. Yi, Y. Liu, J. Fiadorwu, and X. Ye, Kinetically controlled self-assembly of binary polymer-grafted nanocrystals into ordered superstructures via solvent vapor annealing, Nano Lett. **21**, 5053 (2021).

[39] Y. Liu, M. Klement, Y. Wang, Y. Zhong, B. Zhu, J. Chen, M. Engel, and X. Ye, Macromolecular ligand engineering for programmable nanoprism assembly, J. Am. Chem. Soc. **143**, 16163 (2021).

[40] X. Ye, C. Zhu, P. Ercius, S. N. Raja, B. He, M. R. Jones, M. R. Hauwiller, Y. Liu, T. Xu, and A. P. Alivisatos, Structural diversity in binary superlattices self-assembled from polymer-grafted nanocrystals, Nat. Commun. **6**, 10052 (2015).

[41] C. Kittel, On the theory of ferromagnetic resonance absorption, Phys. Rev. **73**, 155 (1948).

[42] N. Neugebauer, A. Fabian, M. T. Elm, D. M. Hofmann, M. Czerner, C. Heiliger, and P. J. Klar, Investigation of the dipole interaction in and between ordered arrangements of magnetic nanoparticles, Phys. Rev. B **101**, 104409 (2020).

[43] N. Neugebauer, T. Hache, M. T. Elm, D. M. Hofmann, C. Heiliger, H. Schultheiss, and P. J. Klar, Frequency- and magnetic-field-dependent properties of ordered magnetic nanoparticle arrangements, Phys. Rev. B **103**, 094438 (2021).

[44] E. H. Sanchez, M. Vasilakaki, S. Seong Lee, P. S. Normile, M. S. Andersson, R. Mathieu, A. Lopez-Ortega, B. P. Pichon, D. Peddis, C. Binns, P. Nordblad, K. Trohidou, J. Nogues, and J. A. De Toro, Crossover from individual to collective magnetism in dense nanoparticle systems: Local anisotropy versus dipolar interactions, Small **18**, 2106762 (2022).

[45] J. A. De Toro, M. Vasilakaki, S. Seong Lee, M. S. Andersson, P. S. Normile, N. Yaacoub, P. Murray, E. H. Saanchez, P. Muniz, D. Peddis, R. Mathieu, K. Liu, J. Geshev, K. N. Trohidou, and J. Nogues, Remanence plots as a probe of spin disorder in magnetic nanoparticles, Chem. Mater. **29**, 8258 (2017).

[46] S Mørup, Superparamagnetism and spin glass ordering in magnetic nanocomposites, Europhys. Lett. **28**, 671 (1994).

[47] F. Bødker, S. Morup, and S. Linderoth, Surface Effects in Metallic Iron Nanoparticles, Phys. Rev. Lett. **72**, 282 (1994).

[48] E. Lima, A. L. Brandl, A. D. Arelaro, and G. F. Goyaa, Spin disorder and magnetic anisotropy in Fe_3O_4 nanoparticles, J. Appl. Phys. **99**, 083908 (2006).

[49] Z. Nedelkoski, D. Kepaptsoglou, L. Lari, T. Wen, R. A. Booth, S. D. Oberdick, P. L. Galindo, Q. M. Ramasse, R. F. L. Evans, S. Majetich, and V. K. Lazarov, Origin of reduced magnetization and domain formation in small magnetite nanoparticles, Sci. Rep. **7**, 45997 (2017).

[50] B. W. Zingsem, T. Feggeler, A. Terwey, S. Ghaisari, D. Spoddig, D. Faivre, R. Meckenstock, M. Farle, and M. Winklhofer, Biologically encoded magnonics, Nat. Commun. **10**, 4345 (2019).

[51] See Supplemental Material at http://link.aps.org/supplemental/10.1103/PhysRevB.107.184410 for the theoretical basis of the simulation approach used to model idealized mesocrystals, a discussion of individual versus collective behavior of MNP mesocrystals, the average film magnetization, and the dependence of the surface-to-volume ratio of the individual MNPs, which includes Refs. [41–43,50,52–55].

[52] J. M. D. Coey, *Magnetism and Magnetic Materials* (Cambridge University Press, Cambridge, U.K., 2010).

[53] A. Vansteenkiste, J. Leliaert, M. Dvornik, M. Helsen, F. Garcia-Sanchez, and B. van Waeyenberge, The design and verification of MuMax3, AIP Adv. **4**, 107133 (2014).

[54] L. Shampine and M. Gordon, *Computer Solution of Ordinary Differential Equations: The Initial Value Problem* (Freeman, San Francisco, 1975).

[55] R. F. L. Evans, W. J. Fan, P. Chureemart, T. A. Ostler, M. O. A. Ellis, and R. W. Chantrell, Atomistic spin model simulations of magnetic nanomaterials, J. Phys.: Condens. Matter **26**, 103202 (2014).

[56] J. Kaczer and L. Murtinova, On the demagnetizing energy of periodic magnetic distributions, Phys. Status Solidi A **23**, 79 (1974).

[57] H. How and C. Vittoria, Demagnetization energy and magnetic permeability tensor of spheroidal magnetic particles dispersed in cubic lattices, Phys. Rev. B **43**, 8094 (1991).

[58] C. Mitsumata and S. Tomita, Control of Gilbert damping using magnetic metamaterials, Phys. Rev. B **84**, 174421 (2011).

Supplementary Information

Distance and size dependence of the interactions within highly ordered magnetic nanoparticle mesocrystals

Nils Neugebauer,[1,2,a)] Yi Wang,[3] Matthias T. Elm,[1,2,4] Detlev M. Hofmann,[1,2] Christian Heiliger,[2,5] Xingchen Ye,[3] and Peter J. Klar[1,2]
[1)] *Institute of Experimental Physics I, Justus Liebig University, Heinrich-Buff-Ring 16, 35392 Giessen, Germany*
[2)] *Center for Materials Research (ZfM/LaMa), Justus Liebig University, Heinrich-Buff-Ring 16, 35392 Giessen, Germany*
[3)] *Department of Chemistry, Indiana University, Bloomington, 47405 Indiana, United States*
[4)] *Institute of Physical Chemistry, Justus Liebig University, Heinrich-Buff-Ring 17, 35392 Giessen, Germany*
[5)] *Institute for Theoretical Physics, Justus Liebig University, Heinrich-Buff-Ring 16, 35392 Giessen, Germany*

I. GENERAL ASPECTS OF THE SIMULATION SOFTWARE

Simulations of the dynamic properties of nanoparticle systems are performed with a scheme based on the approach presented by Evans et al.[1]. Here, a brief overview of our software and the essential calculations are presented. The basis for simulating time-dependent properties of magnetic systems is given by the partial differential equation describing the precessional motion of the magnetic moment $\boldsymbol{m}$, the so-called the *Landau-Lifshitz-Gilbert equation*:

$$\begin{gathered}\frac{\partial \boldsymbol{m}}{\partial t} = -\frac{\gamma}{1+\alpha^2}\left(\boldsymbol{m}\times\boldsymbol{B}_{\text{eff}} + \alpha\boldsymbol{m}\times\frac{\partial \boldsymbol{m}}{\partial t}\right), \\ \text{where}\quad \boldsymbol{B}_{\text{eff}} = \boldsymbol{B}_{\text{ext}} + \boldsymbol{B}_{\text{dd}} + \boldsymbol{B}_{\text{aniso}} + \boldsymbol{B}_{\text{exc}} + \dots\,.\end{gathered} \tag{1}$$

The variables are the time t, the gyromagnetic ratio γ, the phenomenological damping parameter α, and the effective magnetic field $\boldsymbol{B}_{\text{eff}}$ acting on the magnetic moment. The effective field $\boldsymbol{B}_{\text{eff}}$ is a superposition of all magnetic fields acting on the magnetic moment, such as the external field $\boldsymbol{B}_{\text{ext}}$, the dipole field $\boldsymbol{B}_{\text{dd}}$, the anisotropy field $\boldsymbol{B}_{\text{aniso}}$ caused by the magnetocrystalline anisotropy, the exchange field $\boldsymbol{B}_{\text{exc}}$, and other possible interactions such as e.g. the Dzyaloshinskii-Moriya interaction. As the effective field acting on an individual nanoparticle is the same for all nanoparticles within an infinitely extended, periodically arranged thin film, it is sufficient to simulate a single nanoparticle and the effect of its magnetization on its neighbors in order to derive the dipole field acting on the nanoparticle from its environment. An estimation of a truncation of the dipole interaction is useful for saving computational resources. The dipole field caused by a magnetic moment $\boldsymbol{m}(\boldsymbol{r})$ located at $\boldsymbol{r} = (x, y, z)$ acting on a magnetic moment residing at the origin $\boldsymbol{m}_0$ is described by

$$\boldsymbol{B}^0_{\text{dd}}(\boldsymbol{r}) = \frac{\mu_0}{4\pi}\left(\frac{3\boldsymbol{r}(\boldsymbol{m}\cdot\boldsymbol{r})}{r^5} - \frac{\boldsymbol{m}}{r^3}\right), \tag{2}$$

where μ_0 is the magnetic constant, $\boldsymbol{r}$ the position vector and $r = |\boldsymbol{r}|$ its absolute value. Assuming a two-dimensional hexagonal arrangement of point dipoles around the magnetic moment at the origin $\boldsymbol{m}_0$, each pointing in x-direction ($\boldsymbol{m}(\boldsymbol{r}) = \{m, 0, 0\}$), and integrating over all magnetic moments up to a certain distance R leads to

$$\begin{aligned}\boldsymbol{B}_{\text{dd}}(\boldsymbol{r}) &= \int_1^R \int_0^{2\pi} \frac{\mu_0}{4\pi}\left(\frac{3\boldsymbol{r}(\boldsymbol{m}\cdot\boldsymbol{r})}{r^5} - \frac{\boldsymbol{m}}{r^3}\right) d\phi dr \\ &= -\left\{\frac{m\mu_0}{8R^2}, 0, 0\right\}.\end{aligned} \tag{3}$$

[a)] Electronic mail: Nils.Neugebauer@physik.uni-giessen.de

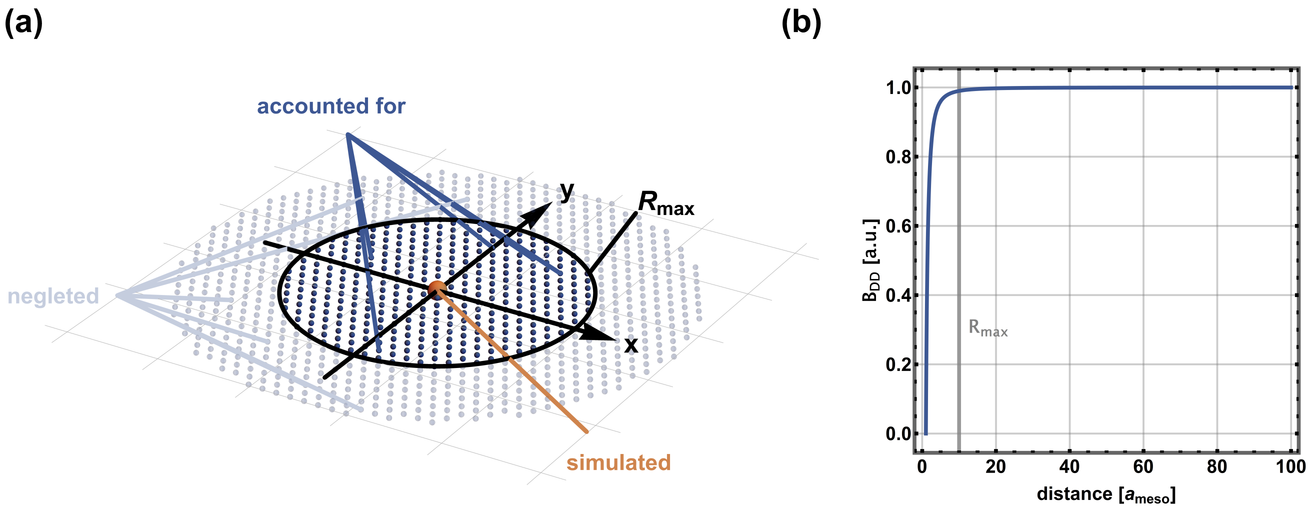

FIG. 1. (a) Schematic illustration of the scheme used for deriving the dipole field experienced by a nanoparticle within an infinitely extended thin film of nanoparticles. As each nanoparticle experiences the same effective magnetic field, it is sufficient to simulate an individual nanoparticle and consider the effect of its magnetization on its neighbors. As the dipole field converges with increasing distance, a truncation of the interaction radius to R_{max} is justified. Nanoparticles for which $R > R_{\mathrm{max}}$ holds are neglected. (b) Dipole field acting on a magnetic moment surrounded by a two-dimensional periodic, hexagonal arrangement of point dipoles (see eq. 3). The truncation of the interaction radius to $R_{\mathrm{max}} = 10a_{\mathrm{meso}}$ is sufficient, as the associated error is only 1%.

Here the position vectors $\boldsymbol{r}$ are given in units of the lattice constant of the mesocrystal a_{meso} and the integration is performed in polar coordinates. As the distance between the point dipoles cannot be closer than a_{meso}, the lower integration boundary is 1. As $m\mu_0/8R^2$ converges for $R \to \infty$, a truncation of the interaction is justified and periodic boundary conditions can be applied. Assuming, e.g., a maximal interaction radius of $R_{\mathrm{max}} = 10a_{\mathrm{meso}}$, an error of 1% for the calculated dipole field occurs which is sufficiently small to mimic periodic boundary conditions. A schematic illustration for calculating the dipole field is given in fig. 1 (a) along with the integrated dipole field vs. R in eq. 3 in fig. 1 (b).

Since the individual MNPs are spherical, and thus do not possess any shape anisotropy, macroscopic demagnetization effects result from the arrangement of the MNP into 2D mesocrystals. The resulting symmetry of the mesocrystal with respect to the external field is therefore appropriately modeled, since the individual dipole fields of each MNP within a sufficiently large R_{max} are taken into account.

The resonance condition derived by C. Kittel for the external field B_{ext} along the z-direction and the microwave field B_ω along the x-direction reads[2]:

$$\frac{\omega}{\gamma} = \sqrt{\left[B_{\mathrm{z}} + \mu_0 \left(N_{\mathrm{y}} - N_{\mathrm{z}}\right) M_{\mathrm{z}}\right] \cdot \left[B_{\mathrm{z}} + \mu_0 \left(N_{\mathrm{x}} - N_{\mathrm{z}}\right) M_{\mathrm{z}}\right]} \tag{4}$$

yielding for the in-plane measurement geometry ($N_{\mathrm{x}} = N_{\mathrm{z}} = 0$ & $N_{\mathrm{y}} = 1$)

$$\frac{\omega}{\gamma} = \sqrt{B_{\mathrm{z}} \cdot \left(B_{\mathrm{z}} + \mu_0 M_{\mathrm{z}}\right)} \tag{5}$$

and for the out-of-plane measurement geometry ($N_{\mathrm{x}} = N_{\mathrm{y}} = 0$ & $N_{\mathrm{z}} = 1$)

$$\frac{\omega}{\gamma} = B_{\mathrm{z}} - \mu_0 M_{\mathrm{z}}. \tag{6}$$

The magnetic field of the magnetocrystalline anisotropy acting on the simulated magnetic moment is represented by[3,4]

$$\boldsymbol{B}_{\mathrm{aniso}} = -\frac{2k_{\mathrm{c}}}{M_{\mathrm{s}}} \cdot \left\{ m_{\mathrm{x}}(m_{\mathrm{y}}^2 + m_{\mathrm{z}}^2), m_{\mathrm{y}}(m_{\mathrm{x}}^2 + m_{\mathrm{z}}^2), m_{\mathrm{z}}(m_{\mathrm{x}}^2 + m_{\mathrm{y}}^2) \right\}, \tag{7}$$

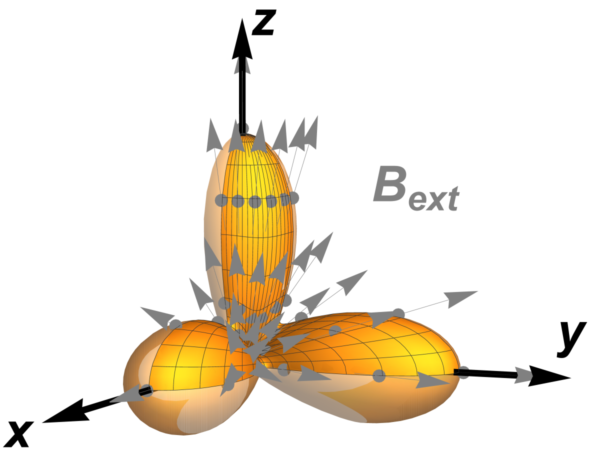

FIG. 2. Magnetocrystalline anisotropy energy surface for magnetite (Fe_3O_4) with $k_c = -1.1 \cdot 10^4\,\mathrm{J/m^3}$ with respect to its principal axes. The magnetic easy axes are along the $\langle 111 \rangle$-directions.

where k_c is the first order cubic anisotropy constant, $M_s = m_{\mathrm{MNP}}/V_{\mathrm{MNP}}$ the saturation magnetization of the MNP with V_{MNP} the volume of the MNP and m_{MNP} the total magnetic moment of the MNP, and m_i the components of the normalized magnetization $\boldsymbol{m}/m = \{m_x, m_y, m_z\}$. In order to adequately incorporate the magnetocrystalline anisotropy, the random orientations of the MNP's principal axes have to be taken into account in the simulations. We make the following simplifying assumptions in order to be able to employ the modelling approach described above. We assume in all calculations that the principal axes of all MNPs of the monolayer are alligned in the same direction and perform calcultions for different orientations of the external magnetic field with respect to the orientation of the MNP's principal axes. Figure 2 depicts the magnetocrystalline anisotropy energy surface $E_{\mathrm{aniso}} = -\boldsymbol{m} \cdot \boldsymbol{B}_{\mathrm{aniso}}$ for $k_c^{Fe_3O_4} = -1.1 \cdot 10^4\,\mathrm{J/m^3}$ of magnetite (Fe_3O_4) with its magnetic easy axes are along the $\langle 111 \rangle$-directions[5]. Averaging over the simulations (or the different orientations between $\boldsymbol{B}_{\mathrm{ext}}$ and the principal axes) yields the impact of the magnetocrystalline anisotropy on the position of the Ferromagnetic resonance and thus the line width and resonance field of the total FMR spectrum.

The time evolution is then calculated by integrating the equation of motion (eq. 1) of each magnetic moment numerically using the FORTRAN90 ODE-solver for ordinary differential equations[6].

II. DISCUSSION OF INDIVIDUAL VS. COLLECTIVE BEHAVIOUR OF MNP MESOCRYSTALS: INTERPARTICLE DIPOLAR COUPLING VS. INTRAPARTICLE MAGNETOCRYSTALLINE ANISOTROPY

The discussion of individual vs. collective properties of mesocrystals composed of magnetic nanoparticles reflects a crucial aspect of the samples investigated in the manuscript. In order to evaluate the associated energies of the magnetocrystalline anisotropy and the dipole-dipole interaction, the following calculations are performed assuming a diameter of the MNPs $d_{\mathrm{MNP}} = 9\,\mathrm{nm}$ and $18\,\mathrm{nm}$, and a spacing $d_{\mathrm{spacer}} = 6\,\mathrm{nm}$ (corresponding to sample 1 - 1 and 3 - 1 as presented in table 1 of the manuscript):

- Dipole-dipole interaction: As in the manuscript, a maximum interaction radius of $R_{\max} = 10 \cdot a_{\mathrm{meso}}$ is assumed. The magnetic moments of all the incorporated MNPs points in x-direction, since the externally applied field aligns the magnetization of all MNPs. The resulting dipole fields for $d_{\mathrm{MNP}} = 9\,\mathrm{nm}$ and $18\,\mathrm{nm}$ are $280\,\mathrm{G}$ and $546\,\mathrm{G}$ in the x-direction, respectively. Thus, the corresponding dipolar energies are $-32\,\mathrm{meV}$ and $-500\,\mathrm{meV}$, for $d_{\mathrm{MNP}} = 9\,\mathrm{nm}$ and $d_{\mathrm{MNP}} = 18\,\mathrm{nm}$ respectively.

- Magnetocrystalline anisotropy: The MNPs investigated in this study consist of magnetite and thus exhibit cubic magnetocrystalline anisotropy. The representation of a cubic anisotropy follows eq. 7 as described in Ref.[4]. The lowest energy states correspond to orientations of the magnetization along the $\langle 111 \rangle$-directions, where $|\boldsymbol{B}_{\mathrm{aniso}}| = 305\,\mathrm{G}$ along $\langle 111 \rangle$ for both diameters $d_{\mathrm{MNP}} = 9\,\mathrm{nm}$ and $18\,\mathrm{nm}$, as $\boldsymbol{B}_{\mathrm{aniso}}$ is independent of the

> volume. Thus, the corresponding energies $E_{\mathrm{aniso}} = -\boldsymbol{m} \cdot \boldsymbol{B}_{\mathrm{aniso}}$ are $E_{\mathrm{aniso}} = -35\,\mathrm{meV}$ for $d_{\mathrm{MNP}} = 9\,\mathrm{nm}$ and $E_{\mathrm{aniso}} = -280\,\mathrm{meV}$ for $d_{\mathrm{MNP}} = 18\,\mathrm{nm}$. The state of the highest energy, i.e. the most unpreferred orientation of the magnetization, corresponds to the $\langle 100 \rangle$-directions of magnetite, where $|\boldsymbol{B}_{\mathrm{aniso}}| = 0\,\mathrm{G}$ and thus the energies are $E_{\mathrm{aniso}} = 0\,\mathrm{meV}$ for both MNP diameters. Taking further into account that the orientations of the principal axes of each MNP after its deposition on the substrate are random, the averaged contribution over all possible orientations is even smaller ($\approx 41\%$ of the values above).

It follows that the contribution of the dipole-dipole interaction is larger than that of the magnetocrystalline anisotropy. Therefore, it can be assumed that the collective oscillation is mostly determined by the dipolar coupling of all MNPs within the monolayer.

All samples investigated in our study show collective behavior, as the spacing between the MNPs is smaller than the diameter of the MNPs themselves. As shown in a previous study[7], dipolar interactions become significant for distances smaller than 5 times the diameter of the magnetic entity. In addition, it has been shown that for MNPs with $d_{\mathrm{MNP}} = 18\,\mathrm{nm}$ and $d_{\mathrm{shell}} = 1\,\mathrm{nm}$, collective oscillations occur and that these are indeed present and detectable using various spectroscopic techniques and micromagnetic simulations[8].

III. SURFACE-TO-VOLUME RATIO OF MNPS

As the size of the MNPs decreases, the proportion of atoms close to the surface n_{surf} increases with respect to the total number of atoms n_{tot} of the MNP. Since the translation symmetry of the crystal is broken at the surface, atoms close to the surface are expected to behave differently from atoms close to the center of the MNP. Figure 3 depicts the ratio $n_{\mathrm{surf}}/n_{\mathrm{tot}}$ assuming different thicknesses of the surface shell s_{surf} (see inset in fig. 3). It can be seen, that $n_{\mathrm{surf}}/n_{\mathrm{tot}}$ is ≈ 1.5 times larger for $d_{\mathrm{MNP}} = 9\,\mathrm{nm}$ than for $d_{\mathrm{MNP}} = 14\,\mathrm{nm}$ and ≈ 2 times larger than for $d_{\mathrm{MNP}} = 18\,\mathrm{nm}$.

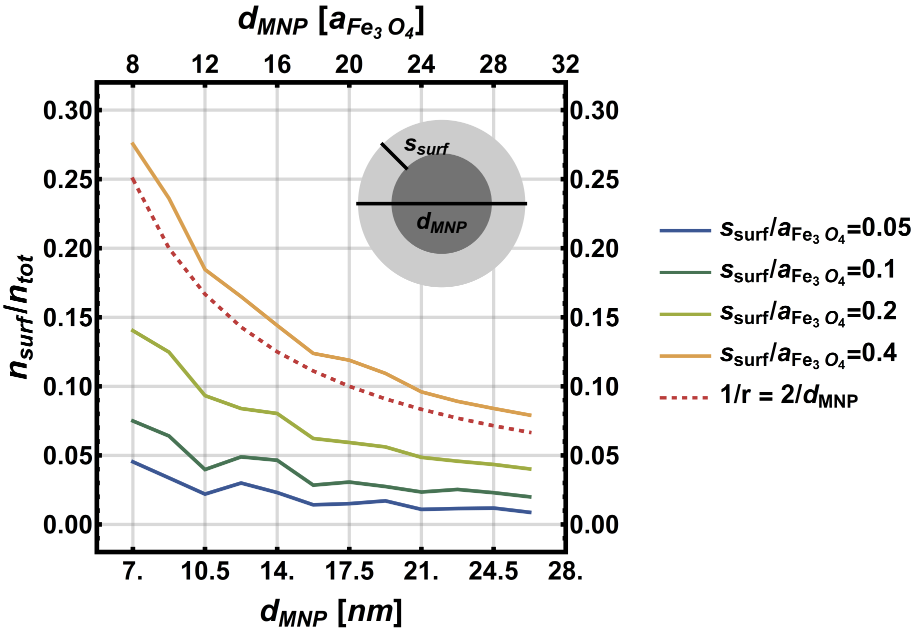

FIG. 3. Ratio of atoms close to the surface n_{surf} with respect to the total number of atoms n_{tot} for different thicknesses of the surface shell s_{surf}. Here, $a_{\mathrm{Fe_3O_4}}$ is the edge length of the unit cell of magnetite.

IV. AVERAGE MAGNETIZATION OF A THIN FILM COMPOSED OF MNPS

As the average magnetization of the thin film M_{film} depends on the packing density of the particles ρ and their spacing, M_{film} may be calculated by:

$$\begin{aligned} M_{\text{film}} &= \rho \cdot M_{\text{MNP}} \\ &= \frac{V_{\text{MNP}}}{V_{\text{UC}}} \cdot M_{\text{MNP}} \\ &= \frac{(4/3)\,\pi\,(d_{\text{MNP}}/2)^2}{(d_{\text{MNP}}+d_{\text{spacer}})^3 \cdot \sin(\pi/3)} \cdot M_{\text{MNP}} \\ &= \frac{\pi\epsilon^3}{3\sqrt{3}\cdot(1+\epsilon)^3} \cdot M_{\text{MNP}}, \end{aligned} \tag{8}$$

where $\rho = V_{\text{MNP}}/V_{\text{UC}}$ is the ratio of the volume occupied with magnetic material V_{MNP} and $V_{\text{UC}} = a^3_{\text{meso}} \sin(\pi/3) = (d_{\text{MNP}} + d_{\text{spacer}})^3 \cdot \sin(\pi/3)$ the volume of the unit cell of the hexagonal close packing and ϵ is the ratio $d_{\text{MNP}}/d_{\text{spacer}}$. Figure 4 depicts M_{film} as a function of $\epsilon = d_{\text{MNP}}/d_{\text{spacer}}$, along with the corresponding averaged thin film magnetization of samples 1 - 1 to 1 - 5. It can be concluded, that M_{film} is only ≈13% of M_{MNP} for sample 1 - 1 and ≈4% of M_{MNP} for sample 1 - 5. Taking into account that the magnetization of the MNPs M_{MNP} is reduced with respect to the bulk value, the simplification of the resonance condition in eq. (3) of the manuscript is justified.

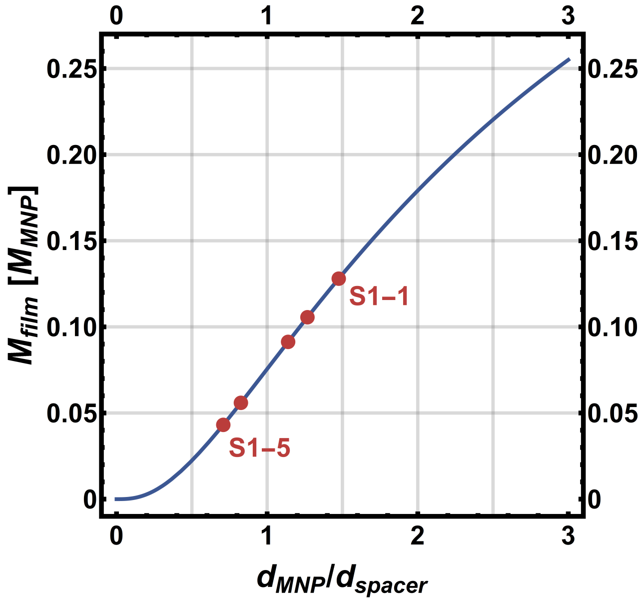

FIG. 4. The average magnetization of the thin film M_{film} in units of the magnetization of the consituent MNPs M_{MNP} as a function of the ratio $\epsilon = d_{\text{MNP}}/d_{\text{spacer}}$. In addition, the average magnetizations for samples 1 - 1 to 1 - 5 are depicted (see table 1 of the manuscript).

[1] R.F.L. Evans, W.J. Fan, P. Chureemart, T.A. Ostler, M.O.A. Ellis, and R.W. Chantrell, Atomistic spin model simulations of magnetic nanomaterials, *J. Phys.: Condens. Matter* **26**, 103202 (2014)

[2] C. Kittel, On the theory of ferromagnetic resonance absorption, *Phys. Rev. B* **73**, 155 (1948)

[3] J.M.D. Coey, Magnetism and magnetic materials, *Cambridge University Press*, ISBN: 9780511845000 (2010)

[4] A. Vansteenkiste, J. Leliaert, M. Dvornik, M. Helsen, F. Garcia-Sanchez, and B. van Waeyenberge, The design and verification of MuMax3, *AIP Advances* **4**, 107133 (2014)

[5] B.W. Zingsem, T. Feggeler, A. Terwey, S. Ghaisari, D. Spoddig, D. Faivre, R. Meckenstock, M. Farle, and M. Winklhofer, Biologically encoded magnonics, *Nat. Comm.* **10**, 4345 (2019)

[6] L. Shampine, M. Gordon, Computer Solution of Ordinary Differential Equations: The Initial Value Problem, *Freeman*, ISBN: 0716704617 (1975)

[7] N. Neugebauer, A. Fabian, M.T. Elm, D.M. Hofmann, M. Czerner, C. Heiliger, and P.J. Klar, Investigation of the dipole interaction in and between ordered arrangements of magnetic nanoparticles, *Phys. Rev. B* **101**, 104409 (2020)

[8] N. Neugebauer, T. Hache, M.T. Elm, D.M. Hofmann, C. Heiliger, H. Schultheiss, and P.J. Klar, Frequency- and magnetic-field-dependent properties of ordered magnetic nanoparticle arrangements, *Phys. Rev. B* **103**, 094438 (2021)

5

Conclusion and Outlook

Over the scope of this dissertation dipolar coupling phenomena within highly ordered magnetic nanoparticle (MNP) arrangements have been systematically investigated. The arrangements were composed of magnetite (Fe_3O_4) MNPs of sizes ranging from $d_{\mathrm{MNP}} = 9\,\mathrm{nm}$ to $d_{\mathrm{MNP}} = 20\,\mathrm{nm}$ and spacings ranging from $d_{\mathrm{spacer}} = 2\,\mathrm{nm}$ to $d_{\mathrm{MNP}} = 18\,\mathrm{nm}$. The experimental characterization of the corresponding samples has been performed employing ferromagnetic resonance experiments (FMR) and Brillouin-light-scattering microscopy (BLS). In corroboration with theoretical numerical modeling, a detailed interpretation of the experimental findings has become possible which in summary contributed to a more detailed understanding of dipolar coupling phenomena at the mesoscopic scale, which has been the main focus of this work. Thus, an understanding of dipolar coupling phenomena at different length scales of a hierarchical magnetic sample is provided. Since the sizes of the MNPs employed in this work are comparable with the characteristics length of the exchange interaction of magnetite [143], a more profound insight into the physical characteristics of MNPs at the border between classically dominated properties to quantum mechanical characteristics has been given.

As the employment of MNPs arranged into mesocrystals introduces additional degrees of freedom to tune the characteristics of a material, it is important to understand and precisely control the associated properties at the different hierarchical levels. This is in principle referred to (i) the scale of the individual MNPs, (ii) the scale of the arrangement of the MNPs, and (iii) the shape of the whole MNP arrangement. The three publications developed over the course of this work address the characteristics on these different levels. Publication 1 demonstrates the feasibility to arrange MNPs into assemblies of defined shape possessing a distinct dependence on the distance between the assemblies and thus addresses aspect (iii). The findings show that similar results may be obtained when using monolithic magnetic nanostructures, but distinct differences most pronounced for the damping are observed, since the MNPs in assemblies were randomly arranged and did not show any ordering. In addition, the occurrence of multiple resonant excitations within circular MNP assemblies has been demonstrated, which is further investigated in Publication 2. Here, the origin of the different resonant excitations within an individual ensemble has been clarified, which covers central aspects of (ii). Furthermore, the improvement of the deposition of the MNPs yielded highly ordered MNP arrangements which have been investigated highlighting the importance of the MNP ordering on the damping of the dynamic characteristics. In order to discuss the properties associated with aspect (i), Publication 3 provides an investigation of the characteristics at the level of the MNP ordering. Here, it was possible not only to contribute to a more detailed

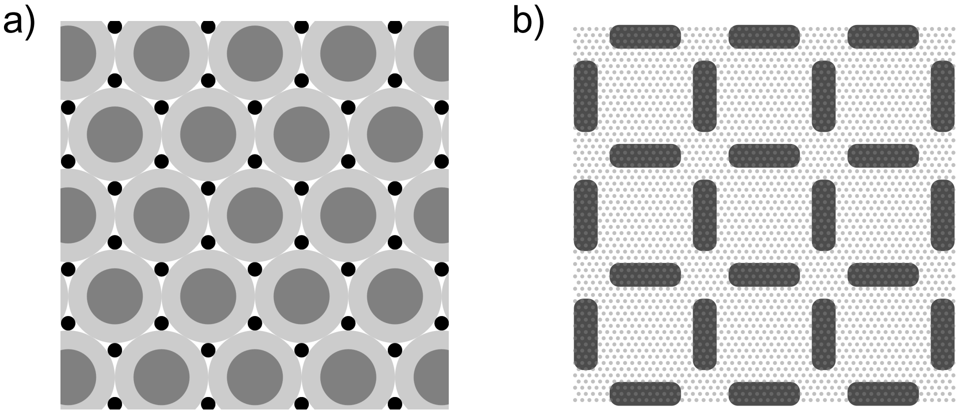

Figure 5.1: a) Schematic illustration of a hexagonal mesocrystal composed of two different species. Depending on the ratio of two particle diameters and the ratio of the particle numbers in the dispersion, various lattices may form [5] which introduce additional anisotropies and coupling phenomena between the MNPs. b) Sketch of an artificial spin ice (dark gray bars) covered with a mesocrystal (light gray dots). Adding the mesocrystal affects the coupling between the magnetic bars and thus the collective properties of the whole artificial spin ice structure.

understanding of the dynamic properties of MNP mesocrystals, but also to highlight that the material parameters of MNPs in the range of $d_{\mathrm{MNP}} = 9\,\mathrm{nm}$ to $d_{\mathrm{MNP}} = 20\,\mathrm{nm}$ may deviate from those of their bulk counterpart.

The above-mentioned findings provide a basis for future investigations regarding the dynamic properties of magnetic mesocrystals. These may be divided into three main routes: (i) Continuing the investigations of the individual characteristics of the MNP by studying differently shaped and sized MNPs, (ii) characterizing and collective properties of MNPs arrangement in different mesocrystal lattices and potential effects of incorporating multiple species of NPs and (iii) employing MNPs to precisely manipulate the characteristics of larger magnetic structures.

Concerning (i), it may be interesting to characterize the dynamic properties of MNPs of sizes which are comparable to those employed in this work and to focus on properties which are dominated by quantum mechanical exchange interactions in more detail as, e.g., suggested in Ref. [11, 17, 25, 26, 32, 43]. In addition, as different shapes of NPs introduce additional magnetic anisotropies, the associated characteristics of the individual MNPs in the exchange dominated regime may also be of great interest. By addressing (ii) and (iii), it is of high interest to exploit the advantages of the employment of mesocrystals in a broader realm by fabricating highly ordered structures composed of two or three nanoparticle species as schematically shown in fig. 5.1 a). For example, by adding diamagnetic nanoparticles to the MNPs in the mesocrystals will introduce additional anisotropies which are not possible to introduce in monolithic materials opening up a vast platform to tune the characteristics of magnetic material.

On the other hand, by using MNPs it may be possible to modulate and control dipolar couplings within, e.g., artificial spin ice (ASI) structures as depicted in fig. 5.1 b). First attempts to precisely manipulate the coupling phenomena in an ASI by depositing magnetic quantum dots have already been performed [144, 145, 146, 147], which may be extended by the employment of MNPs. In principle, two strategies may be pursued here, where (i) the ASI itself is fabricated from a structured MNP mesocrystal employing the approach described in chapter 3.1.2 "Patterning: Electron Beam Lithography", or (ii) by precisely manipulating the dipolar interaction between a previously deposited, monolithic ASI which has been fabricated from a structured thin film. Here, the employment of polystyrene (PS) coated MNPs along with polymethyl methacrylate (PMMA) as the electron resist offer the opportunity to precisely remove MNPs from specific areas of the sample. This can be achieved by utilizing appropriate solvents for PMMA and the MNPs during the deposition and the lift-off process [148]. For example, a previously fabricated monolithic ASI may be covered by a MNP film using spin-coating. Subsequently, PMMA may be deposited onto the same substrate using a solvent for the resist which does not disperse the PS coated MNPs whereby the MNP film remains intact. Exposing the thus fabricated stack with low electron doses, PMMA serves as a positive resist yielding openings in the PMMA layer after the development using a solution of water and isopropanol. In a subsequent step, the uncovered MNPs may be removed using an appropriate solvent such as n-octane, which leaves the remaining PMMA intact.

Bibliography

[1] S. Anantha Ramakrishna "Physics of negative refractive index materials", *Rep. Prog. Phys.* **68**, 449 (2005)

[2] H. Yang, and M. Münzenberg "THz Magnonics" in "The 2021 Magnonics Roadmap", A. Barman, G. Gubbiotti, *J. Phys.: Cond. Matt.* **33**, 413001 (2021)

[3] A. Fabian, M.T. Elm, D.M. Hofmann, and P.J. Klar "Hierarchical structures of magnetic nanoparticles for controlling magnetic interactions on three different length scales", *J. Appl. Phys.* **121**, 224303 (2017)

[4] J. Park, K. An, Y. Hwang, J.G. Park, H.J. Noh, J.Y. Kim, J.H. Park, N.M. Hwang, T. Hyeon "Ultra-Large-Scale Syntheses of Monodisperse Nanocrystal", *Nat. Mater.* **3**, 891 (2004)

[5] E.V. Shevchenko, D.V. Talapin, N.A. Kotov, S. O'Brien, and C.B. Murray "Structural diversity in binary nanoparticle superlattices", *Nature* **439**, 55 (2006)

[6] X. Ye, C. Zhu, P. Ercius, S.N. Raja, B. He, M.R. Jones, M.R. Hauwiller, Y. Liu, T. Xu, and A.P. Alivisatos "Structural diversity in binary superlattices self-assembled from polymer-grafted nanocrystals", *Nat. Comm.* **6**, 10052 (2015)

[7] Y. Wang, J. Chen, C. Zhu, B. Zhu, S. Jeong, Y. Yi, Y. Liu, J. Fiadorwu, P. He, and X. Ye "Kinetically Controlled Self-Assembly of Binary Polymer-Grafted Nanocrystals into Ordered Superstructures via Solvent Vapor Annealing", *Nano Letters* **21**, 5053 (2021)

[8] A. Aharoni "Exchange resonance modes in a ferromagnetic sphere", *J. Appl. Phys.* **69**, 7762 (1991)

[9] A. Aharoni "Effect of surface anisotropy on the exchange resonance modes", *J. Appl. Phys.* **81**, 830 (1997)

[10] J.D. Jackson "Klassische Elektrodynamik", *De Gruyter Studium* (2013), ISBN: 9783110334470

[11] R. Arias, P. Chu, and D. Mills "Dipole exchange spin waves and microwave response of ferromagnetic spheres", *Phys. Rev. B* **71**, 224410 (2005)

[12] J.H. Choi, H. Wang, S.J. Oh, T. Paik, P.S. Jo, J. Sung, X. Ye, T. Zhao, B.T. Diroll, C.B. Murray, C.R. Kagan "Exploiting the colloidal nanocrystal library to construct electronic devices", *Science* **352**, 6282 (2016)

[13] C.R. Kagan, and C.B. Murray "Charge transport in strongly coupled quantum dot solids", *Nature Nanotechnology* **10**, 1013 (2015)

[14] Z. Yang, J. Wei, P. Bonville, and M.P. Pileni "Engineering the Magnetic Dipolar Interactions in 3D Binary Supracrystals Via Mesoscale Alloying", *Adv. Funct. Mat.* **25**, 4908 (2015)

[15] J. Pang, S. Xiong, F. Jaeckel, Z. Sun, D. Dunphy, and C.J. Brinker "Free-standing, patternable nanoparticle/polymer monolayer arrays formed by evaporation induced self-assembly at a fluid interface", *J. Am. Chem. Soc.* **130**, 3284 (2008)

[16] N. Neugebauer, T. Hache, M.T. Elm, D.M. Hofmann, C. Heiliger, H. Schultheiss, and P.J. Klar "Frequency- and magnetic-field-dependent properties of ordered magnetic nanoparticle arrangements", *Phys. Rev. B* **103**, 094438 (2021)

[17] M. Krawczyk, and D. Grundler "Review and prospects of magnonic crystals and devices with reprogrammable band structure", *J. Phys. Cond. Matt.* **26**, 123202 (2014)

[18] N.I. Zheludev, and Y.S. Kivshar "From metamaterials to metadevices", *Nat. Mat.* **11**, 917 (2012)

[19] L. Giovannini, F. Montoncello, and F. Nizzoli "Effect of interdot coupling on spin-wave modes in nanoparticle arrays", *Phys. Rev. B* **75**, 024416 (2007)

[20] J.M. Vargas, W.C. Nunes, L.M. Socolovsky, M. Knobel, and D. Zanche "Effect of dipolar interaction observed in iron-based nanoparticles", *Phys. Rev. B* **72**, 184428 (2005)

[21] C. Moya, O. Iglesias, X. Batlle, and A. Labarta "Quantification of Dipolar Interactions in $Fe_{3-x}O_4$ Nanoparticles", *J. Phys. Chem. C* **119**, 24142 (2015)

[22] S.D. Slöetjes, E. Digernes, C. Klewe, P. Shafer, Q. Li, M. Yang, Z.Q. Qiu, A.T. N'Diaye, E. Arenholz, E. Folven, and J.K. Grepstad "Effects of lattice geometry on the dynamic properties of dipolar-coupled magnetic nanodisk arrays", *Phys. Rev. B* **99**, 064418 (2019)

[23] F. Montoncello, S. Tacchi, L. Giovannini, M. Madami, G. Gubbiotti, G. Carlotti, E. Sirotkin, E. Ahmad, F.Y. Ogrin, and V.V. Kruglyak "Asymmetry of spin wave dispersions in a hexagonal magnonic crystal", *Appl. Phys. Lett.* **102**, 202411 (2013)

[24] N. Ross, M. Kostylev, and R.L. Stamps "Standing spin-wave mode structure and linewidth in partially disordered hexagonal arrays of perpendicularly magnetized sub-micron Permalloy discs", *J. Appl. Phys.* **116**, 113909 (2014)

[25] P. Chu, D. Mills, and R. Arias "Exchange/dipole collective spin-wave modes of ferromagnetic nanosphere arrays", *Phys. Rev. B* **73**, 094405 (2006)

[26] M. Krawczyk, and H. Puszkarski "Plane-wave theory of three-dimensional magnonic crystals", *Phys. Rev. B* **77**, 054437 (2008)

[27] M. Krawczyk, and H. Puszkarski "Magnonic excitations versus three-dimensional structural periodicity in magnetic composites", *Cryst. Res. Technol.* **41**, 547 (2006)

[28] M. Krawczyk, and H. Puszkarski "Magnonic crystal theory of the spin-wave frequency gap in low-doped manganites", *J. Appl. Phys.* **100**, 073905 (2006)

[29] S. Mamica, M. Krawczyk, M.L. Sokolovskyy, and J. Romero-Vivas "Large magnonic band gaps and spectra evolution in three-dimensional magnonic crystals based on magnetoferritin nanoparticles", *Phys. Rev. B* **86**, 144402 (2012)

[30] T. Fließbach "Elektrodynamik II", *Springer*, ISBN: 9783827430359 (2012)

[31] J. Chen, A. Dong, J. Cai, X. Ye, Y. Kang, J.M. Kikkawa, and C.B. Murray "Collective dipolar interactions in self-assembled magnetic binary nanocrystal superlattice membranes", *Nano Letters* **10**, 5103 (2010)

[32] R. Arias, and D. Mills "Theory of collective spin-wave modes of interacting ferromagnetic spheres", *Phys. Rev. B* **70**, 104425 (2004)

[33] Z.K. Wang, V.L. Zhang, H.S. Lim, S.C. Ng, M.H. Kuok, S. Jain, and A.O. Adeyeye "Observation of frequency band gaps in a one-dimensional nanostructured magnonic crystal", *Appl. Phys. Lett.* **94**, 083112 (2009)

[34] F. Fabris, E. Lima Jr., C. Quinteros, L. Nener, M. Granada, M. Sirena, R.D. Zysler, H.E. Troiani, V. Leboran, F. Rivadulla, and E.L. Winkler "Tunnel Magnetoresistance in Self-Assemblies of Exchange-Coupled Core/Shell Nanoparticles", *Phys. Rev. Appl* **11**, 054089 (2019)

[35] C.T. Black, C.B. Murray, R.L. Sandstrom, and S. Sun "Spin-Dependent Tunneling in Self-Assembled Cobalt-Nanocrystal Superlattices", *Science* **290**, 1131 (2000)

[36] J. Chen, X. Ye, S.J. Oh, J.M. Kikkawa, C.R. Kagan, and C.B. Murray "Bistable Magnetoresistance Switching Binary Nanocrystal Superlattices by in Exchange-Coupled CoFe2O4-Fe3O4 Self-Assembly and Thermal Annealing", *ACS Nano* **7**, 1478 (2013)

[37] A. Dong, Y. Jiao, and D.J. Milliron "Electronically coupled nanocrystal superlattice films by in situ ligand exchange at the liquid-air interface", *ACS Nano* **7**, 10978 (2013)

[38] G. Song, M. Ranjbar, D.R. Daughton, and R.A. Kiehl "Nanoparticle-Induced Anomalous Hall Effect in Graphene", *Nano Letters* **19**, 7112 (2019)

[39] D. Song, Z.A. Li, J. Caron, A. Kovács, H. Tian, C. Jin, H. Du, M. Tian, J. Li, J. Zhu, and R.E. Dunin-Borkowski "Quantification of Magnetic Surface and Edge States in an FeGe Nanostripe by Off-Axis Electron Holography", *Phys. Rev. Lett.* **120**, 167204 (2018)

[40] Y. Wu, S. Li, N. Gogotsi, T. Zhao, B. Fleury, C.R. Kagan, C.B. Murray, and J.B. Baxter "Directional Carrier Transfer in Strongly Coupled Binary Nanocrystal Superlattice Films Formed by Assembly and in Situ Ligand Exchange at a Liquid-Air Interface", *J. Phys. Chem.* **121**, 4146 (2017)

[41] M.A. Boles, M. Engel,and D.V. Talapin "Self-assembly of colloidal nanocrystals: From intricate structures to functional materials", *Chem. Rev.* **116**, 11220 (2016)

[42] A. Dong, X. Ye, J. Chen, and C.B. Murray "Two-dimensional binary and ternary nanocrystal superlattices: The case of monolayers and bilayers", *Nano Letters* **11**, 1804 (2011)

[43] P. Chu, and D. Mills "Theory of Brillouin light scattering from ferromagnetic nanospheres", *Phys. Rev. B* **75**, 054405 (2007)

[44] S. Jung, B. Watkins, L. DeLong, J.B. Ketterson, and V. Chandrasekhar "Ferromagnetic resonance in periodic particle arrays", *Phys. Rev. B* **66**, 132401 (2002)

[45] T. Shinjo, T. Okuno, R. Hassdorf, K. Shigeto, T. Ono "Magnetic Vortex Core Observation in Circular Dots of Permalloy", *Science* **289**, 930 (2000)

[46] D. Bisero, P. Cremon, M. Madami, M. Sepioni, S. Tacchi, G. Gubbiotti, G. Carlotti, A.O. Adeyeye, N. Singh, and S. Goolaup "Effect of dipolar interaction on the magnetization state of chains of rectangular particles located either head-to-tail or side-by-side", *J. Nanopart. Res.* **13**, 5691 (2011)

[47] Y. Takagaki, C. Herrmann, and E. Wiebicke "Dipole-dipole interaction in square arrays of MnAs nanodisks on GaAs(001)", *J. Phys.: Condens. Matter* **20**, 225007 (2008)

[48] G. Gubbiotti, S. Tacchi, G. Carlotti, N. Singh, S. Goolaup, A. O. Adeyeye, and M. Kostylev "Collective spin modes in monodimensional magnonic crystals consisting of dipolarly coupled nanowires", *Appl. Phys. Lett.* **90**, 092503 (2007)

[49] C.Yu, M.J. Pechan, and G.J. Mankey "Dipolar induced, spatially localized resonance in magnetic antidot arrays", *Appl. Phys. Lett.* **83**, 3948 (2004)

[50] G. Shimon, and A.O. Adeyeye "Direct observation of configurational anisotropy in coupled magnetic disk cluster using micro-focused Brillouin light scattering spectroscopy", *Appl. Phys. Lett.* **9**, 032407 (2016)

[51] S. Fleutot, G.L. Nealon, M. Pauly, B.P. Pichon, C. Leuvrey, M. Drillon, J.L. Gallani, D. Guillon, B. Donnio, and S. Begin-Colin "Spacing-dependent dipolar interactions in dendronized magnetic iron oxide nanoparticle 2D arrays and powders", *Nanoscale* **5**, 1597 (2013)

[52] J.A. De Toro, P.S. Normile, S.S. Lee, D. Salazar, J.L. Cheong, P. Muniz, J.M. Riveiro, M. Hillenkamp, F. Tournus, A. Tamion, and P.Nordblad "Controlled close-packing of ferrimagnetic nanoparticles: An assessment of the role of interparticle superexchange versus dipolar interactions", *J. Phys. Chem. C* **117**, 10213 (2013)

[53] E.H. Sanchez, M. Vasilakaki, S.S. Lee, P.S. Normile, G. Muscas, M. Murgia, M.S. Andersson, G. Singh, R. Mathieu, P. Nordblad, P.C. Ricci, D. Peddis, K.N. Trohidou, J. Nogues, and J.A. De Toro "Simultaneous Individual and Dipolar Collective Properties in Binary Assemblies of Magnetic Nanoparticles", *Chem. Mater.* **32**, 969 (2020)

[54] M.D. Nguyen, H.V. Tran, S. Xu, and T. Randall Lee "Fe_3O_4 nanoparticles: Structures, synthesis, magnetic properties, surface functionalization, and emerging applications", *Appl. Sci.* **11**, 11301 (2021)

[55] J.A.C. Bland, and B Heinrich"Ultrathin Magnetic Structures I: An Introduction to the Electronic, Magnetic and Structural Properties" *Springer* (1994), ISBN: 9783662308844

[56] J.A.C. Bland, and B Heinrich"Ultrathin Magnetic Structures II: Measurement Techniques and Novel Magnetic Properties" *Springer* (1994), ISBN: 9783540219569

[57] J.A.C. Bland, and B Heinrich"Ultrathin Magnetic Structures III: Fundamentals of Nanomagnetism" *Springer* (1994), ISBN: 9783540219538

[58] J.A.C. Bland, and B Heinrich"Ultrathin Magnetic Structures IV: Applications of Nanomagnetism" *Springer* (1994), ISBN: 9783540219545

[59] D. Menard, and R. Barklia "Electron Paramagnetic and Ferromagnetic Resonance" in "Handbook of Magnetism and Magnetic Materials", M. Coey, and S. Parkin, *Springer* (2021), ISBN: 9783030632083

[60] J.M.D. Coey "Magnetism and magnetic materials", *Cambridge University Press*, ISBN: 9780511845000 (2010)

[61] J.C. Gartside, A. Vanstone, T. Dion, K.D. Stenning, D.M. Arroo, H. Kurebayashi, and W.R. Branford "Reconfigurable magnonic mode-hybridisation and spectral control in a bicomponent artificial spin ice", *Nat. Comm.* **12**, 2488 (2021)

[62] J.C. Gartside, K.D. Stenning, A. Vanstone, H.H. Holder, D.M. Arroo, T. Dion, F. Caravelli, H. Kurebayashi, and W.R. Branford "Reconfigurable training and reservoir computing in an artificial spin-vortex ice via spin-wave fingerprinting", *Nat. Nanotech.* **17**, 460 (2022)

[63] V. Iurchuk, J. Pablo-Navarro, T. Hula, R. Narkowicz, G. Hlawacek, L. Körber, A. Kákay, H. Schultheiss, J. Fassbender, K. Lenz, and J. Lindner "Tailoring crosstalk between localized 1D spin-wave nanochannels using focused ion beams", *Sci. Rep.* **13**, 764 (2023)

[64] B.W. Zingsem, T. Feggeler, A. Terwey, S. Ghaisari, D. Spoddig, D. Faivre, R. Meckenstock, M. Farle, and M. Winklhofer "Biologically encoded magnonics", *Nat. Comm.* **10**, 4345 (2019)

[65] M. Farle "Ferromagnetic resonance of ultrathin metallic layers", *Rep. Prog. Phys* **61**, 776 (1998)

[66] H.T. Jeng, and G.Y. Guo "First-principles investigations of the electronic structure and magnetocrystalline anisotropy in strained magnetite", *Phys. Rev. B* **765**, 094429 (2002)

[67] T. Sebastian, K. Schultheiss, B. Obry, B. Hillebrands, and H. Schultheiss "Micro-focused Brillouin light scattering: imaging spin waves at the nanoscale", *Frontiers in Physics* **3**, 35 (2015)

[68] A. Banholzer, R. Narkowicz, C. Hassel, R. Meckenstock, S. Stienen, O. Posth, D. Suter, M. Farle, and J. Lindner "Visualization of spin dynamics in single nanosized magnetic elements", *Nanotechnology* **22**, 295713 (2011)

[69] C. Schoeppner, K. Wagner, S. Stienen, R. Meckenstock, M. Farle, R. Narkowicz, D. Suter, and J. Lindner "Angular dependent ferromagnetic resonance analysis in a single micron sized cobalt stripe", *J. Appl. Phys.* **116**, 033913 (2014)

[70] R. Narkowicz, D. Suter, and I. Niemeyer "Scaling of sensitivity and efficiency in planar microresonators for electron spin resonance", *Rev. Sci. Instr.* **79**, 084702 (2008)

[71] R. Narkowicz, D. Suter, and R. Stonies "Planar microresonators for EPR experiments", *J. Mag. Res.* **175**, 275 (2005)

[72] K. Lenz, R. Narkowicz, K. Wagner, C.F. Reiche, J. Körner, T. Schneider, A. Kákay, H. Schultheiss, U. Weissker, D. Wolf, D. Suter, B. Büchner, J. Fassbender, T. Mühl, and J. Lindner "Scaling of sensitivity and efficiency in planar microresonators for electron", *Small* **15**, 1904315 (2019)

[73] S. Pile, S. Stienen, K. Lenz, R. Narkowicz, S. Wintz, J. Förster, S. Mayr, M. Buchner, M. Weigand, V. Ney, J. Lindner, and A. Ney "Nonstationary spin waves in a single rectangular permalloy microstrip under uniform magnetic excitation", *Phys. Rev. B* **105**, 094415 (2022)

[74] H. Cansever, R. Narkowicz, K. Lenz, C. Fowley, L. Ramasubramanian, O. Yildirim, A. Niesen, T. Huebner, G. Reiss, J. Lindner, J. Fassbender, and A.M. Deac "Investigating spin-transfer torques induced by thermal gradients in magnetic tunnel junctions by using micro-cavity ferromagnetic resonance", *J. Phys. D: Appl. Phys.* **51**, 224009 (2018)

[75] B. Hillebrands, and G. Güntherodt "Brillouin Light Scattering in Magnetic Superlattices" in "Ultrathin Magnetic Structures II: Measurement Techniques and Novel Magnetic Properties", J.A.C. Bland, and B Heinrich, *Springer* (1994), ISBN: 9783540219569

[76] J.F. Cochran "Light Scattering from Ultrathin Magnetic Layers and Bilayers" in "Ultrathin Magnetic Structures II", B. Heinrich, and J.A.C. Bland, *Springer*, ISBN: 9783662225776 (1994)

[77] J.F. Cochran "Brillouin light scattering intensities for patterned magnetic thin films", *J. Mag. Mag. Mat.* **212**, 40 (2000)

[78] Y. Zhu "Brillouin light scattering spectroscopy" in "Modern Techniques for Characterizing Magnetic Materials", *Springer*, ISBN: 1402080077 (2005)

[79] J.F. Cochran "Radio Frequency Techniques" in "Ultrathin Magnetic Structures II", B. Heinrich, and J.A.C. Bland, *Springer*, ISBN: 9783662225776 (1994)

[80] H. Schultheiss "Kohärenz und Dämpfungsverhalten von Spinwellen in magnetischen Mikrostrukturen", *Dissertation*, TU Kaiserslautern (2010)

[81] S. Tacchi, G. Gubbiotti, M. Madami, and G. Carlott "Brillouin light scattering studies of 2D magnonic crystals", *J. Phys. Cond. Matt.* **29**, 073001 (2017)

[82] A. Kumar Chaurasiya, A. Kumar Mondal, J.C. Gartside, K.D. Stenning, A. Vanstone, S. Barman, W.R. Branford, and A. Barman "Comparison of Spin-Wave Modes in Connected and Disconnected Artificial Spin Ice Nanostructures Using Brillouin Light Scattering Spectroscopy", *ACS Nano* **15**, 11734 (2021)

[83] S. Tacchi, G. Duerr, J.W. Klos, M. Madami, S. Neusser, G. Gubbiotti, G. Carlotti, M. Krawczyk, and D. Grundler "Forbidden band gaps in the spin-wave spectrum of a two-dimensional bicomponent magnonic crystal", *Phys. Rev. Lett.* **109**, 137202 (2012)

[84] S. Neusser, and D. Grundler "Magnonics: Spin Waves on the Nanoscale", *Advanced Materials* **21**, 2927 (2009)

[85] S. Zhang, I. Gilbert, C. Nisoli, G.W. Chern, M.J. Erickson, L. O'Brien, C. Leighton, P.E. Lammert, V.H. Crespi, and P. Schiffer "Crystallites of magnetic charges in artificial spin ice", *Nature* **500**, 553 (2013)

[86] J.C. Gartside, D.M. Burn, L.F. Cohen, and W.R. Branford "A novel method for the injection and manipulation of magnetic charge states in nanostructures", *Sci. Rep.* **6**, 32864 (2016)

[87] J.C. Gartside, D.M. Arroo, D.M. Burn, V.L. Bemmer, A. Moskalenko, L.F. Cohen, and W.R. Branford "Realization of ground state in artificial kagome spin ice via topological defect-driven magnetic writing", *Nat. Nanotech.* **13**, 53 (2018)

[88] V.F. Puntes, P. Gorostiza, D.M Aruguete, N.G. Bastus, and A.P. Alivisatos "Collective behaviour in two-dimensional cobalt nanoparticle assemblies observed by magnetic force microscopy", *Nat. Mat.* **3**, 263 (2004)

[89] M. Varón, M. Beleggia, T. Kasama, R.J. Harrison, R.E. Dunin-Borkowski, V.F. Puntes, and C. Frandsen "Dipolar magnetism in ordered and disordered low-dimensional nanoparticle assemblies", *Sci. Rep.* **3**, 1234 (2013)

[90] M. Varon, M. Beleggia, J. Jordanovic, J. Schiotz, T. Kasama, V.F. Puntes, and C. Frandsen "Longitudinal domain wall formation in elongated assemblies of ferromagnetic nanoparticles", *Sci. Rep.* **5**, 14536 (2015)

[91] R.E. Dunin-Borkowski, A. Kovács, T. Kasama, M.R. McCartney, and D.J. Smith "Electron Holography" in "Springer Handbook of Microscopy", P.W. Hawkes, and J.C.H. Spence, *Springer* (2019), ISBN: 9783030000691

[92] F. Bodker, S. Morup, and S. Linderoth "Surface Effects in Metallic Iron Nanoparticles", *Phys. Rev. Lett.* **72**, 282 (1993)

[93] E. Lima, A.L. Brandl, A.D. Arelaro, and G.F. Goya "Spin disorder and magnetic anisotropy in Fe3O4 nanoparticles", *J. Appl. Phys.* **99**, 083908 (2006)

[94] M.J. Donahue, and D.G. Porter "OOMMF 2.0 User's Guide", *National Institute of Standards and Technology* (2018), URL: `https://math.nist.gov/oommf/doc/userguide20a1/userguide/`

[95] A. Vansteenkiste, J. Leliaert, M. Dvornik, M. Helsen, F. Garcia-Sanchez, and B. van Waeyenberge "The design and verification of MuMax3", *AIP Advances* **4**, 107133 (2014)

[96] S. Jung, J.B. Ketterson, and V. Chandrasekhar "Micromagnetic calculations of ferromagnetic resonance in submicron ferromagnetic particles", *Phys. Rev. B* **66**, 132405 (2002)

[97] L. Körber, G. Quasebarth, A. Otto, and A. Kakay "Finite-element dynamic-matrix approach for spin-wave dispersions in magnonic waveguides with arbitrary cross section", *AIP Advances* **11**, 095006 (2021)

[98] R.F.L. Evans, W.J. Fan, P. Chureemart, T.A. Ostler, M.O.A. Ellis, and R.W. Chantrell "Atomistic spin model simulations of magnetic nanomaterials", *J. Phys.: Condens. Matter* **26**, 103202 (2014)

[99] B. Skubic, J. Hellsvik, L. Nordström, and O. Eriksson "A method for atomistic spin dynamics simulations: Implementation and examples", *J. Phys. Cond. Matter* **20**, 315203 (2008)

[100] W. Nolting "Quantentheorie des Magnetismus 1", *B.G. Teubner Stuttgart*, ISBN: 3519030845 (1986)

[101] W. Nolting "Quantentheorie des Magnetismus 2", *B.G. Teubner Stuttgart*, ISBN: 3519030853 (1986)

[102] W. Nolting "Quantum Theory of Magnetism", *Springer*, ISBN: 9783540854159 (2009)

[103] J. Rumble "CRC Handbook of Chemistry and Physics", *CRC Press*, ISBN: 781032121710 (2009)

[104] S. Blundell "Magnetism in Condensed Matter" *Oxford University Press* (2001), ISBN: 0198505922

[105] W. Pauli "Über Gasentartung und Paramagnetismus", *Z. Phys.* **41**, 81 (1927)

[106] L.D. Landau "Diamagnetismus der Metalle", *Z. Phys.* **64**, 629 (1930)

[107] N. Bohr "The doctors dissertation: Studies on the Electron Theory of Metals", *Dissertation*, University Copenhagen (1911)

[108] H.J. v. Leeuwen "Problemes de la theorie electronique du magnetisme", *J. Phys. Radium* **2**, 361 (1921)

[109] R.G. Piety "Ferromagnetic Anisotropy of Iron Crystals at Various Temperatures", *Phys. Rev.* **50**, 1173 (1936)

[110] W. Heisenberg "Mehrkörperproblem und Resonanz in der Quantenmechanik", *Zeitschrift für Physik* **38**, 411 (1926)

[111] P.A.M. Dirac "On the theory of quantum mechanics", *Proc. Royl. Soc. A* **112**, 661 (1926)

[112] W. Gerlach and O. Stern "Der experimentelle Nachweis der Richtungsquantelung im Magnetfeld", *Zeitschrift für Physik* **9**, 349 (1922)

[113] R. Skomski "Magnetic Exchange Interactions" in "Handbook of Magnetism and Magnetic Materials", M. Coey, and S. Parkin, *Springer* (2021), ISBN: 9783030632083

[114] M. Uhl, and B. Siberchicot "A first-principles study of exchange integrals in magnetite", *J. Phys.: Condens. Matter* **7**, 4227 (1995)

[115] Z. Nedelkoski, D. Kepaptsoglou, L. Lari, T. Wen, R.A. Booth, S.D. Oberdick, P.L. Galindo, Q.M. Ramasse, R.F. L. Evans, S. Majetich, and V.K. Lazarov "Origin of reduced magnetization and domain formation in small magnetite nanoparticles", *Sci. Rep.* **7**, 1038 (2017)

[116] R. Skomski "Anisotropy and Crystal Field" in "Handbook of Magnetism and Magnetic Materials", M. Coey, and S. Parkin, *Springer* (2021), ISBN: 9783030632083

[117] A. Aharoni "Introduction to the Theory of Ferromagnetism", *Oxford University Press*, ISBN: 9780198508083

[118] D.D. Stancil, and A. Prabhakar "Spin Waves: Theory and Applications", *Springer Science+Business Media*, ISBN: 9780387778648 (2009)

[119] S. Tandon, M. Beleggia, Y. Zhu, and M. de Graef "On the computation of the demagnetization tensor for uniformly magnetized particles of arbitrary shape. Part I: Analytical approach", *J. Mag. Mag. Mat.* **271**, 9 (2004)

[120] B. Krüger, G. Selke, A. Drews, and D. Pfannkuche "Fast and accurate calculation of the demagnetization tensor for systems with periodic boundary conditions", *IEEE Trans. Mag.* **49**, 4749 (2013)

[121] B. Hillebrands, and S. Blügel "Magnetismus" in "Lehrbuch der Experimentalphysik: Festkörper", R. Kassing, *W. de Gruyter* (2005), ISBN: 3110174855

[122] C. Kittel "On the theory of ferromagnetic resonance absorption", *Phys. Rev. B* **73**, 155 (1948)

[123] D. Petrascheck, and F. Schwabl "Elektrodynamik", *Springer*, ISBN: 9783662597866 (2019)

[124] A. Aharoni "Demagnetizing factors for rectangular ferromagnetic prisms", *J. Appl. Phys.* **83**, 3432 (1998)

[125] M. Donahue, and D.G. Porter "Quantitative Evaluation of Errors in Calculation of the Demagnetization Tensor", *Presentation at: MMM-Intermag Conference in Washington, DC* (2020), available via URL: `https://math.nist.gov/~MDonahue/talks/mmm2020-talk.pdf`

[126] A. Newell, W. Williams, and D. Dunlop "A Generalization of the Demagnetizing Tensor for Nonuniform Magnetization", *J. Geophys. Res.* **98**, 9551 (1993)

[127] K. Lebecki, M. Donahue, and M. Gutowski "Periodic boundary conditions for demagnetization interactions in micromagnetic simulations", *J. Phys. D: Appl. Phys.* **41**, 175005 (2008)

[128] H. How, and C. Vittoria "Demagnetization energy and magnetic permeability tensor of spheroidal magnetic particles dispersed in cubic lattices", *Phys. Rev. B* **43**, 8094 (1991)

[129] J. Kaczer, and L. Murtinova "On the demagnetizing energy of periodic magnetic distributions", *Phys. Stat. Sol. (a)* **23**, 79 (1974)

[130] R. Moreno, R.F.L. Evans, S. Khmelevskyi, M.C. Munoz, R.W. Chantrell, and O. Chubykalo-Fesenko "Temperature-dependent exchange stiffness and domain wall width in Co", *Rep. Prog. Phys* **61**, 776 (1998)

[131] N. Neugebauer, A. Fabian, M.T. Elm, D.M. Hofmann, M. Czerner, C. Heiliger, and P.J. Klar "Investigation of the dipole interaction in and between ordered arrangements of magnetic nanoparticles", *Phys. Rev. B* **101**, 104409 (2020)

[132] N. Neugebauer, Y. Wang, M.T. Elm, D.M. Hofmann, C. Heiliger, X. Ye, and P.J. Klar "Distance and size dependence of the interactions within highly ordered magnetic nanoparticle mesocrystals", *Phys. Rev. B* **107**, 184410 (2023)

[133] D. Frenkel "Entropy-driven phase transitions", *Physica A* **263**, 26 (1999)

[134] J.L. Barrat "Basic Concepts for Simple and Complex Liquids", *Cambridge University Press*, ISBN: 9780511606533

[135] C. Kittel "Excitation of spin waves in an antiferromagnet by a uniform rf field", *Phys. Rev. B* **110**, 1295 (1958)

[136] Y. Wiemann, J. Simmendinger, C. Clauss, L. Bogani, D. Bothner, D. Koelle, R. Kleiner, M. Dressel, and M. Scheffler "Observing electron spin resonance between 0.1 and 67 GHz at temperatures between 50 mK and 300 K using broadband metallic coplanar waveguides", *Appl. Phys. Lett.* **106**, 193505 (2015)

[137] I.A. Yastremsky, O.M. Volkov, M. Kopte, T. Kosub, S. Stienen, K. Lenz, J. Lindner, J. Fassbender, B.A. Ivanov, and D. Makarov "Thermodynamics and Exchange Stiffness of Asymmetrically Sandwiched Ultrathin Ferromagnetic Films with Perpendicular Anisotropy", *Phys. Rev. Appl.* **12**, 064038 (2019)

[138] S.O. Demokritov, and A.N. Slavin "Spin Waves" in "Handbook of Magnetism and Magnetic Materials", M. Coey, and S. Parkin, *Springer* (2021), ISBN: 9783030632083

[139] J.E. Miltat, and M.J. Donahue "Numerical Micromagnetics: Finite Difference Methods" in "Handbook of Magnetism and Advanced Magnetic Materials", H. Kronmüller, and S. Parkin, *Wiley* (2007), ISBN: 9780470022177

[140] L. Shampine, M. Gordon "Computer Solution of Ordinary Differential Equations: The Initial Value Problem", *Freeman*, ISBN: 0716704617 (1975)

[141] J.C. Butcher "Numerical Methods for Ordinary Differential Equations", *Wiley*, ISBN: 9781119121503 (2016)

[142] C. Mitsumata, and S. Tomita "Control of Gilbert damping using magnetic metamaterials", *Phys. Rev. B* **84**, 174421 (2011)

[143] G.S. Abo, Y.K. Hong, J. Park, J. Lee, W. Lee, and B.C. Choi "Definition of magnetic exchange length", *IEEE Trans. Mag.* **49**, 4937 (2013)

[144] R. Negrello, F. Montoncello, M.T. Kaffash, M B. Jungfleisch, and G. Gubbiotti "Dynamic coupling and spin-wave dispersions in a magnetic hybrid system made of an artificial spin-ice structure and an extended NiFe underlayer", *APL Materials* **10**, 091115 (2022)

[145] M.T. Kaffash, W. Bang, S. Lendinez, A. Hoffmann, J.B. Ketterson, and M.B. Jungfleisch "Control of spin dynamics in artificial honeycomb spin-ice-based nanodisks", *Phys. Rev. B* **101**, 174424 (2020)

[146] E. Östman, H. Stopfel, I.A. Chioar, U.B. Arnalds, A. Stein, V. Kapaklis, and B. Hjörvarsson "Interaction modifiers in artificial spin ices", *Nature Phys.* **14**, 375 (2018)

[147] Y. Sun, M.B. Salamon, K. Garnier, and R.S. Averback "Memory Effects in an Interacting Magnetic Nanoparticle System", *Phys. Rev. Lett.* **91**, 167206 (2003)

[148] J. Brandrup, and E.H. Immergut "Polymer Handbook, Second Edition", *John Wiley & Sons* (1975), ISBN: 9780471481720

Danksagung

An dieser Stelle möchte ich mich bei allen bedanken, die mich während der Zeit dieser Arbeit unterstützt und begleitet und zum Gelingen dieses Abschlusses beigetragen haben. Dabei möchte ich neben den wissenschaftlichen Debatten auch die persönlichen Auseinandersetzungen hervorheben, welche ganz wesentlich für eine schöne Zeit an der Justus-Liebig-Universität gesorgt haben. Diese habe ich sehr genossen und mein besonderer Dank gilt dabei:

- Prof. Dr. Peter J. Klar[1,2]
- Prof. Dr. Christian Heiliger [2,3]
- Dr. Matthias T. Elm[1,2]
- Prof. Dr. Detlev M. Hofmann[1,2]
- Dr. Helmut Schultheiss[4,5] und Dr. Toni Hache[4,6]
- Prof. Dr. Xingchen Ye[7] und Yi Wang[7]
- Prof. Dr. Hans-Albrecht Kurg von Nidda[8] und Dr. Dieter Ehlers[8]
- Dr. Kilian Lenz[4]
- Dr. Janis K. Eckhardt[1,3], Dr. Alexander Fabian[1,3], Dr. Marcel Giar[1,3] und Dr. Michael Czerner[1,3]

Abschließend möchte ich mich von ganzem Herzen bei meinen Freunden und vor allem bei meiner Familie und bedanken, ohne deren Unterstützung und stets guter Rat mir diese Weg und diese Arbeit nicht möglich gewesen wäre.

---

[1] Institute of Experimental Physics I, Justus Liebig University, Heinrich-Buff-Ring 16, 35392 Giessen, Germany

[2] Center for Materials Research (ZfM/LaMa), Justus Liebig University, Heinrich-Buff-Ring 16, 35392 Giessen, Germany

[3] Institute for Theoretical Physics, Justus Liebig University, Heinrich-Buff-Ring 16, 35392 Giessen, Germany

[4] Helmholtz-Center Dresden-Rossendorf, Institute of Ion Beam Physics and Materials Research, Bautzner Landstraße 400, 01328 Dresden, Germany

[5] Technische Universität Dresden, 01062 Dresden, Germany

[6] Institute for Physics, Technische University Chemnitz, 09107 Chemnitz, Germany

[7] Department of Chemistry, Indiana University, Bloomington, 47405 Indiana, United States

[8] Center for Electronic Correlations and Magnetism, Institute of Physics, University of Augsburg, 86135 Augsburg, Germany

Selbstständigkeitserklärung

(German)
Hiermit versichere ich, die vorgelegte Arbeit selbstständig und ohne unerlaubte fremde Hilfe und nur mit den Hilfen angefertigt zu haben, die ich in der Arbeit angegeben habe. Alle Textstellen, die wörtlich oder sinngemäß aus veröffentlichten Schriften entnommen sind, und alle Angaben die auf mündlichen Auskünften beruhen, sind als solche kenntlich gemacht. Bei den von mir durchgeführten und in der Arbeit erwähnten Untersuchungen habe ich die Grundsätze guter wissenschaftlicher Praxis, wie sie in der „Satzung der Justus-Liebig-Universität zur Sicherung guter wissenschaftlicher Praxis“ niedergelegt sind, eingehalten. Gemäß § 25 Abs. 6 der Allgemeinen Bestimmungen für modularisierte Studiengänge dulde ich eine Überprüfung der Arbeit mittels Anti-Plagiatssoftware.

(English)
I declare that I have completed this dissertation single-handedly without the unauthorized help of a second party and only with the assistance acknowledged therein. I have appropriately acknowledged and cited all text passages that are derived verbatim from or are based on the content of published work of others, and all information relating to verbal communications. I consent to the use of an anti-plagiarism software to check my thesis. I have abided by the principles of good scientific conduct laid down in the charter of the Justus Liebig University Giessen „Satzung der Justus-Liebig-Universität Gießen zur Sicherung guter wissenschaftlicher Praxis“ in carrying out the investigations described in the dissertation

Datum

Nils Neugebauer